

UNIVERSITY OF CALIFORNIA
SANTA CRUZ

EMERGENT PHENOMENA IN ACTIVE POLYMER ARRAYS

A dissertation submitted in partial satisfaction of the
requirements for the degree of

DOCTOR OF PHILOSOPHY

in

PHYSICS

by

Stephen E. Martin

September 2018

The Dissertation of Stephen E. Martin
is approved:

Professor Joshua Deutsch, Chair

Professor Onuttom Narayan

Professor Alexander Sher

Lori Kletzer
Dean of Graduate Studies

Table of Contents

List of Figures	v
Abstract	ix
Dedication	x
Acknowledgments	xi
1 Introduction	1
1.1 Outline	2
1.2 Motor proteins and non-equilibrium	4
1.2.1 Actin and myosin	4
1.2.2 Kinesin and microtubules	7
1.3 Stokes flow	8
1.3.1 The stokeslet	10
1.3.2 Boundary-value problems with stokeslets	11
2 Photomechanical Energy Conversion Using Polymer Brush Dissocia- tion	21
2.1 Introduction	21
2.2 The System	24
2.3 Estimate of system parameters	27
2.4 Three dimensional model	28
2.5 Steady State Probability Distribution	34
2.6 One dimensional solution	38
2.7 Unbound Equilibration Model	44
2.7.1 Efficiency in large power stroke limit	52
2.8 Conclusions	56
3 Emergence of Metachronal Waves in Active Microtubule Arrays	59
3.1 Introduction	59
3.2 Proposed Mechanism of Action	61

3.3	The Quasi-2D Interaction Tensor	65
3.4	Simulation Methods	69
3.5	Analysis of Unipolarity	73
3.5.1	Instability of mixed polarity bundles	74
3.5.2	Model of mixed polarity bundles	76
3.6	Results	79
3.7	Discussion	84
3.8	Conclusions	86
4	Spontaneous Circulation of Active Microtubules Confined by Optical Traps	88
4.1	Introduction	88
4.2	Preliminary Estimations	90
4.2.1	Laser frequency	90
4.2.2	Forces	90
4.2.3	Heating	92
4.3	Method of simulation	94
4.3.1	Kinesin drag force	96
4.3.2	Description of other forces	97
4.3.3	Interaction tensor	100
4.4	Results	102
4.4.1	Types of microtubule motion	102
4.4.2	Fluid velocity field	103
4.4.3	Angular momentum power spectra	105
4.5	System behavior and simulation parameters	108
4.6	Conclusion	109
	Bibliography	112
	A Supplementary Videos	124

List of Figures

1.1	A series of illustrations depicting the mechanism by which muscles contract. Image credit to OpenStax Anatomy and Physiology.	5
1.2	An illustration of the image charge system used by Blake to simplify the approach to solving the flow due to a stokeslet in the vicinity of an infinite plane. The real stokeslet (with arbitrary direction) is shown as the red dot ($z = h$). The infinite no-slip surface is the $z = 0$ plane, and the image stokelet (blue dot) is placed at $z = -h$ with equal magnitude and opposite direction.	13
1.3	An illustration of the image charge system used by Liron and Mochon to simplify the approach to solving the parallel-plate stokeslet flow. The real stokeslet is shown as the red dot near $z = 0$, and the solid black lines are the plates. All other dots are image stokelets, with blue dots opposing the real stokeslet and red dots identical.	17
1.4	Comparison of flows due to a single stokeslet in the three geometries described in sections 1.3.2.1-1.3.2.3. All figures are for a stokeslet placed at the origin, pointing in the x -direction with unit magnitude. (a) $u_x(x, 0, 0)$, the fluid velocity in the direction of the stokeslet along the x -axis. The dashed lines are guides to the eye for $u_x \propto r^{-1}$ (blue), $u_x \propto r^{-2}$ (green), and $u_x \propto r^{-3}$ (red). (b) $ u_x(0, y, 0) $, the fluid speed in the direction of the stokeslet along the y -axis. The dashed lines are guides to the eye for $u_x \propto r^{-1}$ (blue), $u_x \propto r^{-2}$ (green), and $u_x \propto r^{-5}$ (red). The cusp in the green curve indicates the transition from $u_x > 0$ (flowing in the same direction as the stokeslet) and $u_x < 0$ (flowing opposite the stokeslet). (c) A zoomed in view of $u_x(0, y, 0)$, showing backward flow for the parallel plate geometry.	19

2.1	(a) A schematic of the light energy to mechanical converter. A polymer brush of semiflexible chains is put in contact with a plate a height h above the base, containing an array of anisotropic binding sites with preferred binding direction $\hat{\mathbf{n}}_a$. Polymer ends are trapped by unlikely thermal fluctuations, applying a non-zero average force parallel to the plate. Photodissociation of the polymer ends with the binding sites releases the chain end that will move until it finds another site. The upper plate moves at a velocity v , thereby generating power. A single track is shown, and the separation between binding sites is L . The shape of the binding sites is meant only as a guide to the eye concerning the direction of $\hat{\mathbf{n}}_a$, and is not necessarily an indicator of the binding sites' physical structure.	26
2.2	A plot of the isotropic binding potential $U_i(r)$ vs. r , for $A = 0.2$, potential well depth $V_a = 60$, and interaction length scale $r_s = 1$	30
2.3	The average force f and the power $P = fv$ measured as a function of the relative velocity between the plates v . For clarity, the power is multiplied by 2000. There were 4 links, with a plate separation of $h = 1$, spacing between binding sites $L = 2$, the direction of $\hat{\mathbf{n}}_a$ (that is, the binding angle) is $\pi/4$, $V_a = 60$, $A = 0.2$, link length of 1, stiffness constant $C = 0.5$, potential range $r_s = 1.0$, and a coefficient of damping of 10. The coefficients of binding and unbinding, respectively, are (a) $c_0 = c_1 = 0.05$, and (b) $c_0 = c_1 = 0.4$	32
2.4	The average force f and the power $P = fv$ measured as a function of the relative velocity between the plates v . The binding sites are placed randomly, with average binding site separation $\bar{d} = 2$ and minimum binding site separation $d_{min} = 0.1$. Other than this, the same parameters and scaling are used as in Fig. 2.3: (a) $c_0 = c_1 = 0.05$, and (b) $c_0 = c_1 = 0.4$	33
2.5	An asymmetric spring potential used to tether the chain. It has a second dip at approximately $x = 2$	41
2.6	Plots of the probability distribution of P_1 as a function of position x for $x' = -\pi, -\pi/2, 0$, and $\pi/2$ for the asymmetric spring model Eq. 2.22.	42
2.7	Plots of the probability distribution of P_1 as a function of position x for the values of x' shown in Fig. 2.6, but for an asymmetric periodic potential and a linear spring.	43
2.8	Illustration of the kind of potentials employed in the Unbound Equilibration Model. The periodic potential V_p is nonzero only on small regions on the x -axis. It shows a large peak of height V_{max} and large negative dip V_{min} . The spring potential V_0 is parabolic, except that it has a cutoff where it becomes infinite when stretched by more than l_c . The corresponding probability distribution P_0 (grey curve) is assumed to have relaxed to equilibrium. The spring potential is shown at two different position, when it is centered at x' and $L - x'$	45

2.9	(a) The force and power versus velocity for the one dimensional model described in the text. Here the spring coefficient $k = 15$. The line going through the power is a cubic spline fit used to more accurately determine the maximum value of the power. The velocity and power are both in units of 10^{-6} . (b) A plot of the efficiency of the motor as a function of the spring constant k . Four separate runs, each of 3×10^{10} steps were used to determine the error bars, for each data point shown.	55
3.1	Conceptual illustration of forces acting on a single polymer that are not due to hydrodynamic interactions. The blue vectors indicate the buckling forces due to kinesin walkers (tangent to polymer), the red vectors show the direction and relative magnitude of stiffness forces (in the direction of $d^4\mathbf{r}/ds^4$), and the green arrows indicate a restorative force keeping the base of the polymer approximately perpendicular to the binding surface.	62
3.2	Fluid speeds as a function of distance ρ from the stokeslet $\mathbf{F} = \hat{i}$. Solid curves are calculated using the full interaction tensor (3.2) and dashed lines are the far-field approximation (3.3). (a) $u_x(\rho)$ along the line $y = 0$; (b) $u_x(\rho)$ along the line $x = 0$; (c) $u_y(\rho)$ along the line $y = x$	66
3.3	Illustration of the geometry for which interaction tensor is derived in 3.3. While this is a three-dimensional system, we constrain polymers to the xy -plane.	69
3.4	Illustration of hydrodynamic forces between two example monomers in a planar polymer array. The green forces are the sum of non-hydrodynamic forces on the monomer (and by extension the force the monomer exerts on the surrounding fluid). $\vec{F}_{a \rightarrow b}$ and $\vec{F}_{b \rightarrow a}$ are the hydrodynamic forces on monomer b due to \vec{F}_a and the hydrodynamic force on monomer a due to \vec{F}_b , respectively.	70
3.5	Simulated metachronal wave formation for 128-polymer arrays in (a) circular and (b) planar geometries. In both cases, $k_{seen} = 0.1$, $k_{stiff} = 10.0$, $H = 1$	80
3.6	Full correlation functions for circular geometry with $H = 1$ and $k_{stiff} = 10$, with $k_{seen} = 0.1, 0.2$, and 0.3 (a-c, respectively). The correlation function at $\Delta i = 0$ for all of these values of k_{seen} are shown in (d).	82
3.7	Full correlation functions for planar geometry with $H = 1$ and $k_{seen} = 0.1$, with $k_{stiff} = 5.0, 10.0$, and 20.0 (a-c, respectively). The correlation function at $\Delta i = 0$ for all of these values of k_{stiff} are shown in (d).	83
3.8	Full correlation functions for circular geometry with $k_{stiff} = 10$, $k_{seen} = 0.2$, and $H = 1.0, 0.5$, and 0.1 (a-c, respectively). The correlation function at $\Delta i = 0$ for all of these values of H are shown in (d).	85

4.1	Predicted increase in temperature per watt at the center of the optical trap as a function of laser wavelength. The trap is assumed to only contain water a distance of 10 μm from a thermally conducting plate. The lower bound of the plot terminates at 600 nm because at this point the absorption coefficient of water becomes similar to that of glass, and the constant temperature boundary condition approximation becomes questionable.	95
4.2	Illustrations of some of the important forces applied to simulated polymers. (a) shows stiffness and kinesin drag forces that a polymer experiences regardless of the existence of other polymers (part of the F terms in Eq. 4.14), and (b) gives an example of how polymers exert hydrodynamic forces on one another via the interaction tensor \mathbb{G}	98
4.3	Quiver plots showing the direction of fluid flow in the vicinity of the polymers (black curves, with black circles indicating polarity) caught in the trap (dashed red circle). Color map is overlaid to show relative magnitudes of fluid velocity. (a) Uncorrelated circulation, using 32 polymers of length 8 and $k_{stiff} = 2.0$. (b) Correlated circulation, using 32 polymers of length 8 and $k_{stiff} = 0.5$. (c) Stasis, with 64 polymers of length 4 and $k_{stiff} = 0.5$. See the appendix for a link to animations of each of these.	101
4.4	Fluid speeds plotted with respect to distance to the center of the trap, with trap radius $R = 5$, for the three simulations shown in Figure 4.3. The black dashed line is an example of $v \propto 1/r^2$ as a guide to the eye.	104
4.5	Plots showing the power spectrum of (a) uncorrelated circulation and (b) stasis, with identical system parameters as shown in Fig. 4.3(a) and (c), respectively. Each plot shows the power spectrum for four system initializations. Units on both axes are arbitrary. The power spectrum for correlated circulation is not shown, as it is so heavily peaked at zero frequency. Plot (c) averages the initializations from plot the other plot on a log-log scale. The dashed lines are a guide to the eye for $ \hat{L} ^2 \sim \omega^{-3/2}$ (blue) and $ \hat{L} ^2 \sim \omega^{-1/2}$ (red)	106
4.6	Tables showing the observed behavior (S = stasis, C = correlated circulation, U = uncorrelated circulation) as a function of input parameters. In all tables except (d), monomer density remains constant – e.g. there are double the number of polymers of length 4 as there were of length 8 in a similar run. (a) Trap radius = 5.0, 256 monomers, $k_{Oseen} = 0.1$. (b) Trap radius = 10.0, 1024 monomers, $k_{Oseen} = 0.1$. (c) Trap radius = 5.0, 256 monomers, $k_{stiff} = 0.5$. (d) Trap radius = 5.0, polymer length = 8, $k_{Oseen} = 0.1$, $k_{stiff} = 0.5$	108

Abstract

Emergent Phenomena in Active Polymer Arrays

by

Stephen E. Martin

Three active matter systems involving long, flexible molecules (which we often refer to generally as polymers) are examined. Phenomena arising from these systems – be it pure prediction (as in chapters 2 and 4) or based on a known experiment (chapter 3) – are analyzed theoretically and through simulation. The first system we consider is a plate resting on a tilted polymer brush, where the ends of the polymers bind to sites on the plate and unbind in response to an incoming photon. We show that, under the right conditions, the plate will move in the direction of the polymer tilt, converting incoming light energy directly to mechanical energy. This mechanism was inspired by a similar mechanism already present in biology: the actin-myosin interface in muscle tissue. The second system is that of microtubule bundles confined between two parallel plates with one end bound to a surface, as studied experimentally by Sanchez et al [1]. In this experiment, the spontaneous formation of metachronal waves was observed. We show that this result can be reproduced using first-principles hydrodynamic simulations, and argue that these basic interactions are sufficient to explain the observed behavior. Finally, we propose an experiment in which microtubules are not bound to a surface, but rather confined to an optical trap. We show that, under the right conditions, drifting microtubules exhibit various phases, and can even align, circling the trap uniformly.

To my family:

My parents, Mike and Carol, who unconditionally give me wisdom from what
was.

Jon and Moryah, who show me what it means to stay focused on what is.

Elizabeth, Henry, Ruth, Jack, Aulani, and Short Round, who remind me to
think about what could be.

Acknowledgments

I would like to thank my advisor, Josh Deutsch, for his patience, guidance, and insight over the past several years as I gradually learned a number of physics, math, and computer science tools that fall well outside of the standard physics curriculum. I would also like to thank Onuttom Narayan and Sasha Sher for serving on my dissertation reading committee as well as my oral qualifying exam committee.

Further thanks go to my friends: Adam Coogan, Devon Hollowood, Sheena Shier, and Caitlin Johnson for helping me get through the first two years and for their continuing support, Alice Durand for so many unexpected baked goods at so many unexpected times, and to Taren Stinebrickner-Kauffman, Kelsey Kauffman, and Tuck Eskay for their selfless help in reviewing and offering input on this document.

The text of this dissertation includes reprints of the following previously published material and material that has been submitted for publication. The primary co-author for all of these is Josh Deutsch, who directed and supervised the research.

Chapter 2 – Photomechanical Energy Conversion [2]

I made computational and modeling contributions to the three dimensional model, especially in relation to randomly placed binding sites, and wrote sections of the paper.

Chapter 3 – Emergence of Metachronal Waves [3]

I wrote most of this paper, ran all of the simulations and performed the theoretical work.

The backbone of the simulation was written by Matthew Brunner, who co-authored the paper, but I added several important modifications.

Chapter 4 – Spontaneous Circulation of Active Microtubules [4]

I wrote all of this paper, ran all simulations, and performed nearly all analysis. The simulation used was adapted from the simulation used to simulate metachronal waves (chapter 3) so again the backbone of the simulation was written by Matthew Brunner, a coauthor.

Chapter 1

Introduction

Experiments in recent years show puzzling, counterintuitive, and potentially very useful emergent phenomena that arise in biological or synthetic systems that have some mechanism to convert energy from an external or internal source to organized motion. These types of systems, broadly speaking, have come to be called “active matter.” This may seem at first to be outside the realm of traditional physics. However, applying some of the same sorts of physical reasoning to biological systems has led to interesting and useful understanding of how and why they behave the way they do.

At the highest level, active matter systems are interesting because – while unpowered systems always seek equilibrium – active matter systems often remain out of equilibrium so long as their energy source is not depleted. A variety of phenomena in a number of systems have been studied: collective motion such as swarming, large-scale mixing, spontaneous stable vortex formation, and Brownian ratcheting have all been observed, sometimes with the same phenomenon being observed in seemingly unrelated

systems.

In what follows, we focus on and analyze such active matter systems, both treating the systems theoretically and through simulation. We specifically focus on the sorts of phenomena that arise when long, flexible molecules such as polymers and microtubules play an important function in the organized motion of the system.

1.1 Outline

In the sections that follow in this chapter, we first discuss the biology and interesting physics of what exactly makes matter “active”: motor proteins that are able to convert the chemical energy in ATP into mechanical energy. We specifically discuss the actin-myosin interface in muscle tissue (as this is relevant to the material in chapter 2) and the mechanism by which kinesin move along microtubules (relevant to chapters 3-4). The simulations in chapters 3 and 4 also make use of first-principles hydrodynamic interactions. For this reason, we also discuss in detail the fundamentals of fluid flow at the subcellular level (i.e. the Stokes regime) and how localized forces (stokeslets) affect this flow. We expand this analysis to address relevant boundary value problems, and give a qualitative comparison of these flows.

In chapter 2, a device is investigated that continuously and directly converts light into mechanical energy, using polymers and photodissociation. A polymer brush tethered to a surface, is brought into contact with a parallel plate a small distance above it that contains reaction sites where photodissociation of bound polymer and light can

occur. Under the appropriate conditions, the collective effect of these polymers is predicted to apply a force parallel to the plates, converting incoming light into mechanical work. Numerical work is carried out to understand this effect, a three dimensional Langevin simulation, solution to the Fokker Planck equation, and a one dimensional Monte Carlo simulation. Theoretical analysis of the Fokker Planck equation is used to study a model where equilibration of the unbound state occurs and equilibration to a metastable equilibrium is achieved in the bound state. It is shown that the work per cycle can be made much larger than the thermal energy but at the expense of requiring a greatly diminished photodissociation rate. Parameters are discussed in order to optimize mechanical energy conversion.

In chapter 3, we investigate the physical mechanism behind the spontaneous formation of metachronal waves in microtubule arrays in a low Reynolds number fluid. This has been of interest for the past several years, yet is still not well understood. We present a model implementing the hydrodynamic coupling hypothesis from first principles, and use this model to simulate kinesin-driven microtubule arrays and observe their emergent behavior. The results of simulations are compared to known experimental observations by Sanchez et al.[1, 5]. By varying parameters, we determine regimes in which the metachronal wave phenomenon emerges, and categorize other types of possible microtubule motion outside these regimes.

In chapter 4, we propose an experiment to demonstrate spontaneous ordering and symmetry breaking of kinesin-driven microtubules confined to an optical trap. Calculations involving the feasibility of such an experiment are first performed that

analyze the power needed to confine microtubules and address heating concerns. We then present the results of first-principles simulations of active microtubules confined in such a trap and analyze the types of motion observed by the microtubules as well as the velocity of the surrounding fluid, both near the trap and in the far-field. We find three distinct phases characterized by breaking of distinct symmetries and also analyze the power spectrum of the angular momenta of polymers to further quantify the differences between these phases. Under the correct conditions, microtubules were found to spontaneously align with one another and circle the trap in one direction.

1.2 Motor proteins and non-equilibrium

1.2.1 Actin and myosin

The interaction between myosin-II (a motor protein) and actin microfilaments are the basis for how skeletal muscles contract. A skeletal muscle is comprised of long muscle fibers, and each fiber is segmented into sections called sarcomeres. Each sarcomere is spanned internally by myosin structures, and is partially spanned on each end by actin microfilaments. The sarcomeres contract (and thus the muscle contracts) when the myosin structures exert an inward force on the actin microfilaments.

This is the question that is of particular interest: how does the myosin exert this inward force? Figure 1.1 shows a series of illustrations for how this cycle occurs. The myosin head is able to attach and detach to binding sites on the actin microfilament. Its lowest energy state is when bound to the filament – for this reason, muscles

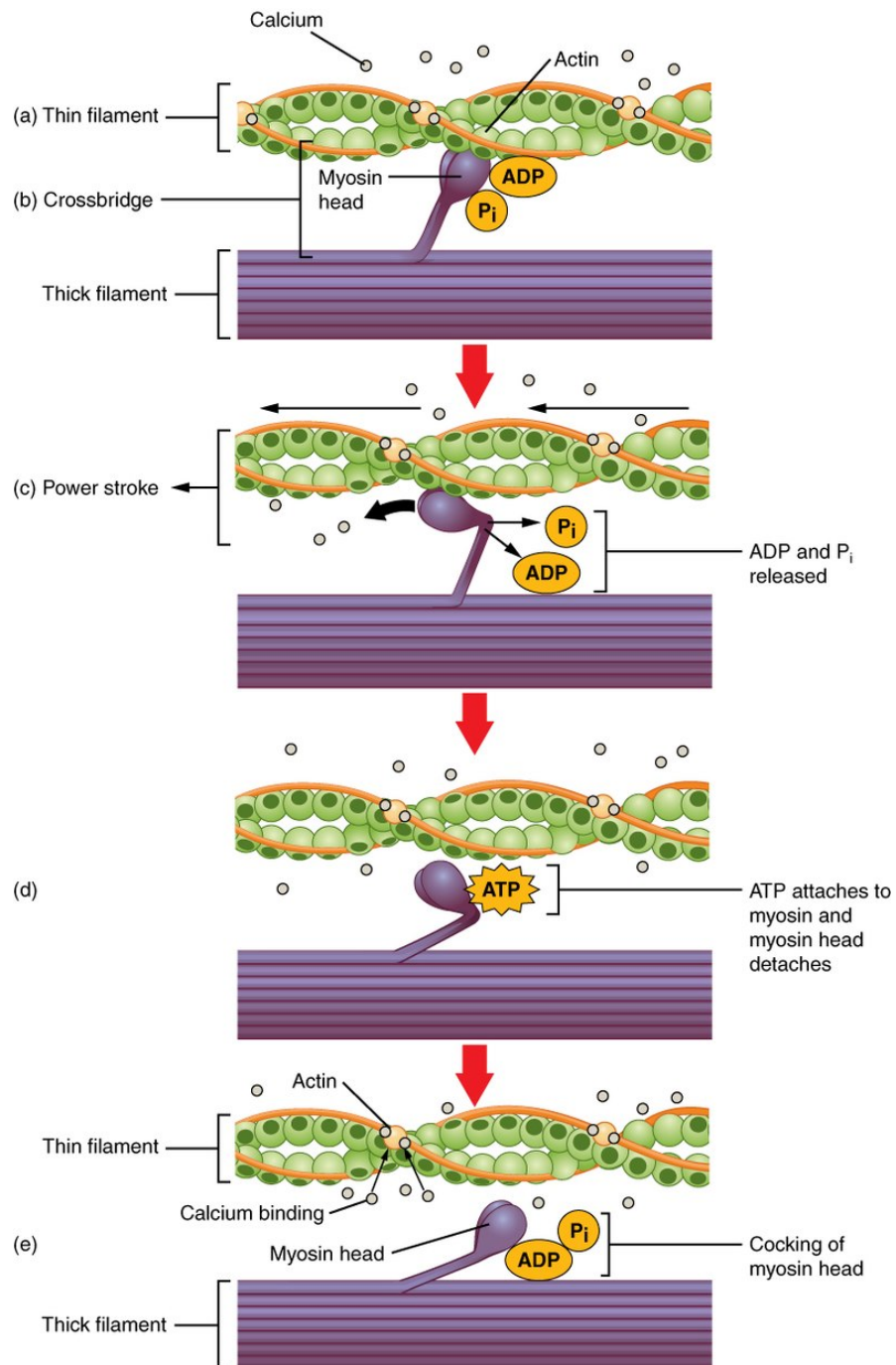


Figure 1.1: A series of illustrations depicting the mechanism by which muscles contract. Image credit to OpenStax Anatomy and Physiology.

that are not contracted have actin binding sites blocked by the protein tropomyosin (otherwise muscles would continually flex – this is the mechanism behind rigor mortis). When the myosin head binds, it undergoes a so-called “power stroke,” which pulls the microfilament. Once a myosin head is bound to a binding site, this bond is typically broken only by hydrolysis of ATP, and then the myosin falls back and is able to bind to another binding site and repeat the cycle.

This is a statistical process at its core. The motion of the unbound myosin head is Brownian, but because it is tilted back, when it does bind to the microfilament it tends to be in a place where it can exert an effective power stroke. This does not work every time – sometimes the myosin head is not far back enough, and sometimes the entire cycle does negative work on the microfilament. On average, though, each cycle results in positive work, and so the sarcomere contracts on the whole.

The device proposed in chapter 2 is inspired by this process. However, instead of converting chemical energy (in the form of ATP) to mechanical energy, we propose an entirely synthetic device that converts light into mechanical energy. It should be mentioned that, while the power stroke certainly makes the energy conversion process more efficient, it is not necessary for there to be a net work. We show in this chapter that having a tilted polymer brush, with binding sites that tend to fix the binding head at an angle, is enough to create a net positive average work per cycle.

1.2.2 Kinesin and microtubules

Kinesin is another motor protein that, like myosin, binds to a long, slender molecule called a microtubule. Microtubules are comprised of the protein tubulin, and are present in the cytoplasm of eukaryotes. Kinesin are also present throughout the cytoplasm, and when a kinesin comes near a microtubule, it has two heads (although it might be more appropriate to call these “feet”) which can bind to the microtubule. It then begins to walk – that is, each head binds and unbinds to the microtubule (hydrolyzing ATP), similar to how myosin binds and unbinds with actin microfilaments. The walk is made unidirectional due to the structure of the microtubule binding sites (all kinesins only walk a single direction on a given microtubule) and a process known as neck linker zippering [6]. A link to a video animation of this process is given in the appendix [7].

The function of this walking is to assist in cargo transport within the cell: some cellular structures that need to be distributed throughout the cell are too large to mix purely by diffusion. Instead, they bind to kinesin, which then walk them along microtubules to a relatively distant location.

From the perspective of active matter, the kinesin/microtubule interaction has an interesting consequence: as kinesin walk along a microtubule, there is a viscous drag force that opposes its motion. This imparts a force on the microtubule and (by Newton’s third law) an equal and opposite force on the fluid. This can cause interesting motions in both the fluid and in the microtubules, and if we wish to understand these motions it

is therefore critical to understand the physics of hydrodynamic forces at the microscopic level.

1.3 Stokes flow

In order to understand active matter in biological fluids, we must have a firm grasp of non-active fluid dynamics at the microscopic scale. We begin, then, by writing the full Navier-Stokes equation:

$$\left(\frac{\partial \mathbf{u}}{\partial t} + \mathbf{u} \cdot \nabla \mathbf{u} \right) = -\frac{1}{\rho} \nabla p + \nu \nabla^2 \mathbf{u} + \mathbf{F} \quad (1.1)$$

Here, $\mathbf{u}(\mathbf{r}, t)$ is the fluid velocity, $p(\mathbf{r}, t)$ is the fluid pressure, ρ is the density, ν is the kinematic viscosity, and $\mathbf{F}(\mathbf{r}, t)$ is the body force on the fluid. We can make this equation dimensionless by multiplying both sides by the quantity L/V^2 , where L and V are characteristic length and velocity scales, respectively. We can now redefine all of the quantities and derivatives to be dimensionless:

- $\mathbf{u} = \frac{\mathbf{u}}{V}$
- $p = \frac{p}{\rho V^2}$
- $\mathbf{F} = \frac{\mathbf{F}L}{V^2}$
- $\frac{\partial}{\partial t} = \frac{L}{V} \frac{\partial}{\partial t}$
- $\nabla = L \nabla$

Equation 1.1 then becomes

$$\left(\frac{\partial \mathbf{u}}{\partial t} + \mathbf{u} \cdot \nabla \mathbf{u}\right) = -\nabla p + \frac{1}{\text{Re}} \nabla^2 \mathbf{u} + \mathbf{F} \quad (1.2)$$

where $\text{Re} \equiv LV/\nu$ is called the Reynolds number. The Reynolds number allows us to make a very important observation: for microscopic biological phenomena, length scales are (by definition) quite small, as are velocities. For example, the kinematic viscosity of room temperature water is $\nu \approx 10^{-6} \text{ m}^2/\text{s}$. Microtubules (of considerable interest in the chapters that follow) have lengths on the order of around tens of microns, so $L \sim 10^{-5} \text{ m}$. If fluid is being driven by kinesin, then the characteristic speed is on the order of the kinesin walk speed, which is no more than $V \sim 10^{-6} \text{ m/s}$ [8, 9]. This gives $\text{Re} \sim 10^{-5}$, making the $\nabla^2 \mathbf{u}$ term in equation 1.2 dominant over the other derivative terms. We thus let the left hand side of equation 1.2 go to zero, leaving

$$-\nabla p + \frac{1}{\text{Re}} \nabla^2 \mathbf{u} + \mathbf{F} = 0 \quad (1.3)$$

This, along with the incompressibility condition $\nabla \cdot \mathbf{u} = 0$, is the definition of Stokes flow. Conceptually, the Reynolds number can be thought of as the ratio of inertial forces to viscous forces. Letting the Reynolds number equal zero therefore means that, in the Stokes regime, there is no inertia: a moving object with no external forces acting on it will stop immediately.

While mathematically useful for the elimination of the left hand side of equation 1.2, equation 1.3 is difficult to conceptualize due to its lack of dimensionality. The more common form of the Stokes flow equations is

$$\mu \nabla^2 \mathbf{u} - \nabla p + \mathbf{F} = 0; \quad \nabla \cdot \mathbf{u} = 0 \quad (1.4)$$

where $\mu = \rho\nu$ is the dynamic viscosity.

1.3.1 The stokeslet

Equation 1.4 is a good starting point, but it leaves the question of what to do about the body force, \mathbf{F} . For the microtubule-kinesin active matter system, the forces being exerted on the fluid are complicated: there is a drag force exerted by kinesin walkers, and the microtubules themselves experience external forces (which are then transferred perfectly to the fluid because there are no inertial effects). How can we begin to approach this? A key observation here is that Stokes flow allows for superposition of solutions, i.e. the resulting velocity \mathbf{u} and pressure p from two body forces \mathbf{F}_1 and \mathbf{F}_2 are

$$\mathbf{u} = \mathbf{u}_1 + \mathbf{u}_2 \quad \text{and} \quad p = p_1 + p_2, \quad (1.5)$$

where $\mathbf{u}_{1,2}$ and $p_{1,2}$ are the solutions to the Stokes equations for each force individually,

$$\mu \nabla^2 \mathbf{u}_{1,2} - \nabla p_{1,2} + \mathbf{F}_{1,2} = 0; \quad \nabla \cdot \mathbf{u}_{1,2} = 0 \quad (1.6)$$

This superposition is important, as it allows us to express forces in the fluid as sums and/or integrals of point forces in the fluid, similar to superposition problems in electricity and magnetism. This is, in essence, the strategy for summing forces on microtubules in chapters 3-4, and why the results of the derivations for a single point force in the following sections are so important to the method of simulation used.

Such a point force in the fluid is known as a stokeslet. A stokeslet at position \mathbf{R} with magnitude \mathbf{F} can be expressed as $\delta(\mathbf{r} - \mathbf{R})\mathbf{F}$, where $\delta(\mathbf{r})$ is the Dirac delta

function. The following sections show solutions to the Stokes equations with a single stokeslet and various boundary conditions.

1.3.2 Boundary-value problems with stokeslets

1.3.2.1 The Oseen tensor

We begin with a seemingly simple question: what is the solution to the Stokes equation for a single stokeslet immersed in “infinite” fluid (i.e. far from any boundaries)? This was solved exactly by Oseen nearly a century ago, but here we present a solution from Kim & Karilla [10, 11]. We begin with the Stokes equation with a stokeslet at the origin:

$$\mu \nabla^2 \mathbf{u} - \nabla p = -\mathbf{F} \delta(\mathbf{r}) \quad \nabla \cdot \mathbf{u} = 0 \quad (1.7)$$

These equations are linear in p and in \mathbf{u} , so we can express solutions as the products

$$p(\mathbf{r}) = \frac{\mathbf{P}(\mathbf{r}) \cdot \mathbf{F}}{8\pi\mu} \quad \mathbf{u}(\mathbf{r}) = \frac{\mathbb{J}(\mathbf{r}) \cdot \mathbf{F}}{8\pi\mu} \quad (1.8)$$

for some vector field $\mathbf{P}(\mathbf{r})$ and second-rank tensor $\mathbb{J}(\mathbf{r})$. Applying a Fourier transform to equation 1.7,

$$-i\mathbf{k}\hat{p} - \mu k^2 \hat{\mathbf{u}} = -\mathbf{F} \quad (1.9)$$

This allows us to insert the Fourier transform of our expected solutions in equation 1.8:

$$-i\frac{\mathbf{k}}{8\pi\mu} \hat{\mathbf{P}} \cdot \mathbf{F} - \frac{k^2}{8\pi} \hat{\mathbb{J}} \cdot \mathbf{F} = -\mathbf{F} \quad (1.10)$$

We can now use the identity $\mathbf{A}(\mathbf{B} \cdot \mathbf{C}) = (\mathbf{A} \otimes \mathbf{B}) \cdot \mathbf{C}$ to get rid of the \mathbf{F} terms, leaving

$$-\frac{i}{8\pi\mu} \mathbf{k} \otimes \hat{\mathbf{P}} - \frac{k^2}{8\pi} \hat{\mathbb{J}} = -\mathbb{I} \quad (1.11)$$

where \mathbb{I} is the identity matrix. We can similarly take the Fourier transform of the incompressibility condition $\nabla \cdot \mathbf{u} = 0$, and use equation 1.8 to deduce that

$$\hat{\mathbb{J}} \cdot \mathbf{k} = 0 \quad (1.12)$$

This suggests that equation 1.11 may be simplified by applying an inner product with \mathbf{k} :

$$\begin{aligned} -\frac{i}{8\pi\mu}(\mathbf{k} \otimes \hat{\mathbf{P}}) \cdot \mathbf{k} &= -\mathbf{k} \\ -\frac{ik^2}{8\pi\mu}\hat{\mathbf{P}} &= -\mathbf{k} \quad \rightarrow \quad \hat{\mathbf{P}} = -8\pi\mu \frac{i\mathbf{k}}{k^2} \end{aligned} \quad (1.13)$$

Now we apply an inverse Fourier transform,

$$\mathbf{P} = -8\pi\mu \nabla \left[\mathcal{F}^{-1} \left(\frac{1}{k^2} \right) \right] \quad (1.14)$$

This inverse Fourier transform is known: $\mathcal{F}^{-1} \left(\frac{1}{k^2} \right) = \frac{1}{4\pi r}$. We therefore have

$$\mathbf{P} = -2\mu \nabla \left(\frac{1}{r} \right) \quad (1.15)$$

Now we can solve for the velocity field. Inserting equation 1.13 into equation 1.11,

$$-\frac{\mathbf{k} \otimes \mathbf{k}}{k^2} - \frac{k^2}{8\pi} \hat{\mathbb{J}} = -\mathbb{I} \quad (1.16)$$

Solving for $\hat{\mathbb{J}}$,

$$\frac{\hat{\mathbb{J}}}{8\pi} = \frac{\mathbb{I}}{k^2} - \frac{\mathbf{k} \otimes \mathbf{k}}{k^4} \quad (1.17)$$

As before, we take an inverse Fourier transform, again using $\mathcal{F}^{-1} \left(\frac{1}{k^2} \right) = \frac{1}{4\pi r}$:

$$\frac{\mathbb{J}}{8\pi} = \frac{\mathbb{I}}{4\pi r} - \mathcal{F}^{-1} \left(\frac{\mathbf{k} \otimes \mathbf{k}}{k^4} \right) \quad (1.18)$$

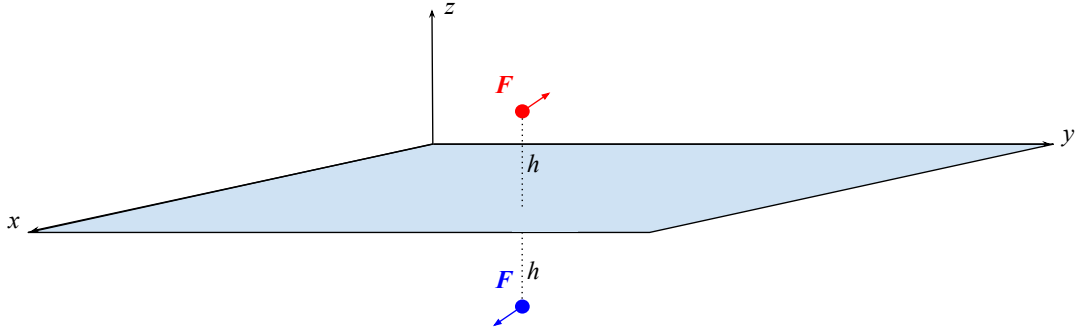


Figure 1.2: An illustration of the image charge system used by Blake to simplify the approach to solving the flow due to a stokeslet in the vicinity of an infinite plane. The real stokeslet (with arbitrary direction) is shown as the red dot ($z = h$). The infinite no-slip surface is the $z = 0$ plane, and the image stokeslet (blue dot) is placed at $z = -h$ with equal magnitude and opposite direction.

We give the following inverse Fourier transform without derivation:

$$\mathcal{F}^{-1} \left(\frac{\mathbf{k} \otimes \mathbf{k}}{k^4} \right) = \frac{\mathbb{I}}{8\pi r} - \frac{\mathbf{r} \otimes \mathbf{r}}{8\pi r^3} \quad (1.19)$$

Equation 1.18 therefore becomes

$$\mathbb{J} = \frac{1}{r} \left(\mathbb{I} + \frac{\mathbf{r} \otimes \mathbf{r}}{r^2} \right) \quad (1.20)$$

\mathbb{J} is known as the Oseen tensor. We can now combine our results for \mathbb{J} (equation 1.20)

and \mathbf{P} (equation 1.15) to give final expressions for the fluid velocity and pressure:

$$p(\mathbf{r}) = \frac{\mathbf{r} \cdot \mathbf{F}}{4\pi r^3} \quad \mathbf{u}(\mathbf{r}) = \frac{1}{8\pi\mu r} \left(\mathbb{I} + \frac{\mathbf{r} \otimes \mathbf{r}}{r^2} \right) \cdot \mathbf{F} \quad (1.21)$$

1.3.2.2 The Blake correction and the method of images

The derivation of the Oseen tensor is an important step, but many (if not most) relevant problems in biology are in environments where the “infinite fluid” approximation does not hold. In what follows, we show how a tool from electrostatics –

the method of images – can be used to arrive at an exact solution for a stokeslet near an infinite flat plane with no-slip boundaries (i.e. $\mathbf{u} = 0$ at the surface of the plane). This approach was first described by Blake in 1971 [12] in an effort to understand forces and flows on cilia near a glass slide.

Figure 1.2 shows the geometry of this problem. A single stokelet is placed a distance h above an infinite no-slip surface at $z = 0$, and we wish to find the velocity field everywhere. This problem is difficult, but it simplifies considerably if we construct an image stokeslet of equal magnitude and opposite direction directly below the real stokeslet at $z = -h$. With the image stokelet, we can use equation 1.21 to calculate the velocity field at $z = 0$:

$$\mathbf{u}(z = 0) = \frac{1}{8\pi\mu r} \left(\mathbb{I} + \frac{\mathbf{r} \otimes \mathbf{r}}{r^2} \right) \cdot \mathbf{F} - \frac{1}{8\pi\mu r'} \left(\mathbb{I} + \frac{\mathbf{r}' \otimes \mathbf{r}'}{r'^2} \right) \cdot \mathbf{F} \quad (1.22)$$

where $\mathbf{r} = x\hat{i} + y\hat{j} - h\hat{k}$ is the displacement from the real stokeslet to a point on the plate, and $\mathbf{r}' = x\hat{i} + y\hat{j} + h\hat{k}$ is the displacement from the image stokeslet to that same point. We immediately see that \mathbf{r} and \mathbf{r}' are equal in magnitude. In matrix form, equation 1.22 simplifies to

$$\mathbf{u}(z = 0) = \frac{h}{4\pi\mu r^3} \begin{pmatrix} 0 & 0 & x \\ 0 & 0 & y \\ x & y & 0 \end{pmatrix} \cdot \mathbf{F} = \frac{h}{4\pi\mu r^3} \begin{pmatrix} F_z x \\ F_z y \\ F_x x + F_y y \end{pmatrix} \quad (1.23)$$

While this is not zero, most of the elements of the matrix are zero, and this suggests that we may add some higher order multipoles to the image stokeslet such that $\mathbf{u} = 0$ everywhere in the $z = 0$ plane. Specifically, we can add what is known as a Stokes

doublet (two opposing stokeslets which are very close to one another), and what is known as a “source doublet” or “potential doublet” (a source and a sink that are very close to one another). Both of these constructs have been well-studied [13], so we state their fluid flows without derivation. The Stokes doublet flow field \mathbf{v} can be expressed as

$$\mathbf{v} = -\boldsymbol{\beta} \cdot \nabla \mathbf{u} = \frac{(\boldsymbol{\beta} \times \mathbf{f}) \times \mathbf{r}}{r^3} - \frac{(\mathbf{f} \cdot \boldsymbol{\beta})\mathbf{r}}{r^3} + 3\frac{(\mathbf{f} \cdot \mathbf{r})(\boldsymbol{\beta} \cdot \mathbf{r})\mathbf{r}}{r^5} \quad (1.24)$$

where \mathbf{u} is the flow due to a stokeslet (equation 1.21) and $\boldsymbol{\beta}$ is the vector separating the two stokeslets. \mathbf{f} is used as the magnitude and direction of the stokeslet here so as to avoid confusion with \mathbf{F} . The source doublet has a flow \mathbf{w} :

$$\mathbf{w} = -\frac{1}{2}\nabla^2 \mathbf{u} = -\frac{\boldsymbol{\delta}}{r^3} + 3\frac{(\boldsymbol{\delta} \cdot \mathbf{r})\mathbf{r}}{r^5} \quad (1.25)$$

where $\boldsymbol{\delta}$ is a vector in the direction of the displacement between the two sources, similar to $\boldsymbol{\beta}$, although we have also absorbed the strength of the stokeslet into $\boldsymbol{\delta}$ as we are free to tune both the separation and the magnitude. In the above two equations, we are able to choose the values of $\boldsymbol{\beta}$, \mathbf{f} , and $\boldsymbol{\delta}$ as we wish in order to make $\mathbf{u} = \mathbf{u}_{\text{stokeslet}} + \mathbf{u}_{\text{image}} + \mathbf{v} + \mathbf{w} = 0$ everywhere in the $z = 0$ plane. There is not a unique solution to this (the magnitudes of $\boldsymbol{\beta}$ and \mathbf{f} are somewhat arbitrary), but appropriate values for these terms are as follows:

$$\begin{aligned} \beta_{x,y} &= -\frac{hF_{x,y}}{4\pi\mu} & \beta_z &= \frac{hF_z}{4\pi\mu} & \mathbf{f} &= \hat{k} \\ \delta_{x,y} &= \frac{h^2F_{x,y}}{4\pi\mu} & \delta_z &= -\frac{h^2F_z}{4\pi\mu} \end{aligned} \quad (1.26)$$

Adding these together (equations 1.21, 1.24, and 1.25) gives the final solution for the

fluid velocity at location \mathbf{r} due to a stokeslet at \mathbf{x} :

$$\mathbf{u}(\mathbf{r}) = \mathbf{u}(\mathbf{r} - \mathbf{x}) - \mathbf{u}(\mathbf{r} - \mathbf{x} + 2h\hat{k}) + \mathbf{v}(\mathbf{r} - \mathbf{x} + 2h\hat{k}) + \mathbf{w}(\mathbf{r} - \mathbf{x} + 2h\hat{k}) \quad (1.27)$$

where, using the values in equation 1.26 and ignoring r^{-5} terms as they cancel by construction,

$$\begin{aligned} \mathbf{u}(\mathbf{r}) &= \frac{1}{8\pi\mu r} \left(\mathbb{I} + \frac{\mathbf{r} \otimes \mathbf{r}}{r^2} \right) \cdot \mathbf{F} \\ \mathbf{v}(\mathbf{r}) &= \frac{(\boldsymbol{\beta} \times \mathbf{f}) \times \mathbf{r}}{r^3} - \frac{(\mathbf{f} \cdot \boldsymbol{\beta})\mathbf{r}}{r^3} \\ \mathbf{w}(\mathbf{r}) &= -\frac{\boldsymbol{\delta}}{r^3} \end{aligned}$$

It is a straightforward (albeit tedious) exercise to verify that equation 1.27 indeed vanishes when $z = 0$. This fluid field was used previously in order to simulate cytoplasmic streaming in *Drosophila* oocytes [14], and a version of this simulation (modified to instead use the Liron-Mochon interaction discussed in the following section) was used to obtain results presented in chapters 3-4.

1.3.2.3 The Liron-Mochon solution

After Blake's paper in 1971, the method of images as an approach for solving boundary value Stokes flow problems gained popularity and was explored thoroughly over the following decade. One such study was completed by Liron and Mochon in 1976, in which they calculate the flow due to a stokeslet contained between two infinite parallel plates [15].

The method used to solve this is not as elegant as in the two previous sections. Because infinite image stokeslets are needed to solve this (see Figure 1.3), if we wish to

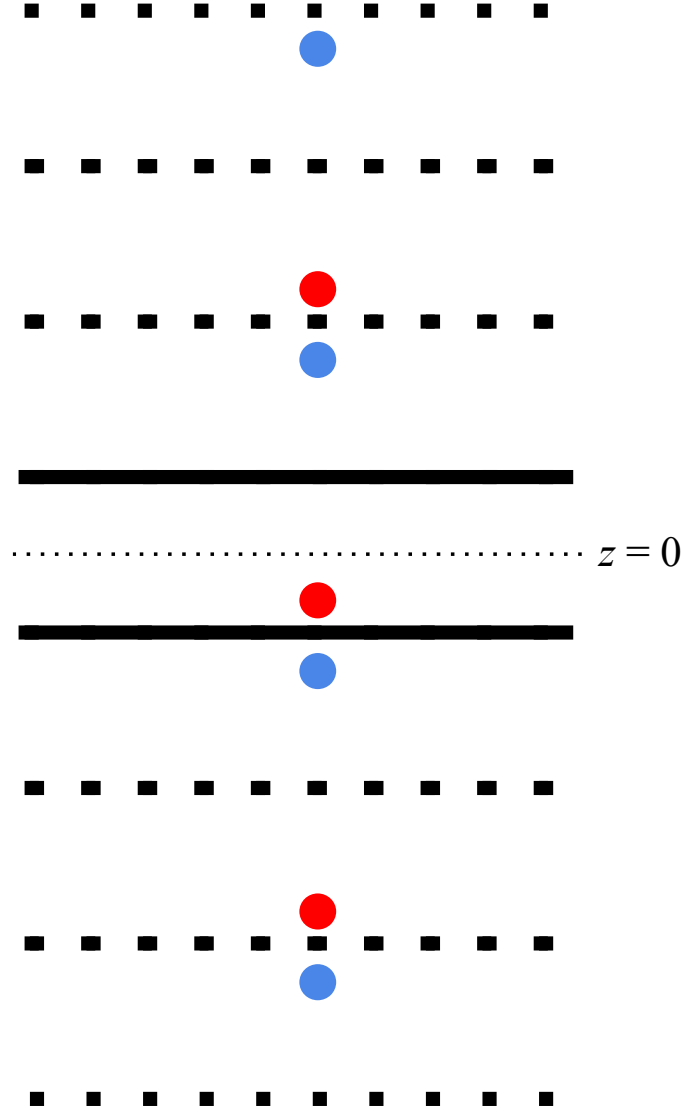


Figure 1.3: An illustration of the image charge system used by Liron and Mochon to simplify the approach to solving the parallel-plate stokeslet flow. The real stokeslet is shown as the red dot near $z = 0$, and the solid black lines are the plates. All other dots are image stokelets, with blue dots opposing the real stokeslet and red dots identical.

express the solution in terms of only images, we also would need to take into account the images of the Blake corrections (Stokes doublets and source doublets). This quickly becomes impractical, and a Fourier transform method is used (Blake also used a Fourier transform method, but this is not strictly required, as shown in the previous section).

Due to its complexity, the Liron-Mochon solution will not be printed in its entirety here. A simplified version of this solution, where the stokeslet is located halfway between the plates ($z = 0$) and points only in the xy -plane, is described in more detail in section 3.3.

1.3.2.4 Comparison of interaction tensors

Figure 1.4 contains plots showing the flow for each of the geometries explored above (free field, single infinite plane, parallel infinite planes). We immediately notice a few things about these – first, a stokeslet near a single plane has a sharper dropoff in fluid speeds in the far field than either of the other two geometries. Free-field stokeslet speeds drop off like $1/r$. Placing a stokeslet near a single plane reduces the fluid velocity because the velocity goes to zero near the plane – that is, at all points on the plane, the plane exerts a force on the fluid in the opposite direction as the stokeslet. The far-field flow in the parallel plane case, while also experiencing these forces from the no-slip planes, is somewhat bolstered by continuity in its quasi-2D geometry. Whereas the fluid could “escape” in the z -direction for a stokeslet near a single plate, the fluid does not have this option with two parallel plates, and this results in a stronger far-field behavior.

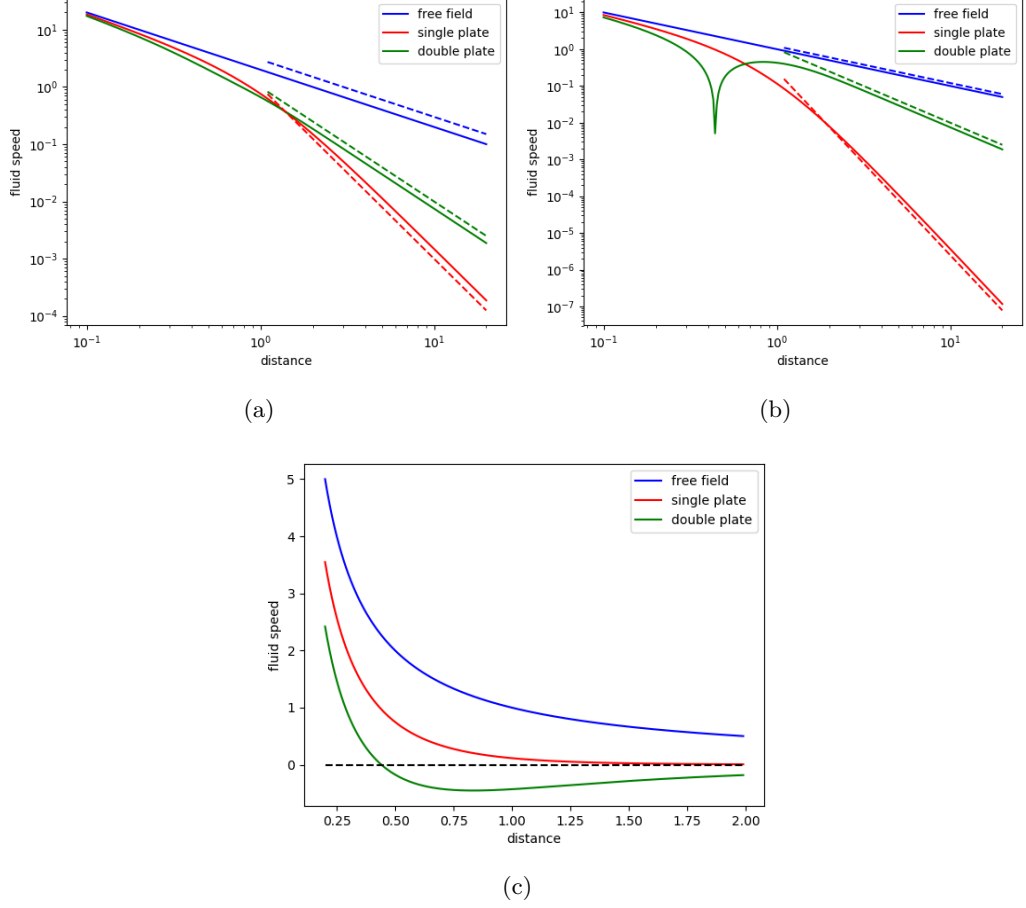


Figure 1.4: Comparison of flows due to a single stokeslet in the three geometries described in sections 1.3.2.1-1.3.2.3. All figures are for a stokeslet placed at the origin, pointing in the x -direction with unit magnitude. (a) $u_x(x, 0, 0)$, the fluid velocity in the direction of the stokeslet along the x -axis. The dashed lines are guides to the eye for $u_x \propto r^{-1}$ (blue), $u_x \propto r^{-2}$ (green), and $u_x \propto r^{-3}$ (red). (b) $|u_x(0, y, 0)|$, the fluid speed in the direction of the stokeslet along the y -axis. The dashed lines are guides to the eye for $u_x \propto r^{-1}$ (blue), $u_x \propto r^{-2}$ (green), and $u_x \propto r^{-5}$ (red). The cusp in the green curve indicates the transition from $u_x > 0$ (flowing in the same direction as the stokeslet) and $u_x < 0$ (flowing opposite the stokeslet). (c) A zoomed in view of $u_x(0, y, 0)$, showing backward flow for the parallel plate geometry.

This all being said, in the near field, we see how interesting the parallel plate case really is. While the free-field and single plate cases have qualitatively similar flow fields, the parallel plate geometry often has flows opposing the stokeslet. This opposition is potentially important for emergent phenomena in these geometries, as it can lead to counter-intuitive interactions (see section 3.3).

Chapter 2

Photomechanical Energy Conversion Using Polymer Brush Dissociation

2.1 Introduction

There are many proposals to convert light into mechanical energy using smart polymeric photo-responsive materials [16, 17, 18, 19, 20] or the synthesis of individual molecules that lead to rotary or linear motion [21].

Photoresponsive materials use a conformational change of a macroscopic collection of polymers in response to light or an external change in temperature and pH. This will cause a change in volume. If this process is reversible, which it is in many instances, this device can be cycled to derive mechanical energy [16, 17, 18].

In general, there are many scenarios leading to a change in configuration of a molecule in response to light [17]: *cis-trans* isomerization, zwitter ion formation,

radical formation, ionic dissociation, and ring formation/cleavage. If such light-sensitive elements are incorporated into a macromolecular system, this can in principle, through thermodynamic cycles, to conversion of light to mechanical power.

Remarkable advances in the design of molecules have led to prototypes for light-driven synthetic molecular motors [21]. Many of these are based on photoisomerization reactions that enable rotary motion of molecules when combined with thermal rotation steps [22, 23, 24, 21]. It has also been possible to make threading-dethreading systems [25, 21], and shuttle molecular rings [26, 21]. There has even been progress on a macroscopic level, such as creating droplet motion by modifying surface properties [27] or inducing mechanical deformation [28] similar to what is achieved with photo-responsive materials [16, 17, 18, 19, 20].

Much of the research in this area is inspired by biological machines such as myosin II that work by quite a different principle than man-made macroscopic motors [29]. Biological motors use chemical energy rather than photons to produce mechanical power however this difference does not affect the basic mechanism of operation. A myosin head can be thought of as being in two states, bound or unbound. Thermal noise in the unbound state can cause the head to bind to actin, producing a force. The hydrolysis of ATP releases energy causing the head to return to the unbound state. The biochemistry of a real motor protein is considerably more complicated, but by simplifying this description to one involving only these two states, the motion can be analyzed, and it is easily seen that electromagnetic energy can be used instead of chemical energy [30].

In this chapter, we investigate the use of photons in powering a two state motor system similar to biological motors. We consider creating motion between two surfaces that are very close together by placing an *asymmetric* polymer brush between them. This could potentially have advantages. A continuous source of light would create a motion that is constant on a macroscopic scale, that could for example, rotate the surfaces relative to each other. It would not require any additional mechanisms to keep it moving, other than the microscopic motion of molecules between the plates.

The device proposed here falls into a distinct category different than the experimental approaches above. It is not a macroscopic smart material that changes properties in response to external stimuli. The device described in the next section works on the scale of individual polymers, and the force generated on the surfaces is the sum of these molecules acting independently of each other. However it is unlike the chemical synthesis approach that requires different states of isomerization. The principles that it relies on are robust and just require photodissociation of polymer to a binding site, and, as in the case of biological motors, some degree of asymmetry. This asymmetry, plus a disruption of thermal equilibrium due to energy input are the two factors needed to convert energy from chemical or electromagnetic energy, to mechanical [30].

The chapter is organized as follows: The photo-mechanical system is described (The System) and rough estimates of its operation are given (Estimate of system parameters), including a discussion of its potential efficiency. In order to illustrate the characteristics that need to be understood, a three dimensional simulation of this device is carried out (Three dimensional model). The physics of this system is then

investigated in more analytical detail, starting with general considerations of its steady state behavior using Fokker Planck equations. The results will be used in subsequent sections. An exact description of this system is possible in steady state (Steady State Probability Distribution) and the resulting differential equation is solved numerically in one dimension (One dimensional solution). This allows to understand better how effective the asymmetry in the force produces power, and influences the direction that is taken in the rest of this work. Next, we study the useful large power stroke limit that is hard to probe numerically, but allows us to understand how the efficiency of this system is related to spring stiffness, metastability, relaxation times, and the photo-dissociation rate (Unbound Equilibration Model). We then use this model to understand the efficiency, using a one dimensional Monte Carlo model that is in this regime (Efficiency in large power stroke limit). Finally, we conclude on how the physics that has been learned might be useful in optimizing experimental parameters for such a system (Conclusions).

2.2 The System

The components needed to do constant photomechanical energy conversion are illustrated in Fig. 2.1.

- **A flat plate of semi-flexible polymer brushes.** Polymer brushes are polymers, each with one end tethered to a wall in a suitable solvent.
- **A parallel plate right above the brush.** These polymers are put in contact with a parallel plate close to the surface so that their ends are able to interact

with it.

- **The parallel plate contains an array of photoreactive binding sites.** It is crucial that these polymers bind with the surface in a sterically asymmetric way, so that the average binding orientation of each (called $\hat{\mathbf{n}}_a$ in Fig. 2.1) is the same.
- **At least one of the plates is transparent.** Light causes the unbinding of polymer ends from the photoreactive binding sites.
- **Binding catalyst.** To control the rate at which binding occurs, the binding of the end of the polymer to a binding site can be facilitated by the use of a catalyst. The concentration of the catalyst can be used to control the rate of binding.

In most of the discussion below, the polymers can be considered to be separated from each other by a sufficient distance so that we can ignore inter-chain interactions. The absorption of light causing unbinding will happen asynchronously. The ends tethered to the lower plates are at positions that are either random or incommensurate with the binding sites of the upper plate. Altogether this means that the motion of each polymer is uncorrelated with the others in the system.

The total effect of the forces acting on the plates can be used to perform work against a force acting on the upper plate. Because we assume that the number of polymers contributing is very large and are asynchronous, the net velocity of the upper plate v will be constant, as will be the net force acting on the plate.

In the following we will analyze the system and model it in different ways to better understand the power generation.

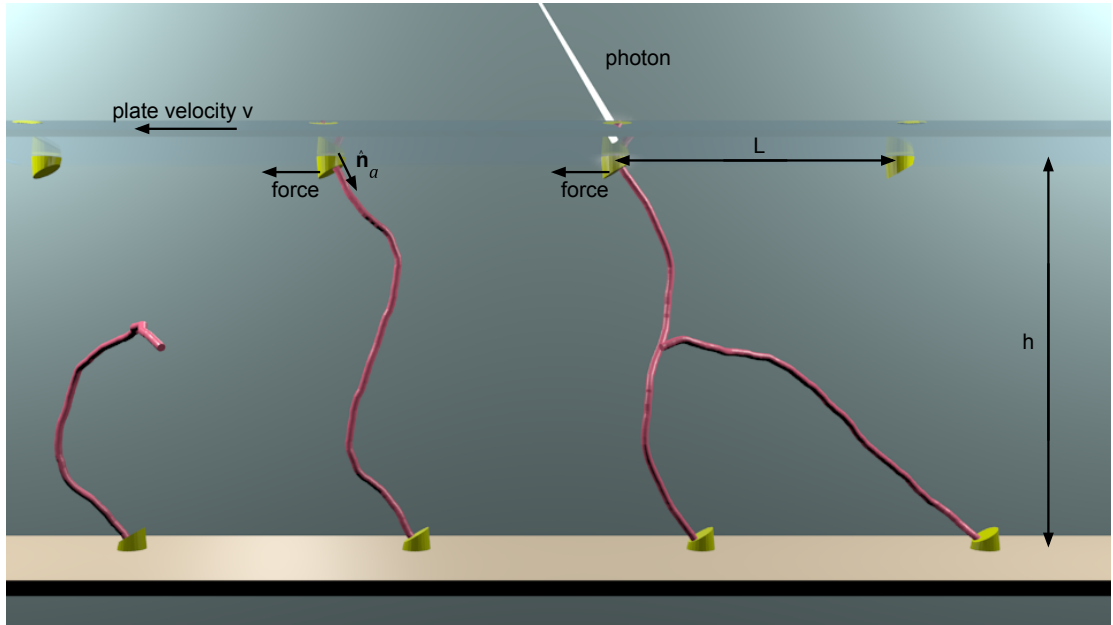


Figure 2.1: (a) A schematic of the light energy to mechanical converter. A polymer brush of semiflexible chains is put in contact with a plate a height h above the base, containing an array of anisotropic binding sites with preferred binding direction \hat{n}_a . Polymer ends are trapped by unlikely thermal fluctuations, applying a non-zero average force parallel to the plate. Photodissociation of the polymer ends with the binding sites releases the chain end that will move until it finds another site. The upper plate moves at a velocity v , thereby generating power. A single track is shown, and the separation between binding sites is L . The shape of the binding sites is meant only as a guide to the eye concerning the direction of \hat{n}_a , and is not necessarily an indicator of the binding sites' physical structure.

2.3 Estimate of system parameters

We will now make a crude estimate with realistic parameters of how well this device should work. We envisage separate one dimensional tracks of the kind shown in Fig. 2.1. We do not enforce that the arrangement of binding sites need be a square two-dimensional array—the spacing between the tracks could indeed be much greater than the distances between polymers on a single track. This would have the effect of limiting polymers to a particular track of binding sites. In reality, it might prove more efficacious to manufacture a square array of polymers and binding sites but we will allow two separate length scales in our analysis below.

We will assume a solar intensity of $I = 600W/m^2$ [31], and an average photon energy of $e = 2eV$ [32]. We will take the relaxation time of a polymer to be $\tau = 10^{-7}s$, which corresponds roughly to a polymer size of $3nm$ [33]. The number of unbinding events, if every photon was absorbed at a binding site, is $I/e \approx 2 \times 10^{21}/(m^2s)$. If the density of polymers is σ , then for all of these events to be utilized requires $I/e = \sigma/\tau$, or $\sigma = 2 \times 10^{14}/m^2$, which is a separation of $1/\sqrt{\sigma} \approx 70nm$. The amount of energy per step that is gained by a photo-dissociation event is of order $k_B T$. With such parameters, this is expected to yield an efficiency of order 1%. However, as we will show below, longer relaxation times allow for more energy per step, and this requires a higher polymer density. However the two dimensional density is limited by inter-chain interactions. In the case considered here, this density could be increased roughly by three orders of magnitude. However the relaxation time for this system depends exponentially on the

force generated, so a three order of magnitude increase in relaxation time would only increase the efficiency by a factor of about 7. Indeed, the detailed analysis presented below suggests that with optimal conditions, the efficiency of conversion is about 7%. To increase the efficiency of solar conversion further might require stacking devices.

There are other means of increasing the solar conversion efficiency by first converting solar radiation to lower energy photons. For example, two methods for doing this are fluorescent down-conversion of solar photons [34], or thermophotovoltaic down-conversion [35].

Further speculation on device efficiency is premature as there will undoubtedly be many unforeseen technical problems that will likely provide other obstacles to increasing device efficiency. However an efficiency for direct photo-mechanical conversion of about 7% is still a useful amount of power comparable to photovoltaic conversion with amorphous solar cells, and also because power is lost in electro-mechanical conversion, which is not a problem with direct mechanical energy conversion.

2.4 Three dimensional model

We start by simulating a three dimensional model of this system. There are two components to the system, the polymer and the binding sites. The polymer chain is modeled as having N links of fixed length. Denote the coordinates of the i th bead as \mathbf{r}_i . The elastic potential for the middle of the chain for the i th bead is

$$U_E(i) \equiv -\frac{C}{2}(|\mathbf{r}_{i+2} - \mathbf{r}_i|^2 + |\mathbf{r}_{i-2} - \mathbf{r}_i|^2) \quad (2.1)$$

where C is the stiffness constant.

The binding potential of the polymer has two components, an isotropic component U_i and directional component U_d . $U_i(r)$ is short range with a length scale r_s and scale V_a :

$$U_i(r) \equiv -V_a \exp\left(-\frac{Ar^2}{r_s^2 - r^2}\right), \quad (2.2)$$

where $A > 0$ is a parameter to adjust the shape of the potential. This binding potential is chosen for two reasons. First, $U_i(r)$ and all of its derivatives vanish as $r \rightarrow r_s$, thus all derivatives of these forces are continuous. Second, for small A , $U_i(r)$ rises quickly as $r \rightarrow r_s$, resulting in a large binding cross section. A plot of $U_i(r)$ for $A = 0.2$, $V_a = 60$, and $r_s = 1$ is shown in Fig. 2.2.

U_d uses a direction $\hat{\mathbf{n}}_a$ so that the difference between the last two end beads $\Delta\mathbf{r} = \mathbf{r}_1 - \mathbf{r}_0$ will give a minimum in U_d along that direction:

$$U_d(\mathbf{r}_0, \mathbf{r}_1) \equiv \left(\left| \frac{\Delta\mathbf{r}}{|\Delta\mathbf{r}|} - \hat{\mathbf{n}}_a \right|^2 + 1 \right) U_i(r). \quad (2.3)$$

The end attached to the lower surface is always bound. The other end can bind to a periodic linear array of binding sites equally spaced at a distance L .

There are two states that the system can be in, unbound, 0, and bound, 1. There are two parameters that control binding: the rate at which dissociation occurs c_1 , and the rate that dissociated ends can be rebound c_0 .

The distance between the lower and upper surface is h and their relative velocity is v .

The model was simulated with a Langevin equation, at finite temperature T .

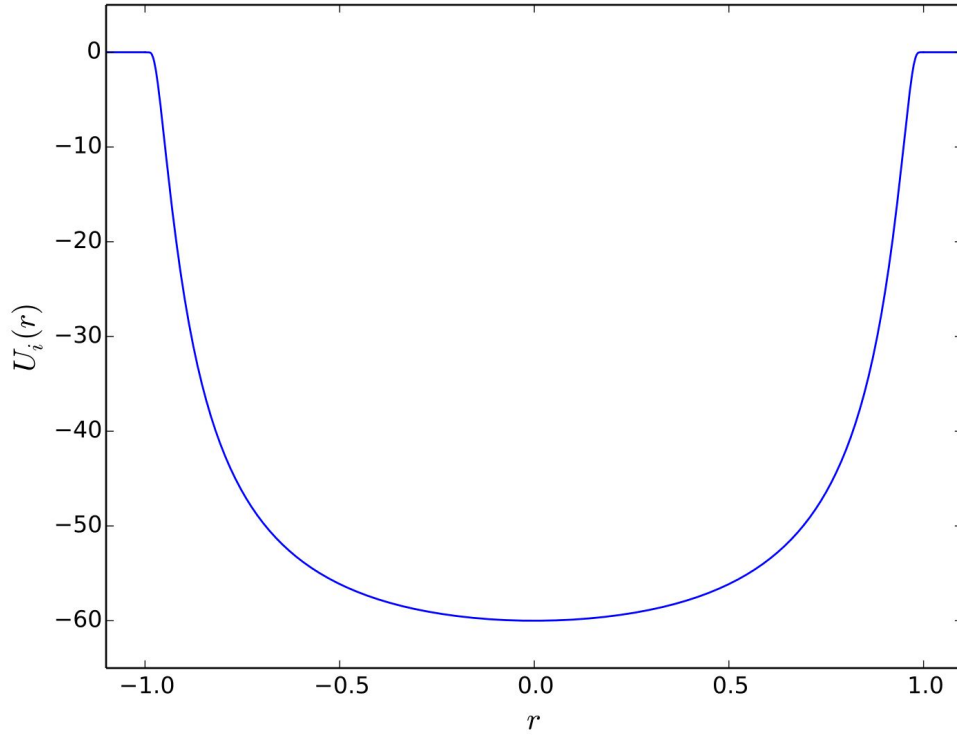


Figure 2.2: A plot of the isotropic binding potential $U_i(r)$ vs. r , for $A = 0.2$, potential well depth $V_a = 60$, and interaction length scale $r_s = 1$.

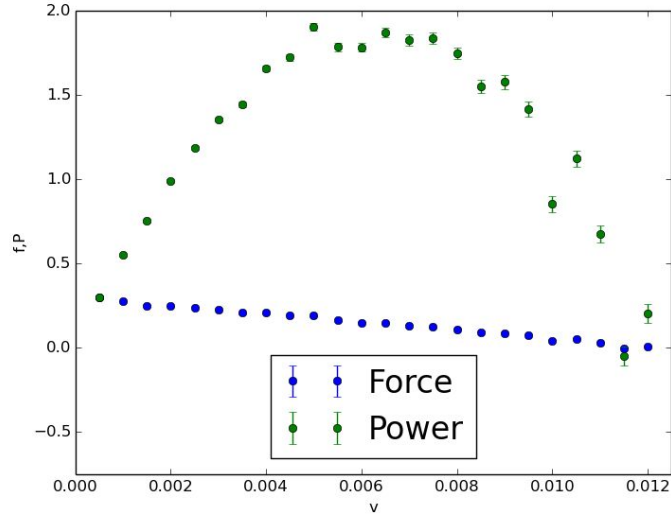
Although inertial effects are typically small at these microscopic scales, it was included for completeness. An algorithm was used that efficiently updates this system with fixed link lengths [36].

In order to increase the rate of binding, we also restrict the vertical motion of the polymer to be between the two plates (i.e. $0 \leq z \leq 1$ for $h = 1$) and the lateral motion (perpendicular to \mathbf{v}) to a maximum distance of $h/2$ from the binding sites. These restrictions are not unrealistic—we expect motion of polymers in such a device to lie between the two solid plates, and lateral motion may be restricted by the polymer stiffness and/or interactions with other polymers.

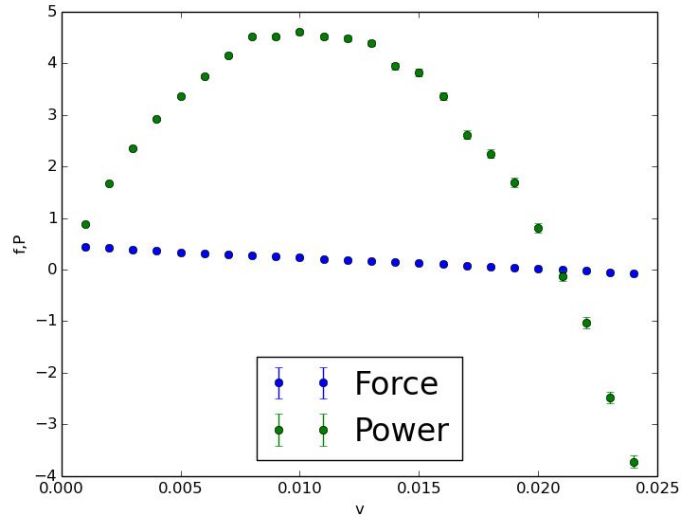
The simulation was run to determine how the force and power generated are influenced by the plate velocity. Fig. 2.3 shows the results of two simulations with different values of c_0 and c_1 . The parameters used were: 4 links, $h = 1$, spacing between binding sites $L = 2$, the direction of $\hat{\mathbf{n}}_a$ is $\pi/4$, $V_a = 60$, link length of 1, particle mass of 1, $C = 0.5$, $r_s = 1.0$, $A = 0.2$, and a coefficient of damping of 10.

The force generated is highest approaching zero velocity and decreases until it becomes negative, at which point it is taking mechanical energy to move it at such high speeds. Qualitatively, this is the point where frictional drag dominates over photo-energy conversion.

Note that the highest force f , peak operating velocity, and power $P = f\mathbf{v}$ are all seen for $c_0 = c_1 = 0.4$. Higher maxima in the power are generally seen with increasing c_0 and c_1 . However, this higher power is at the expense of efficiency, as higher dissociation rates imply a higher photon flux.

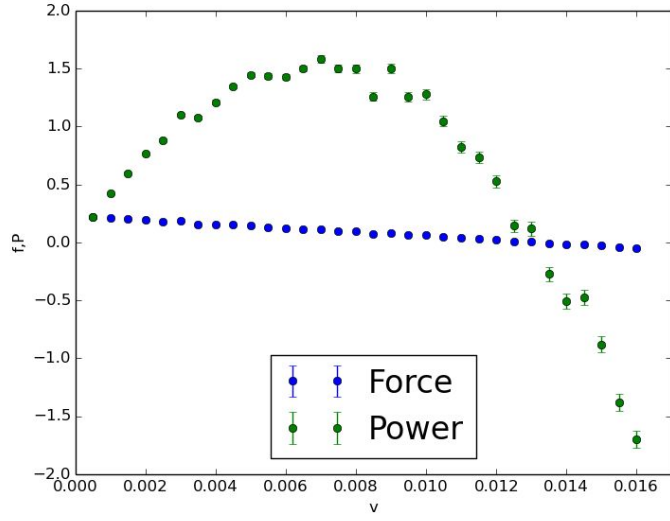


(a)

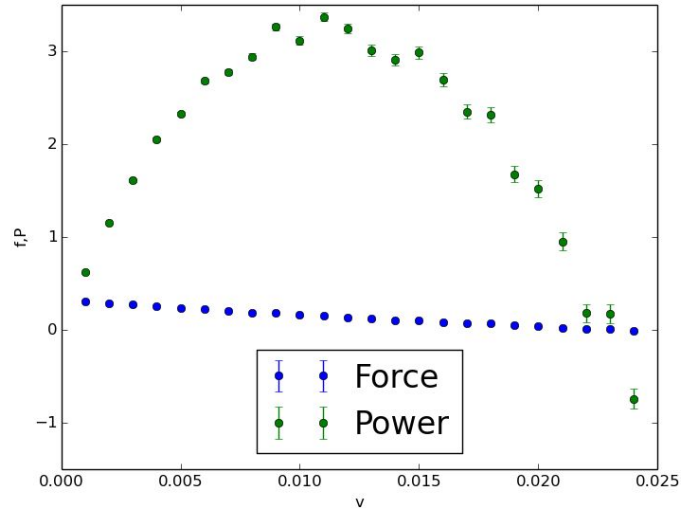


(b)

Figure 2.3: The average force f and the power $P = fv$ measured as a function of the relative velocity between the plates v . For clarity, the power is multiplied by 2000. There were 4 links, with a plate separation of $h = 1$, spacing between binding sites $L = 2$, the direction of $\hat{\mathbf{n}}_a$ (that is, the binding angle) is $\pi/4$, $V_a = 60$, $A = 0.2$, link length of 1, stiffness constant $C = 0.5$, potential range $r_s = 1.0$, and a coefficient of damping of 10. The coefficients of binding and unbinding, respectively, are (a) $c_0 = c_1 = 0.05$, and (b) $c_0 = c_1 = 0.4$.



(a)



(b)

Figure 2.4: The average force f and the power $P = fv$ measured as a function of the relative velocity between the plates v . The binding sites are placed randomly, with average binding site separation $\bar{d} = 2$ and minimum binding site separation $d_{min} = 0.1$. Other than this, the same parameters and scaling are used as in Fig. 2.3: (a) $c_0 = c_1 = 0.05$, and (b) $c_0 = c_1 = 0.4$.

It is also of interest to determine if this photomechanical effect persists if the binding sites are no longer periodic but instead are arranged at random. To investigate this situation, we place the binding sites so that the probability distribution of spacings, d , between binding sites followed Poisson statistics, that is $p_{spacing}(d) \propto \exp(-d/\bar{d})$. Here \bar{d} is the average spacing between sites. However we also must introduce a lower cutoff, d_{min} , to prevent binding sites from overlapping so that when generating the next site's position, we reject spacings less than this cutoff. For our simulations, we set $\bar{d} = 2$ and $d_{min} = 0.1$. The purpose of this is to simulate possible experiments in which a rigidly periodic array of binding sites is impractical to construct.

Fig. 2.4 shows the results of these simulations. The results are strikingly similar to those found with periodic sites. This shows that, at least for this parameter regime, the motor function of the device does not depend strongly on the regular placement of binding sites—an optimistic result from an experimental perspective.

2.5 Steady State Probability Distribution

To understand the above simulation in more detail requires a better understanding of the mechanisms involved. There have been a very large number of works on the theory of motor proteins [37, 29], and we will follow the two state approach mentioned above of Prost *et. al.* [30, 38]. The major difference is that they considered the two states to be periodic potentials, whereas here we model the system to more closely mimic the particular device we are investigating allowing the exploration of force versus

velocity. Hence instead of considering the position of a particle moving between two periodic potentials, we consider the unbound state to have a free end described as moving in a bound potential around the tether point. Likewise, because of this tethering, the bound state potential is not periodic but has a periodic component as we will describe in detail below. Here we consider the probability distribution for this system in steady state, which is described by a Fokker Planck equation.

Initially to calculate the power that is produced, we will concentrate on the low velocity limit, with the two plates moving so slowly that this motion does not affect chain conformations appreciably. In this way, we can consider the average force exerted between the plates by a polymer in steady state in the limit $v = 0$ so that the tether point is not moving. It is most convenient to let the point at which the polymer is tethered to the bottom plate be a variable parameter $\mathbf{r}' = x'\hat{\mathbf{x}}$. With this point fixed, we consider the distribution of the other end of the polymer \mathbf{r} . We will assume that the internal dynamics of the chain are much faster than the binding and unbinding rates, so that the only degrees of freedom are \mathbf{r} , and if the polymer is bound, $i = 0$ is unbound and $i = 1$ is bound. Therefore the probability distribution of the system can be described by a function $P_i(\mathbf{r}; \mathbf{r}')$. The equations describing this are [30]

$$\partial_t P_0(\mathbf{r}) = \nabla \cdot (\nabla - \mathbf{f}_0) P_0(\mathbf{r}) - c_0 P_0(\mathbf{r}) + c_1 P_1(\mathbf{r}) \quad (2.4a)$$

$$\partial_t P_1(\mathbf{r}) = \nabla \cdot (\nabla - \mathbf{f}_1) P_1(\mathbf{r}) + c_0 P_0(\mathbf{r}) - c_1 P_1(\mathbf{r}) \quad (2.4b)$$

where the last \mathbf{r}' argument of P has been left out for notational simplicity. The units here absorb the diffusion coefficient D together with the time, that is t as used here and

below is really D times the time. The force terms have absorbed a temperature factor T , that is \mathbf{f}_i is really the force times $1/k_B T$. Those forces \mathbf{f}_0 and \mathbf{f}_1 are the total forces acting on the upper end of the chain. When the system is unbound, it is the force of a (possibly) nonlinear spring

$$\mathbf{f}_0 = \mathbf{f}_s(\mathbf{r} - \mathbf{r}'). \quad (2.5)$$

When the system is bound we have total force is the sum of the spring force and a periodic force representing the binding potential

$$\mathbf{f}_1 = \mathbf{f}_s(\mathbf{r} - \mathbf{r}') + \mathbf{f}_p(\mathbf{r}). \quad (2.6)$$

These forces are assumed to be conservative, \mathbf{f}_s and \mathbf{f}_p are derived from potentials that respectively are V_s and V_p .

In steady state the left hand sides of Eqs. 2.4a-b are zero. We can eliminate the last two terms on the right hand side to obtain

$$\hat{O}_0 P_0 + \hat{O}_1 P_1 = 0, \quad (2.7)$$

where

$$\hat{O}_i \equiv \nabla \cdot (\nabla - \mathbf{f}_i), \quad i = 0, 1. \quad (2.8)$$

We can now calculate the average force exerted by the two potentials, is zero. In steady state, we multiply Eq. 2.7 by \mathbf{r} and integrate with respect to x , y and z . Then using integration by parts, we have boundary terms at infinity. Because we are assuming that the spring potential grows without bounds, this confines P_0 , and P_1 , to a neighborhood

around \mathbf{r}' , so that the boundary terms vanish. We are then left with

$$\langle \mathbf{f} \rangle = \int (\mathbf{f}_0 P_0 + \mathbf{f}_1 P_1) d^3 \mathbf{r} = 0 \quad (2.9)$$

as is expected because r is confined to a region of space so that the average velocity, and hence average force, will be zero.

We can also determine the total fraction of time spent in the bound or unbound states in steady state. First, because the probability of being in any state is unity,

$$\int (P_0(\mathbf{r}) + P_1(\mathbf{r})) d^3 \mathbf{r} = 1. \quad (2.10)$$

Then by integrating Eq. 2.4a over all space, the derivative term integrates to 0, giving

$$\int (-c_0 P_0(\mathbf{r}) + c_1 P_1(\mathbf{r})) d^3 \mathbf{r} = 0 \quad (2.11)$$

hence

$$\int P_0(\mathbf{r}) d^3 \mathbf{r} = \frac{c_1}{c_0 + c_1}, \quad \int P_1(\mathbf{r}) d^3 \mathbf{r} = \frac{c_0}{c_0 + c_1}. \quad (2.12)$$

To obtain the power produced by this device, we are not interested in the total force acting on the upper chain end because this includes the binding potential, but the average force due to the spring acting on the lower plate $\langle f_s \rangle$. We would like to calculate the work done in moving the lower point \mathbf{r}' by one period of \mathbf{f}_p . After moving one period the system is statistically identical to its starting point, and this method can therefore give the work done in moving n such periods. Denoting the period of \mathbf{f}_p by L , we would like to calculate

$$\begin{aligned} W_l &= \int_0^L \hat{\mathbf{x}} \cdot \langle \mathbf{f}_s \rangle dx' \\ &= \int_0^L \int \hat{\mathbf{x}} \cdot \mathbf{f}_s(\mathbf{r}, x' \hat{\mathbf{x}}) (P_0(\mathbf{r}, x' \hat{\mathbf{x}}) + P_1(\mathbf{r}, x' \hat{\mathbf{x}})) d^3 \mathbf{r} dx' \end{aligned} \quad (2.13)$$

Using Eq. 2.5 and 2.6, this may be rewritten as

$$W_l = \int_0^L \int \hat{\mathbf{x}} \cdot (\mathbf{f}_0 P_0(\mathbf{r}, x' \hat{\mathbf{x}}) + (\mathbf{f}_1 - \mathbf{f}_p) P_1(\mathbf{r}, x' \hat{\mathbf{x}})) d^3 \mathbf{r} dx' \quad (2.14)$$

Eq. 2.9 then yields

$$W_l = - \int_0^L \int \hat{\mathbf{x}} \cdot \mathbf{f}_p(\mathbf{r}) P_1(\mathbf{r}, x' \hat{\mathbf{x}}) d^3 \mathbf{r} dx'. \quad (2.15)$$

In thermal equilibrium, where the transition rates c_0 and c_1 are both zero, we recover the Gibbs distribution. Let us assume, that the system starts, and therefore remains in state $i = 1$. Then

$$P_1(\mathbf{r}, \mathbf{r}') = \frac{e^{-V_1}}{Z} \quad (2.16)$$

where the partition function

$$Z(\mathbf{r}') = \int e^{-V_1} d^3 \mathbf{r} \quad (2.17)$$

which will also have periodicity of L . In this case W_l can be easily calculated because $P_0 = 0$ and $\mathbf{f}_s = -\nabla V_s(\mathbf{r} - \mathbf{r}') = \nabla' V_s(\mathbf{r} - \mathbf{r}')$. So

$$\begin{aligned} W_l &= \int_0^L \int (\partial_{x'} V_s(\mathbf{r}, x' \hat{\mathbf{x}})) \frac{e^{-(V_s(\mathbf{r} - \hat{\mathbf{x}} x') + V_p(\mathbf{r}))}}{Z(x')} d^3 \mathbf{r} dx' \\ &= -T(\log Z(L) - \log Z(0)) = 0 \end{aligned} \quad (2.18)$$

as it must be by the second law of thermodynamics.

2.6 One dimensional solution

In order to investigate how the power conversion depends on the forces acting on this system, it is important to simplify the three dimensional model to obtain a

minimal model that depends on far fewer parameters. Therefore we investigate this model in one dimension.

A key point to understand is how asymmetry in the form of the force produces power. With symmetric spring and binding potentials, it is easily seen by symmetry that no net power can be produced from this system. We now ask how asymmetry affects the results. We will see that even with a large asymmetry in the spring potential, the work defined by Eq. 2.13 is very small. Simulations using Monte Carlo or Langevin equations are too noisy to provide good estimates. We therefore instead use a more analytical approach.

The coupled Focker Planck Eqs. 2.4 (a) and (b) can be solved to produce an equation only involving one distribution function, P_1 in steady state. Using the definitions in Eq. 2.8, we can eliminate P_0 .

$$(\hat{O}_0\hat{O}_1 - c_1\hat{O}_0 - c_0\hat{O}_1)P_1 = 0 \quad (2.19)$$

which is a fourth order equation in spatial variables.

Now we restrict the analysis to one dimension. In this case, $\hat{O}_i = \partial_x(\partial_x - f_i)$ so we can integrate with respect to x . We note that because the spring confines P_1 to a localized region, it will go to zero as $x \rightarrow \pm\infty$. Therefore the integration constant must also be zero

$$((\partial_x - f_0)\partial_x(\partial_x - f_1) - c_1(\partial_x - f_0) - c_0(\partial_x - f_1))P_1 = 0 \quad (2.20)$$

which is a third order linear differential equation.

Eq. 2.20 was solved by the shooting method [39]. The boundary conditions were obtained by considering the system far from x' where P_0 is very small. In that domain, f_p was artificially cutoff so that $f_0 = f_1 = f_s$. Because the potential there is no longer changing between the two states, the solution is that of a system in thermal equilibrium. The solutions were required to match to these thermal solutions in this regime, far from x' . The equation was solved with three different initial conditions. An appropriate linear combination of these were constructed to match the boundary conditions as just described.

The periodic binding potential that was used is

$$V_p = A_1 \cos(x) - A_2 \sin(2x) \quad . \quad (2.21)$$

We first consider asymmetry in V_s but with symmetric functions V_p , that is, $A_2 = 0$ in Eq. 2.21.

$$V_s(x) \equiv \frac{1}{2}kx^2 - \frac{a}{1 + (b(x - d))^2}. \quad (2.22)$$

The first term describes a linear spring with spring constant k , the second adds an asymmetric dip. The parameters are chosen so that this dip is close in potential to the one created predominantly by the linear term, $k = 4$, $a = 8$, $b = 2$, and $d = 2$. The function is plotted in Fig. 2.5.

Plots are shown in Fig. 2.6 of $P_1(x)$ within a period for four values of x' : $-\pi$, $-\pi/2$, 0 , $\pi/2$.

By integrating using these distributions, Eq. 2.15, the work can be obtained.

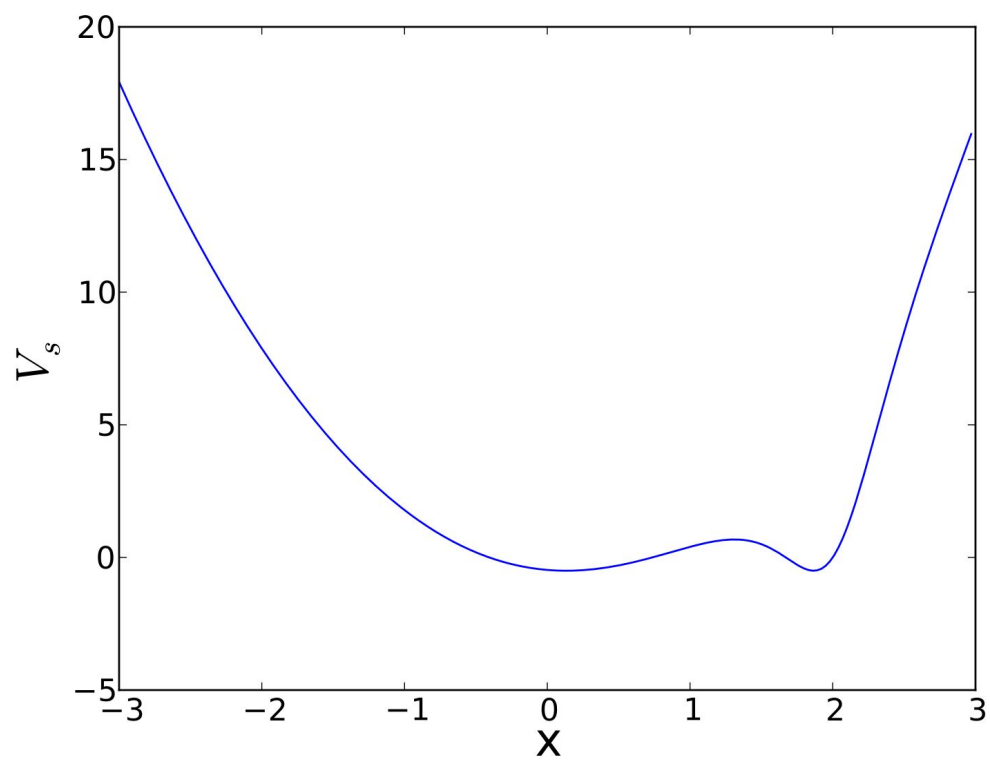


Figure 2.5: An asymmetric spring potential used to tether the chain. It has a second dip at approximately $x = 2$

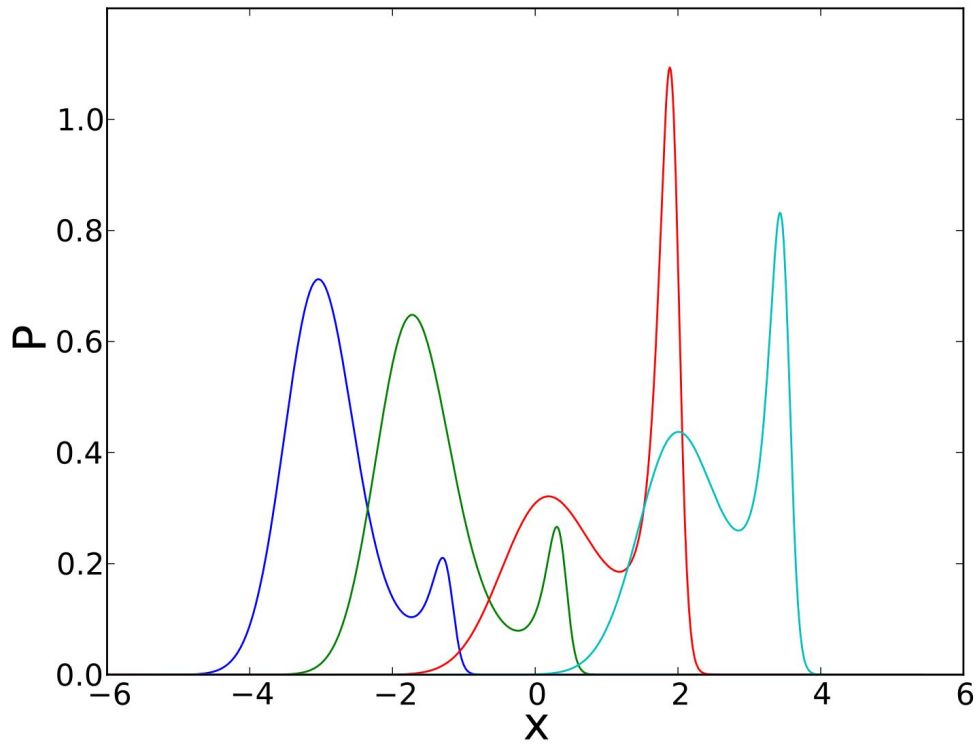


Figure 2.6: Plots of the probability distribution of P_1 as a function of position x for $x' = -\pi$, $-\pi/2$, 0 , and $\pi/2$ for the asymmetric spring model Eq. 2.22.

With $c_0 = 0.025$ and $c_1 = 0.05$ the work $W_L = 0.00080954$. With the c_i 's 10 times those values, $c_0 = 0.25$, and $c_1 = 0.5$, $W_L = 0.0025$.

Now we consider the case of a linear spring so that the nonlinear parameter $a = 0$ in Eq. 2.22. Instead we make the periodic potential asymmetric by setting $A_1 = A_2 = 2$ in Eq. 2.21, still with $c_0 = 0.25$, and $c_1 = 0.5$. Fig. 2.7 plots $P_1(x)$ within a period for the same four values of x' in Fig. 2.6.

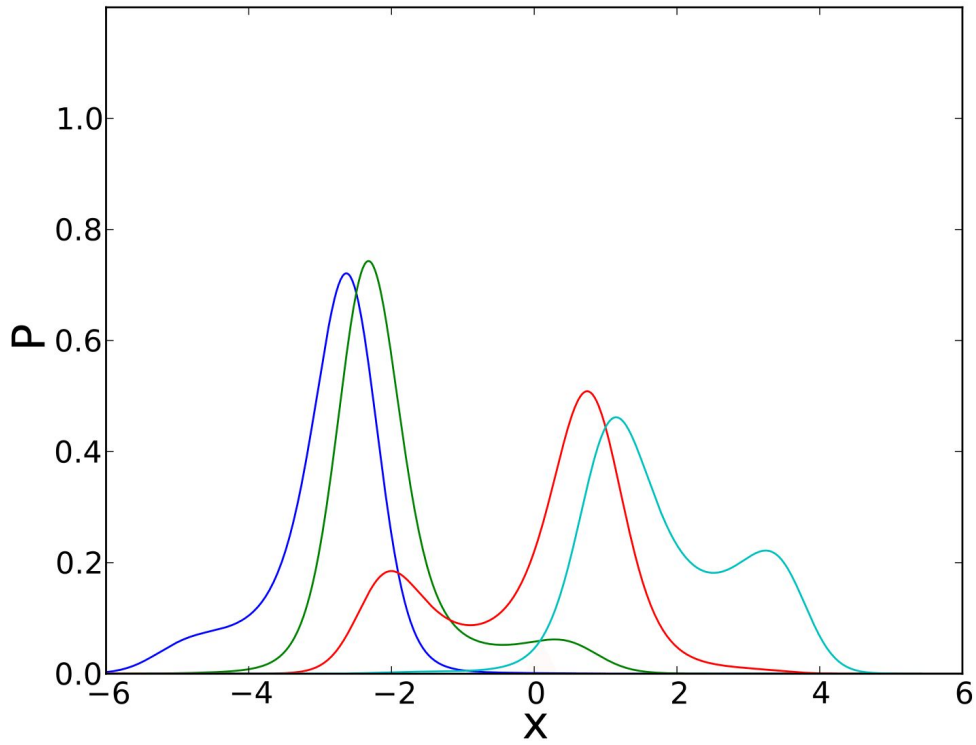


Figure 2.7: Plots of the probability distribution of P_1 as a function of position x for the values of x' shown in Fig. 2.6, but for an asymmetric periodic potential and a linear spring.

In this case, the work $W_L = -0.1596$.

What the numerical results have shown is that asymmetry in the spring potential is quite ineffective at producing work, whereas asymmetry in the periodic binding potential is much more effective. We shall use this result below and concentrate on systems with symmetric spring potentials, but asymmetric binding potentials.

2.7 Unbound Equilibration Model

It is worthwhile to understand in more detail what constrains the maximum force of photo-mechanical conversion by tuning the potentials employed and the binding rate, and to ask how the design will depend on the flux of photons. We are limited in our choice of the potentials V_0 and V_1 that both must be bounded. In this system, the unbound potential is not periodic which limits the amount of power that can be generated. In cases considered earlier [30], where both potentials are periodic, it is possible to get much more efficient motion by alternating between states with different potential maxima. However this is not relevant to our system.

To understand this better, it is useful to examine a limit where we can treat the system analytically. We therefore examine the case where the binding rate of an unbound chain is sufficiently small, so that we can regard it in thermal equilibrium.

The model is illustrated in Fig. 2.8. We take the unbound potential to be that of a linear spring below a cutoff

$$V_s = V_0 = \begin{cases} k(x - x')^2/2, & \text{if } -l_c < (x - x') < l_c. \\ \infty, & \text{otherwise.} \end{cases} \quad (2.23)$$

we choose the spring coefficient k such that $l_c \exp(-kl_c^2/2) \ll 1$. Below, we will take $l_c = L/2$ or ∞ .

The periodic potential V_p is taken to be localized at periodic points (with a separation of L) that rapidly vary from a large maximum V_{max} to a minimum V_{min} , as shown. We take the region over which this happens to be negligibly small compared to other length scales in the problem.

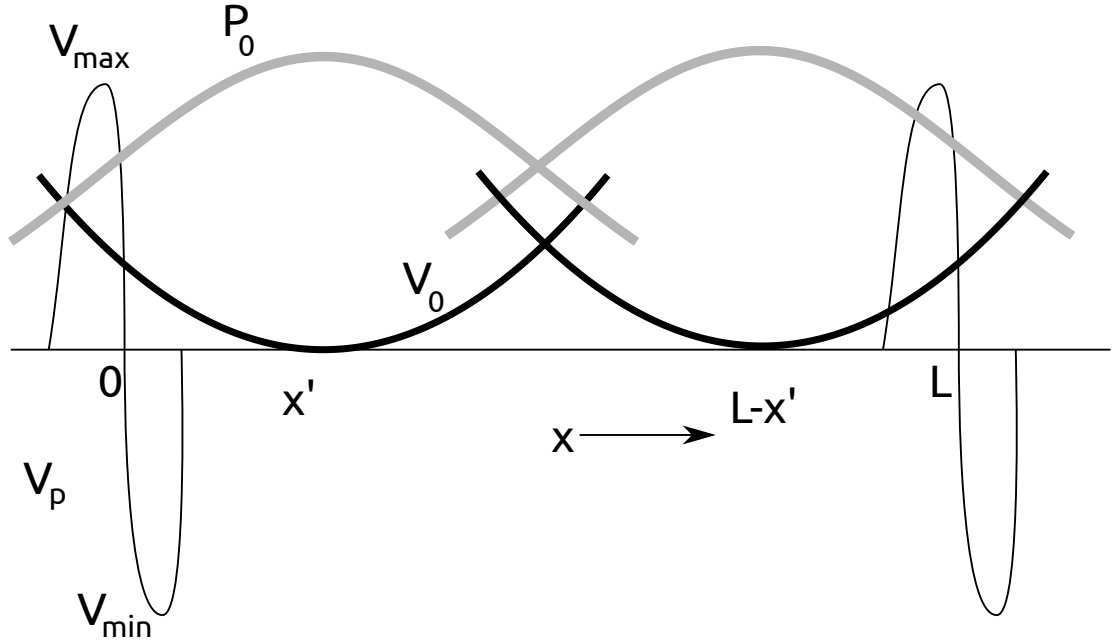


Figure 2.8: Illustration of the kind of potentials employed in the Unbound Equilibration Model. The periodic potential V_p is nonzero only on small regions on the x -axis. It shows a large peak of height V_{max} and large negative dip V_{min} . The spring potential V_0 is parabolic, except that it has a cutoff where it becomes infinite when stretched by more than l_c . The corresponding probability distribution P_0 (grey curve) is assumed to have relaxed to equilibrium. The spring potential is shown at two different position, when it is centered at x' and $L - x'$.

In the following, we present a new analytical method that allows us to systematically solve for the behavior of this kind of nonequilibrium system in the limit of large activation barriers. To understand how equilibration can occur in this model, we can rewrite Eqs. 2.4 in the steady state limit

$$\nabla \cdot (\nabla - \mathbf{f}_i) P_i(\mathbf{r}) - c_i P_i(\mathbf{r}) = -c_{1-i} P_{1-i}(\mathbf{r}), \quad i = 0, 1 \quad (2.24)$$

Although this is time independent, we consider the related time dependent equations for variables $\tilde{P}_i(\mathbf{r}, t)$

$$\partial_t \tilde{P}_i(\mathbf{r}) - \nabla \cdot (\nabla - \mathbf{f}_i) \tilde{P}_i(\mathbf{r}) = 0, \quad i = 0, 1 \quad (2.25)$$

where P_i , $i = 0, 1$, is the Laplace transform of \tilde{P}_i , $P_i(s) = \mathcal{L}\{\tilde{P}_i\}$, where the conjugate variable for $i = 0, 1$ are $s = c_0$ and $s = c_1$, respectively. Taking the Laplace transform of both sides of Eqs. 2.25 yields Eqs. 2.24, with the initial conditions

$$\tilde{P}_i(\mathbf{r}, t = 0) = c_{1-i} P_{1-i}(\mathbf{r}, s = c_{1-i}), \quad i = 0, 1 \quad (2.26)$$

These equations have a direct physical interpretation. The left hand sides in Eqs. 2.25 are those of particles diffusing in potentials, but with conservation of particles. For long enough times, independent of initial conditions, the solution to these equations will go to thermal equilibrium given by the Gibbs distribution. Eq. 2.25, $i = 0$, describes diffusion in a quadratic potential. We require that we are probing this at long enough times t , so that it will have nearly reached this equilibrium state. Call this longest relaxation time τ_0 . The solution to the diffusion equation $\tilde{P}_0(\mathbf{r}, t)$ for either $i = 0, 1$ in Eq. 2.25, can be written as a sum over spatial eigenfunctions, $\phi_n(\mathbf{r})$ that decay at

different rates λ_n , (arranged to be monotonically increasing):

$$\tilde{P}_0(\mathbf{r}, t) = \sum_{n=0}^{\infty} \phi_n(\mathbf{r}) \exp(-\lambda_n t), \quad (2.27)$$

of which the smallest λ , $\lambda_0 = 0$, corresponds to the equilibrium state. The relaxation time is $\tau_0 = 1/\lambda_1$, thus the Laplace transformed variable P_0 can be written

$$P_0(\mathbf{r}, s) = \sum_{n=0}^{\infty} \phi_n(\mathbf{r}) \frac{1}{s + \lambda_n}. \quad (2.28)$$

If the $n = 0$ term is to dominate, we therefore require $s = c_0 \ll 1/\tau_0$. The physical interpretation of this condition is that binding typically occurs only after many relaxation times of the unbound end.

$P_0(\mathbf{r}, s = c_0)$ will be dominated by the first term in Eq. 2.28 and therefore proportional to the eigenfunction $\phi_0(\mathbf{r})$ which is the equilibrium distribution and is $\propto \exp(-V_0)$. An important simplifying point in the above approach is that the precise form of the initial condition Eq. 2.26, $i = 0$, is not important, but because of particle conservation, only the total area under P_1 affects the result.

Now we consider the solution for P_1 . If we consider unbinding times much longer than the relaxation time in the bound state, we also arrive at thermal equilibrium, which was shown by Eq. 2.18 to lead to no work being performed. Instead we will consider situations where there are very long lived metastable states. In Fig. 2.8, the potential seen by a particle in Eq. 2.25, $i = 1$, is $V_1 = V_0 + V_p$. If a particle starts between 0 and L , it will remain trapped in that region for a Kramer's time which (ignoring algebraic pre-factors) depends on x' , but has a minimum value of $\tau_m \propto \exp(V_{max})$. By choosing large enough V_{max} this can be made arbitrarily long.

A particle in such a metastable state will relax to a metastable equilibrium, obeying Eq. 2.27 that will eventually fail for times $t > \tau_m$. In this expansion, the longest relaxation time to this metastable state $\tau_1 = 1/\lambda_1$, will be taken to be much smaller than τ_m . Thus the above argument on the range of c_0 can be used *mutatis mutandis* to restrict the unbinding rate to $1/\tau_m \ll c_1 \ll 1/\tau_1$.

In this regime we can understand the solution to Eqs. 2.25 and 2.26, $i = 1$ by considering the corresponding Green's function $\tilde{G}(\mathbf{r}, t; \mathbf{r}_0)$. We replace the initial condition Eq. 2.26, $i = 1$, by

$$\tilde{G}_1(\mathbf{r}, t = 0; \mathbf{r}_0) = \delta(\mathbf{r} - \mathbf{r}_0). \quad (2.29)$$

We can then obtain \tilde{P}_1 from the Green's function from

$$\tilde{P}_1(\mathbf{r}, t) = \int \tilde{G}_1(\mathbf{r}, t; \mathbf{r}_0) c_0 P_0(\mathbf{r}_0, s = c_0) d^3 \mathbf{r}_0. \quad (2.30)$$

For a wide range of times, and regions of \mathbf{r}' , \tilde{G}_1 will approach the same metastable state. A particle starting at any point within a certain region will end up stuck in the same state and hence approach the same metastable equilibrium. Confining our attention to the one dimension model of Fig. 2.8, for $0 < x_0 < L/2$ the solution will be strongly localized at the minimum $x = 0$. For $L/2 < x_0 < L$ the effects of V_p are negligible and $\tilde{P}_1(x) \propto \exp(-V_0)$. This is because the potential V_0 in Eq. 2.23 is cutoff which does not allow the particle to visit the $x = 0$ region. Hence the effect of V_p is only seen close to $x = L$ where it provides a strong repulsion, but over a negligibly small region of x . For $-L/2 < x_0 < 0$, V_p also does not contribute. For $L < x_0 < 3L/2$

the solution will be strongly localized at the minimum at $x = L$. Because of particle conservation, the area under \tilde{G}_1 is always unity.

A physical interpretation of the above equations in terms of a one dimensional one particle system can now be made using the Laplace transformed variables and the metastable limit considered above is now apparent. In the unbound state, the particle reaches thermal equilibrium relaxing to the Gibbs distribution, $P_0 \propto \exp(-V_0)$. Then the periodic potential V_p is suddenly added in. The position at the time of switching is labeled x_0 . Depending on which interval x_0 is in, x will equilibrate to the corresponding metastable equilibrium with $P_1 \propto \exp(-V_1)$ and is completely confined to that interval. The relative probabilities being in one of the three above regions is obtained by the area under P_0 for that interval.

Now that we know how to determine P_0 and P_1 , we would like to calculate the work W_l given by Eq. 2.13. Because of the symmetric form assumed for f_s , the $f_0 P_0$ term in the integrand gives zero contribution and we are left with

$$W_l = \int_0^L \int_{-\infty}^{\infty} f_0(x - x') P_1(x, x') dx dx' \quad (2.31)$$

and consider first how to calculate the inner integral

$$f_l(x') \equiv \int_{-\infty}^{\infty} f_0(x - x') P_1(x, x') dx \quad (2.32)$$

where x' is the position of the tethered end. Eq. 2.23 gives $f_0(x) = -kx$ for $|x| < L/2$.

Using the prescription we have found for $P_1(x, x')$, which is simplified by the above physical interpretation, we can partition this integral into the different x -intervals of metastability: $I_- \equiv [-L/2, 0]$, $I_0 \equiv [0, L]$, and $I_+ \equiv [L, 3L/2]$. The value of $P_1(x, x')$

depends on the probability of initially being trapped in one of those three intervals. Because of the cutoff we have imposed on V_0 , only two intervals need be considered for a given value of x' . For $0 < x' < L/2$, only intervals I_- and I_0 occur. The probability that $x \in I_-$ given x' is

$$E(x') \equiv P(x \in I_-|x') = \int_{-\infty}^0 p_0(x - x')dx = \int_{x'}^{\infty} p_0(x)dx \quad (2.33)$$

and the probability that $x \in I_0$ is $P(x \in I_0|x') = 1 - E(x')$. Here $p_0(x)$ is proportional to $P_0(x)$ but normalized to unity, to simplify the presentation. We can obtain the values for $L/2 < x' < L$ by symmetry, so that $P(x \in I_+|x') = E(L - x')$ and $P(x \in I_0|x') = 1 - E(L - x')$. In the limit considered here, the effects of the cutoff in the potential will have a negligible effect. For this reason, $p_0(x)$ will be a normal distribution and thus $E(x')$ is simply related to the complementary error function, $E(x') = \frac{1}{2}erfc(\sqrt{k}x')$.

At this point, it is possible to evaluate Eq. 2.31 directly. However, for simplicity, we take a more intuitive approach: there is a symmetry in many of the quantities considered, as shown in Fig. 2.8 where the potential V_0 and corresponding probability distribution p_0 is for the tethering point at x' and at $L - x'$. Therefore it is convenient to consider the quantity $f_{l/2}(x') \equiv f_l(x') + f_l(L - x')$.

Additionally, by equation 2.32, f_l can be thought of as an expectation value, or weighted average. Any expectation value can be expressed as a weighted sum of expectation values broken down by region. This yields

$$W_l = \frac{kc_0}{c_0 + c_1} \int_0^{L/2} 2E(x')(\langle x \rangle' - x') + x' dx'. \quad (2.34)$$

In the limit of large L , which we are considering by virtue of the condition

on the cutoff in V_0 imposed by Eq. 2.23, the integrand simplifies because $\langle x \rangle'$ becomes exponentially close to x' , and the only term remaining is x' . Thus for large L , $W_l = (c_0/(c_0 + c_1))kL^2/8$. The factors involving the c 's represent the fraction of time spent in the bound configuration. The last term increases quadratically with L . This result is misleading if not taken with the appropriate limits that have been assumed in its derivation. The factor $(c_0/(c_0 + c_1))$ is very close to unity as we are assuming that the relaxation time in the unbound state is much faster than in the bound state, hence $c_0 \gg c_1$. However the work W_L to move a distance L was assumed to be in the adiabatic limit, and here the time scales associated with bound state relaxation are exponentially long. This is because to reach this metastable equilibrium the particle has to hop over barriers of size $V_0(x')$, see Fig. 2.8. Hence the longest relaxation time for this is at $x' = L/2$ and is of order $\exp(kL^2/4)$. Note that this does not contradict our assumption that we are still in a region of metastability, which requires times much less than $\exp(V_{max})$. But for this to work, we require that $V_{max} \gg V_0(L/2)$.

Now we consider the case where the spring length cutoff $l_c \rightarrow \infty$. The disadvantage of this is that the chain end can, in principle, hop over many barriers ending up arbitrarily far from the tether point, and that these hopping times should be included in the above analysis. However, the probability of such a hop becomes negligible when the probability of finding the chain end there is small. Hence we still have a clear separation of time scales between metastable states as discussed above, and fully equilibrated system, which requires surmounting the energy barrier V_{max} . In this case, we can therefore assume that when the chain end x' is between nL and $(n+1)L$, it will strongly localized

at $x' = nL$. Therefore

$$f_l(x') = -k \sum_{n=-\infty}^{\infty} \Delta_n(x')(nL - x') \quad (2.35)$$

where $\Delta_n(x')$ is the probability of initially finding the chain end between nL and $(n+1)L$,

$$\Delta_n(x') = E(nL - x') - E((n+1)L - x'). \quad (2.36)$$

It is easily seen that $\Delta_{-n}(L - x') = \Delta_n(x')$. Using this and Eq. 2.35

$$f_l(L - x') = -f_l(x') + kL \sum_{n=-\infty}^{\infty} \Delta_n(x') = -f_l(x') + kL. \quad (2.37)$$

To obtain the work, we follow the same procedure as above and consider $f_l(x') + f_l(L - x')$, which here is just kL . Therefore in this case,

$$W_l = \frac{c_0}{c_0 + c_1} \frac{kL^2}{2}. \quad (2.38)$$

This is an exact value for this model, for all k and L , given that we are in a region of strong metastability.

2.7.1 Efficiency in large power stroke limit

We now are in a position to answer a central question about the performance of this kind of device: is the efficiency limited by the small value of $k_B T$ compared to photon energies? We have seen from the above analysis that it is possible to get arbitrarily large forces developing at the expense of exponentially slow operation. However this is in the limit of infinitesimal plate velocity v . In contrast, the power obtained is instead average force times this, $\langle f \rangle v$ and we would like to operate the device at the

velocity of maximum power, which necessitates the operation of it far from equilibrium, because compensating the increase in v is a decrease in $\langle f \rangle$ due to dissipation. It could be that the optimum velocity of operation decreases very quickly with $kL^2/2$ meaning that the device becomes increasingly inefficient as the spring constant k is increased. This would make it impossible to harvest more than of order $k_B T$ energy per cycle.

The efficiency is defined as the ratio of the amount of power produced to the amount of power put in. The amount of energy needed to dissociate a polymer end from a binding site is V_{min} . Binding to V_{min} must produce an energy less than that of an unbound polymer. The power put in is $V_{min}c$ where $1/c = 1/c_0 + 1/c_1$. Therefore the efficiency is

$$\eta = \frac{\langle f \rangle v}{c V_{min}}. \quad (2.39)$$

To investigate this problem further, the one dimensional model of the last section with $l_c \rightarrow \infty$ was implemented using Metropolis Monte Carlo. We chose the periodic potential V_p to vary as

$$V_p(x) = \begin{cases} -4V_{min} \frac{x}{\delta} (1 - \frac{x}{\delta}), & \text{if } 0 < x < \delta. \\ -4V_{max} \frac{x}{\delta} (1 + \frac{x}{\delta}), & \text{if } 0 > x > -\delta. \\ 0, & \text{otherwise.} \end{cases} \quad (2.40)$$

Here we set $\delta = 0.1$, $V_{max} = V_{min} = 100$, and $L = 1$. In order to preserve diffusional dynamics, steps in x were attempted uniformly in the range $[-0.025, 0.025]$ ensuring that the periodic potential cannot be jumped across in one move. One move increased the time by .05, though this number was arbitrary and aside from an obvious rescaling,

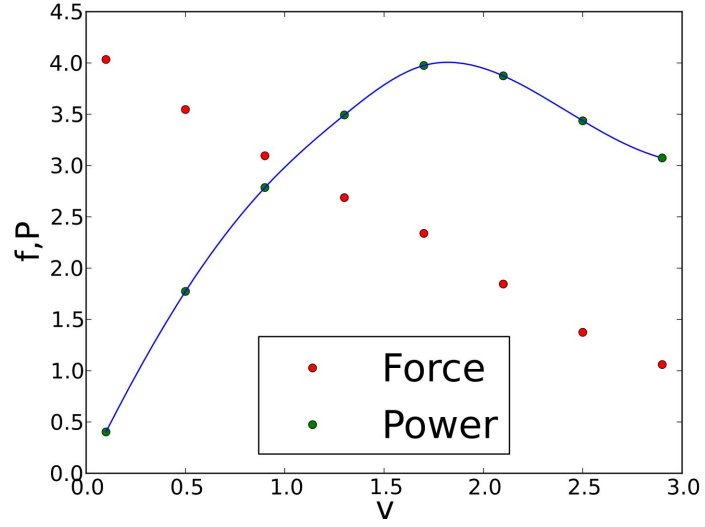
does not affect the results obtained.

To observe behavior in the limit of metastability as discussed in the previous section, the rate of unbinding must be set to be small compared to the inverse metastable equilibration time in the bound state. Hence we chose the unbinding rate $c_1 = 10^{-5}$ and $c_0 = 5 \times 10^{-4}$.

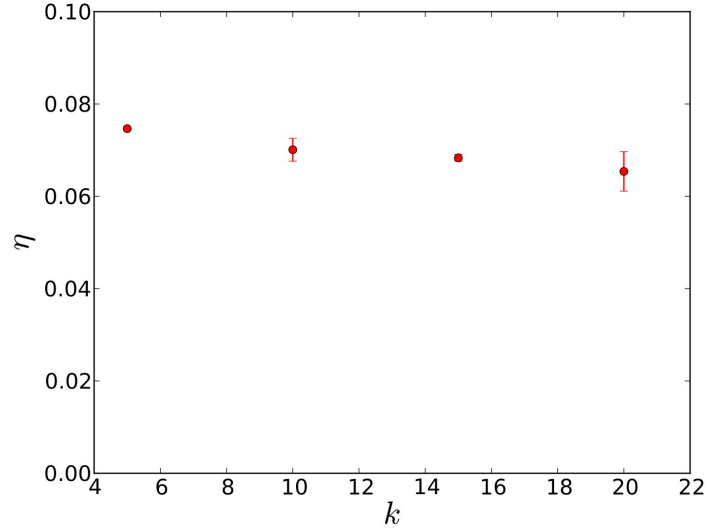
As the simulation was running, the tether point was moved at velocity v which was typically small, The average spring force $\langle f \rangle$ was measured as a function of v for a given spring constant k . The results of a run of 3×10^{10} steps are shown in Fig. 2.9(a).

We are interested in the limit of large k , although this is hard to achieve numerically owing to exponentially long relaxation times. The parameters used allow us to probe up to $k = 20$. In the large k limit, the minimum value of V_{min} needed to bind is $kl^2/2$, where l is the maximum amount the spring will need to stretch from the tether to the binding site. Because $\delta = 0.1$ and $L = 1$, this implies $l = 0.9$. Therefore our formula for the efficiency, given this input energy is $\eta = P_{max}/(ckl^2/2)$, where P_{max} is the maximum of the power versus velocity, as shown in Fig. 2.9(a). Plotting the efficiency for different values of k ranging from 5 to 20 yields the points in Fig. 2.9(b). Despite the fact that the relaxation time for metastable relaxation of the system varies over more than two orders of magnitude, the overall efficiency is almost constant. We expect at higher value of k , the efficiency will eventually drop owing to the fact that the average unbinding time becoming smaller than the metastable relaxation time.

What the above analysis shows is that in the limit where the photon cross section can be made arbitrarily low, the efficiency can be adjusted to be constant,



(a)



(b)

Figure 2.9: (a) The force and power versus velocity for the one dimensional model described in the text. Here the spring coefficient $k = 15$. The line going through the power is a cubic spline fit used to more accurately determine the maximum value of the power. The velocity and power are both in units of 10^{-6} . (b) A plot of the efficiency of the motor as a function of the spring constant k . Four separate runs, each of 3×10^{10} steps were used to determine the error bars, for each data point shown.

independent of the photon energy. This is accomplished by choosing a large spring coefficient. In reality with photon energy of $2eV$ and $k_B T \approx 1/40eV$, photon flux would have to be far too low for this optimal regime to be realizable. However the above analysis also shows that the efficiency can be substantially increased by choosing larger k at the expense of lowering the cross section. The energy delivered in one cycle should scale as $E_c = kL^2$. This can be increased to be substantially larger than thermal energies but at the expense of a long relaxation time proportional to $\exp(E_c/k_B T)$. As noted earlier, it should be possible to make E_c about $7k_B T$, with reasonable parameter estimates.

2.8 Conclusions

Here we have analyzed the viability of converting photons to mechanical energy using a device composed of an canted polymer brush tethered to a lower plate but able to bind its other ends to sites on an upper plate. Photons can dissociate these ends from binding sites. By a combination of analytical and numerical arguments we showed that in steady state, this produces net mechanical power.

The system is inspired by biological motors such as myosin II that bind to actin and dissociate via the binding of ATP. The analysis used here could also be applied to such systems, however in reality they contain many more stages. In general, these kind of systems are classified as “thermal ratchets” [37], where the system can be thought of as moving in a washboard potential in the presence of thermal noise. Though

that description can be very useful in understanding the general principles behind the operation of such motors, in the present case we are trying to model the system in more detail than such models can afford. Instead we have described the system using Langevin dynamics and also two coupled Fokker-Planck equations similar in spirit but not identical to previous approaches [30, 29]. The difference here is that in order for potentials to be a sensible model for a polymer tethered to a single point, they cannot be periodic. Such modelling allows us to see how varying microscopic parameters affect the power and force characteristics.

The analytical results on the Unbound Equilibration Model and extensive one dimensional simulations, show that the force applied by the device can be made arbitrarily large at the expense of having exponentially long relaxation times. At a given photon flux, the production of large forces from single polymers imply the need for a very low cross section of interaction between the photon and the bound end plus binding site, as long relaxation times are required. Therefore there is a trade off between this force and the speed the device can move. This may be circumvented to some extent by stacking transparent devices of this kind, so that even though the cross-section of interaction of an individual photon with a given layer is low, it will eventually be captured by one layer.

Therefore it appears that there is no theoretical obstacle to prevent the photomechanical conversion of energy in this manner, however it represents a significant experimental challenge. That being said, we have shown through simulations that the photomechanical effect of this device persists even when binding sites are placed ran-

domly on the upper plate, which suggests that the precision required for production may indeed be afforded some flexibility.

It has been pointed out [40] that there is an important distinction between artificial molecular switches and artificial molecular machines, the former being a fraction of a penny, and the latter being extremely challenging to create. The approach investigated here is closer to biological motors than other proposals, and should be more forgiving about randomness, either in fabrication or due to thermal motion, than approaches that require precise chemical synthesis of molecules capable of sophisticated conformational changes [21]. However, its experimental realization is still quite clearly a formidable task.

Chapter 3

Emergence of Metachronal Waves in Active Microtubule Arrays

3.1 Introduction

Metachronal waves refer to the synchronization of thin, flexible appendages that result in large-scale wavelike formations. These appear in biological systems at the macroscopic scale (e.g. the motion of millipede legs) and at the microscopic scale (e.g. cilia in air pathways). On the microscopic level, metachronal waves are essential components of several critical biological processes, from motility in microorganisms to mucus clearance in human bronchial tubes [41, 42]. If cilia are unable to effectively move and synchronize, the results are often severe – especially if the disorder is genetic [41]. Research into physical explanations for cilia beating [43], and of spontaneous metachronal behavior in cilia is ongoing and still not well understood [44, 45], although many have

suggested that this phenomenon can be explained from hydrodynamic coupling between cilia [46, 47, 48, 49].

Recently, in some remarkable experiments, Sanchez et al. demonstrated metachronal wave behavior in an *in vitro* system [1, 5]. Microtubules (MTs) aggregated into bundles of length $10 - 100\mu\text{m}$ due to the addition of polyethylene glycol [50]. Many of these bundles attached at one end to a fixed boundary forming dense arrays. When exposed to a solution containing clusters of kinesin and ATP, sustained metachronal wave behavior between MT bundles (similar to that displayed by cilia and flagella) was observed. MT bundles were constrained to move between two glass slides. It is surprising that a system with such few ingredients could develop complex behavior that so closely resembles biological systems, which are made up from a much more complicated machinery. Proteomic analysis indicate that eukaryotic cilia are composed of many hundreds of proteins [51].

Some important details of this *in vitro* system are still unclear, most notably whether the MTs in this experiment are unipolar or of mixed polarity. Opposite polarity MTs will move past each other, causing separation into unipolar bundles [52, 53]. We present arguments and simulations for unipolarity in 3.5. The surprising mechanism for the motion of unipolar bundles mentioned here has not previously been given [1, 5], and we believe that the agreement between our model and experiments provides further evidence to support our proposed explanation.

In this chapter, we first outline a mechanism by which the metachronal wave formation observed by Sanchez et al. can be understood. The mechanism described

here is in most ways identical to the model used to describe and simulate cytoplasmic streaming in *Drosophila* oocytes, and the fact that it can be adapted as such is in many ways a testament to its predictive power. A fair amount of attention has been paid in recent years to the understanding of how metachronal waves form in such arrays [54, 55, 56, 57]. However, such models often rely on assumptions about individual MT (or cilia) beat patterns and/or on phenomenology. The model we propose makes no such assumptions (beyond some minor simplifications), relying on first-principles fluid mechanics calculations. This is important, as it is not clear why one would want to impose oscillatory behavior on individual MTs given the lack of a well defined internal structure.

3.2 Proposed Mechanism of Action

We now present a model for the simulation of the Sanchez et al. system. A similar method has been used successfully to simulate cytoplasmic streaming in *Drosophila* oocytes[14], and is based on theoretical work completed several decades ago regarding the calculation of Stokes flows created by a point force (stokeslet) near no-slip boundaries[12, 15]. A conceptual explanation of this mechanism is given below, and further details regarding theory and implementation are given in 3.3 and 3.4.

An illustration of how MT bundles are simulated is given in Figure 3.1. Each MT bundle is modeled as a chain of monomers (i.e. polymer) which are held an approximately fixed distance from one another by a spring force. The base of each polymer is

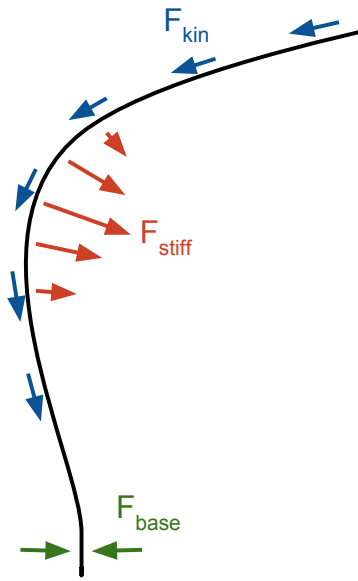


Figure 3.1: Conceptual illustration of forces acting on a single polymer that are not due to hydrodynamic interactions. The blue vectors indicate the buckling forces due to kinesin walkers (tangent to polymer), the red vectors show the direction and relative magnitude of stiffness forces (in the direction of $d^4\mathbf{r}/ds^4$), and the green arrows indicate a restorative force keeping the base of the polymer approximately perpendicular to the binding surface.

anchored to a single point, and the polymer at the base is kept roughly perpendicular to the anchoring surface. Let the polymer be described by the curve $\mathbf{r}(s)$, where $\mathbf{r}(0)$ is the location of the polymer base, and s is the arc length. We give the polymer a stiffness by implementing an energetic cost of bending proportional to curvature squared, which implies a local force at s proportional to $d^4\mathbf{r}/ds^4$. Additionally, monomers feel a “buckling” force due to the drag from the walking kinesin $F_{kin} = -f_k d\mathbf{r}/ds$, which is parallel to the polymer and toward the polymer base. f_k will depend linearly on the speed of the kinesin and the solvent viscosity. This force continually adds energy to the system (making it active), and has been shown to be a good representation of the average drag force due to kinesin walking along the microtubule away from the polymer base [14].

This kind of model for a single chain was first employed to understand glide assay dynamics in two dimensions [58]. In three dimensions, periodic waves develop whose dynamics have been analyzed in detail [14], and related theoretical work has recently also been performed [59]. However, scaling can be used to get the relevant length and timescales [58]. The average radius of curvature depends on the strength of the buckling force f_k , and the elastic constant of a filament characterizing its stiffness k_{stiff} . The radius of curvature over quite a wide range of parameters can be shown to be $R = (k_{stiff}/(\beta f_k))^{1/3}$, where $\beta \approx 0.05$. Likewise, the angular frequency is $\omega = f_k/(\nu R)$, where ν is the hydrodynamic drag coefficient per unit length. Although there is a fairly large experimental uncertainty in parameters used to model a *Drosophila* oocyte, this model finds quite good agreement with the experimental time and length scales. R was

predicted to be $25 - 54\mu\text{m}$, close to the $16.3 \pm 2.2\mu\text{m}$ observed. Likewise, the time scale was predicted to be $203 - 1094\text{s}$, which is in the observed range of $370 \pm 42\text{s}$. It is interesting that the length and time scales observed by Sanchez et al. are also quite close to these numbers, and that the frequency of biological cilia beating is often three orders of magnitude higher than this.

Polymers also feel hydrodynamic forces. As the force from the kinesin causes the polymers to buckle, we begin to see complex motion. Each monomer acts as a point force (stokeslet) in the surrounding fluid. This force a monomer exerts on the fluid is simply the sum of all of the other forces on the monomer: because the Reynolds number is nearly zero, there are no inertial terms, meaning the force is transferred perfectly from the monomer to the fluid. As this is a Stokes flow, the flow contributions from all stokeslets add linearly, and we can (in principle) calculate the flow everywhere. However, we do not need to calculate the fluid velocity everywhere – only at points with monomers. Therefore, the evolution can be calculated via a pairwise sum over all monomers (see 3.3).

We also assume all polymer motion is two dimensional with a constant value of z , which is physically sensible when considering the geometry of the Sanchez et al. experiments. In this experiment, MT bundles were observed between glass slides, with a height H , of approximately $10\mu\text{m}$, creating a narrow channel for which fluid can flow. For this reason, we adopt a two dimensional geometry. In addition, the no-slip boundaries of the plates have a large impact on the hydrodynamic forces between monomers[12, 15], which we state explicitly in 3.3. Other close-range contact forces

were also used (repulsion from anchoring surface, monomer-monomer repulsion), and these are explained in 3.4.

We can now address at the qualitative level the mechanism by which we propose the metachronal waves observed by Sanchez et al. form. As kinesin walk away from the polymer bases, the polymers will tend to buckle. If a polymer is isolated, this buckling will lead to unstable motion (corkscrew motion or irregular beating)[14]. When placed in an array, however, nearby polymers will exert hydrodynamic forces on one another that tend to synchronize their motion. If these hydrodynamic forces are sufficiently strong, this can cause a transition from disordered motion to aligned MTs and correlated motion.

Despite the fact that this model was developed to explain and simulate cytoplasmic streaming, its mechanism can be easily adapted for related biological phenomena. Indeed, when the conditions of the Sanchez et al. experiment are simulated in the same way, we observe metachronal waves. It is not clear if this is formally a transition or a more continuous crossover effect, but the results found make strong predictions that should be testable experimentally. In the following, we present the results of these simulations and discuss the required conditions for metachronal wave formation.

3.3 The Quasi-2D Interaction Tensor

The interaction tensor used in simulations is that of a stokeslet enclosed by two infinite parallel plates, as derived by Liron and Mochon[15]. In general, the interaction

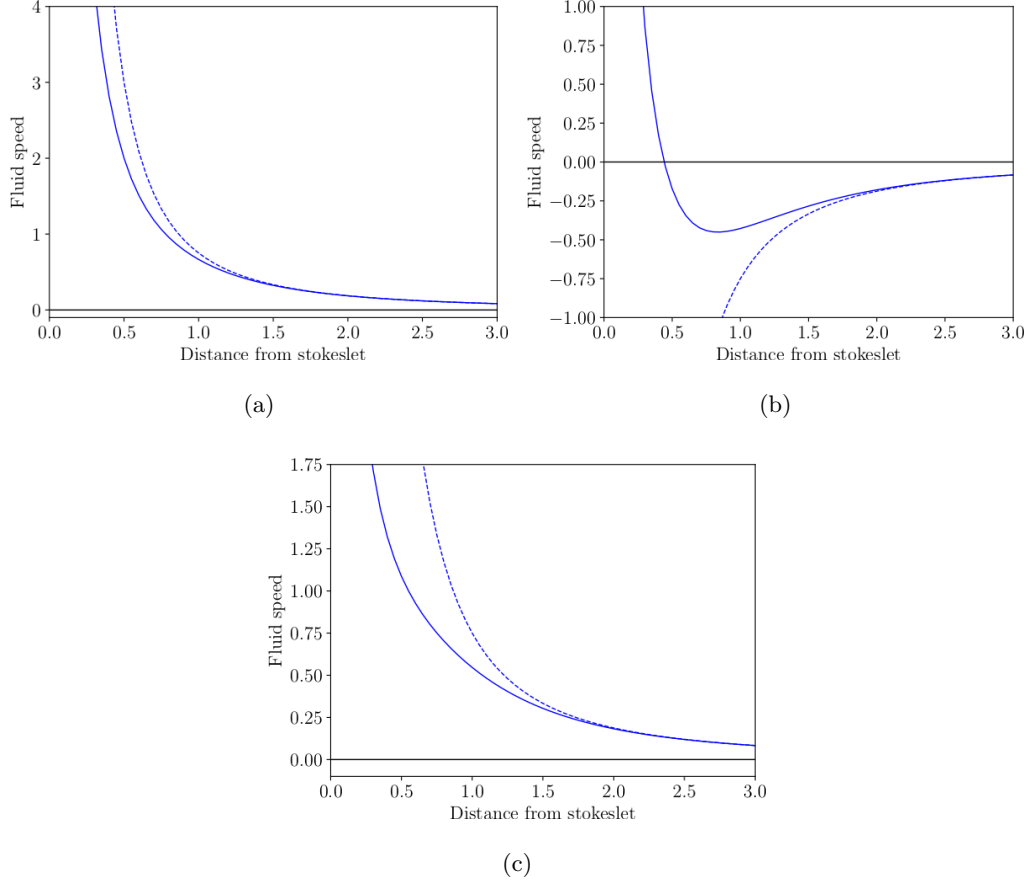


Figure 3.2: Fluid speeds as a function of distance ρ from the stokeslet $\mathbf{F} = \hat{i}$. Solid curves are calculated using the full interaction tensor (3.2) and dashed lines are the far-field approximation (3.3). (a) $u_x(\rho)$ along the line $y = 0$; (b) $u_x(\rho)$ along the line $x = 0$; (c) $u_y(\rho)$ along the line $y = x$.

tensor \mathbb{G} is defined as the relationship between the fluid flow $\mathbf{u}(\mathbf{r})$ and the stokeslet \mathbf{F} which causes this flow:

$$\mathbf{u}(\mathbf{r}) = \mathbf{F} \cdot \mathbb{G}(\mathbf{r}) \quad (3.1)$$

For computational efficiency, we assume all monomers to be only in the xy -plane, with parallel plates at $z = \pm H/2$. This reduces a three-dimensional problem to two dimensions, as (a) the stokeslet is located in the xy -plane, (b) the stokeslet's direction has no z -component, and (c) we only concern ourselves with flows in the xy -plane (see Figure 3.3). For this arrangement, it can be shown from Liron and Mochon's general result that the interaction tensor at a displacement \mathbf{r} (and $\rho \equiv |\mathbf{r}|$) from a single stokeslet \mathbf{F} at the origin reduces to

$$\mathbb{G}(\mathbf{r}) = \frac{H}{8\pi\mu\rho^2} \left\{ \left[4 \left(\frac{\rho}{H} \right)^2 S_1 - \frac{1}{2} \frac{\rho}{H} I_1 \right] \mathbb{I} + \left[4\pi \left(\frac{\rho}{H} \right)^3 S_2 + \frac{1}{2} \frac{\rho}{H} I_1 - \frac{1}{4} \left(\frac{\rho}{H} \right)^2 I_2 \right] \frac{\mathbf{r} \otimes \mathbf{r}}{\rho^2} \right\} \quad (3.2)$$

where

$$\begin{aligned} S_1 &\equiv \frac{1}{4} \sum_{n=0}^{\infty} \frac{(-1)^n}{\left[\left(\frac{\rho}{H} \right)^2 + n^2 \right]^{1/2}} \\ S_2 &\equiv \frac{1}{4\pi} \frac{\rho}{H} \sum_{n=0}^{\infty} \frac{(-1)^n}{\left[\left(\frac{\rho}{H} \right)^2 + n^2 \right]^{3/2}} \\ I_1 &\equiv \int_0^{\infty} \xi J_1 \left(\frac{\rho}{H} \xi \right) \frac{\tanh^2 \frac{\xi}{2}}{\sinh \xi - \xi} d\xi \\ I_2 &\equiv \int_0^{\infty} \xi^2 \left[J_0 \left(\frac{\rho}{H} \xi \right) - J_2 \left(\frac{\rho}{H} \xi \right) \right] \frac{\tanh^2 \frac{\xi}{2}}{\sinh \xi - \xi} d\xi \end{aligned}$$

Here, J_n is the Bessel function of the first kind. Because S_1 and S_2 do not converge rapidly as defined above, we also make use of the Poisson sums

$$S_1 = \sum_{k=0}^{\infty} K_0 \left[\pi(2k+1) \frac{\rho}{H} \right]$$

$$S_2 = \sum_{k=0}^{\infty} (2k+1) K_1 \left[\pi(2k+1) \frac{\rho}{H} \right]$$

where K_n is the modified Bessel function of the second kind.

In the far field, it can be shown that (3.2) approaches

$$\mathbb{G}(\mathbf{r}) \approx -\frac{3H}{32\pi\mu\rho^2} \left(\mathbb{I} - 2 \frac{\mathbf{r} \otimes \mathbf{r}}{\rho^2} \right) \quad (3.3)$$

Figure 3.2 shows plots of $\mathbf{u}(\mathbf{r})$ at selected locations, and compares the exact value from (3.2) to the far-field approximation from (3.3).

We can now make some conceptual observations regarding this interaction tensor and how it compares to the boundary-free Oseen tensor \mathbb{G}_0 :

$$\mathbb{G}_0(\mathbf{r}) = \frac{1}{8\pi\mu r} \left(\mathbb{I} + \frac{\mathbf{r} \otimes \mathbf{r}}{r^2} \right)$$

First, we immediately notice a $1/r$ dependence (rather than $1/\rho^2$). This means forces without boundaries tend to be more long-range, and boundaries result in long-range screening. Second, \mathbb{G}_0 is always positive, whereas this is not true for the interaction tensor used here. One key implication of this is that flows created by a stokeslet are often flowing opposite its direction (e.g. Figure 3.2b). Both of these qualities may enhance metachronal behavior in the confined system. Screening means that interactions between nearby polymers are most important, creating a “domino effect” from one

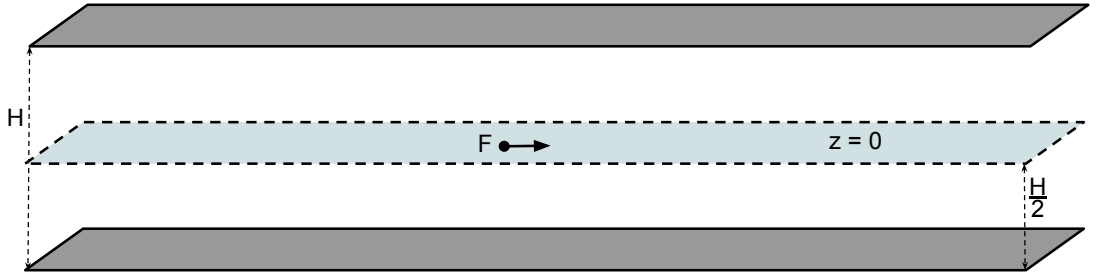


Figure 3.3: Illustration of the geometry for which interaction tensor is derived in 3.3. While this is a three-dimensional system, we constrain polymers to the xy -plane.

polymer to the next rather than having motion more influenced by long-range interactions. The creation of opposing flows means (among other things) that if one polymer is moving toward the anchoring surface, it may exert a force on many of its neighboring polymers *away* from the anchoring surface. This encourages wavelike behavior rather than uniformity of beating motion.

3.4 Simulation Methods

The algorithm we implement is built on work that was used to simulate the mechanism behind cytoplasmic streaming in *Drosophila* oocytes [14], and many of the methods and equations below are explained in detail in these papers. This software simulates an array of active microtubules tethered to a plane that works as follows and is explained in further detail below.

1. After an array of polymers is initialized, forces on all monomers are summed (described below, also see Figure 3.1) and monomer position and velocity are

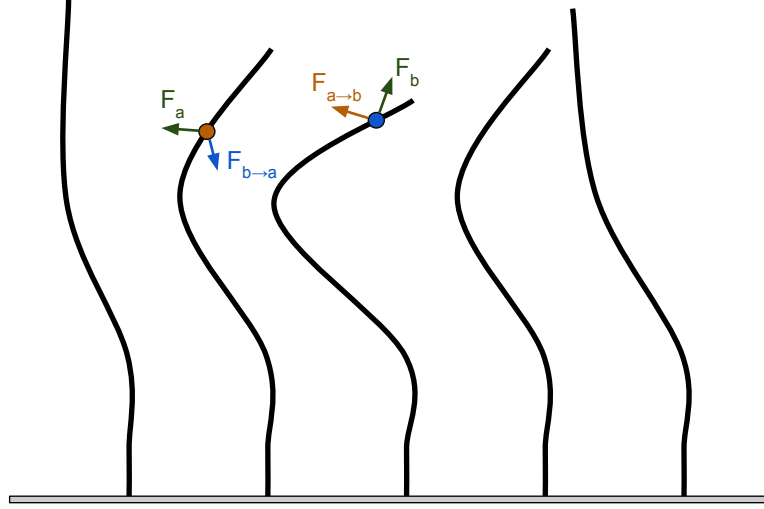


Figure 3.4: Illustration of hydrodynamic forces between two example monomers in a planar polymer array. The green forces are the sum of non-hydrodynamic forces on the monomer (and by extension the force the monomer exerts on the surrounding fluid). $\vec{F}_{a \rightarrow b}$ and $\vec{F}_{b \rightarrow a}$ are the hydrodynamic forces on monomer b due to \vec{F}_a and the hydrodynamic force on monomer a due to \vec{F}_b , respectively.

updated using time step dt .

2. This motion initiates complex flow in the surrounding fluid. The fluid flow is not simulated directly, but the resulting hydrodynamic forces from this flow are calculated via an Oseen tensor with corrections by Blake[12]. This is illustrated in Fig. 3.4.
3. Forces on each monomer are summed, and monomer position and velocity are updated accordingly.
4. Once updated, steps 2-3 are repeated.

In the present work there were these differences:

1. N Microtubules are confined to the xy -plane, with polymer bases separated by a distance l tethered either to a flat plate at $y = 0$ or to a circular boundary. For all presented results, $N = 128$. The geometry of this is shown in Fig. 3.3.
2. At the tethering point, a potential was added in order to keep the base monomer approximately orthogonal to the boundary.
3. Rather than the Blake correction to the Oseen tensor, we use the simplified Liron/Mochon interaction tensor described in Section 3.3.

Now we describe how the above was accomplished in more detail. Each polymer is composed of $n = 16$ monomers. The i th monomer position \mathbf{r}_i is updated using a fourth order Runge Kutta integration of the equation

$$\frac{d\mathbf{r}_i}{dt} = \mathbf{u}(\mathbf{r}_i) - k_{kin} (\mathbf{r}_{i-1} - \mathbf{r}_{i+1}) \quad (3.4)$$

where dt is the time step (set to 0.003), k_{kin} (set to 0.2) controls the strength of the kinesin force tangent to the polymer (\mathbf{F}_{kin} in Figure 3.1), and $\mathbf{u}(\mathbf{r}_i)$ is the fluid velocity due to the motion of all other monomers as given by Equation 4.16 and 3.2 (which imparts the forces $\mathbf{F}_{a \rightarrow b}$ in Figure 3.4):

$$\mathbf{u}(\mathbf{r}_i) = \sum_{j \neq i} \mathbf{F}_j \cdot \mathbb{G}(\mathbf{r}_i - \mathbf{r}_j) \quad (3.5)$$

Here, \mathbf{F}_j is the total force on the fluid due to the j th monomer. Because there are no inertial effects when $Re \ll 1$, any non-hydrodynamic force exerted on the monomer must be transferred to the fluid. In our case,

$$\mathbf{F}_j = \mathbf{T}_j + \mathbf{C}_j + \mathbf{Q}_j, \quad (3.6)$$

where

- $\mathbf{T}_j = k_{spr} [(|\mathbf{r}_{j-}| - \ell) \hat{\mathbf{r}}_{j-} + (|\mathbf{r}_{j+}| - \ell) \hat{\mathbf{r}}_{j+}]$

with $\mathbf{r}_{j\pm} \equiv \mathbf{r}_{j\pm 1} - \mathbf{r}_j$, is the spring force keeping monomer separation approximately constant. For our simulations, $k_{spr} = 100$ and $\ell = 1$. In these simulations the separation between polymer bases defines above, l is equal to 4ℓ .

- $\mathbf{C}_j = k_{stiff} (2\mathbf{r}_i - \mathbf{r}_{i+2} - \mathbf{r}_{i-2})$

is the stiffness force which resists polymer bending. k_{stiff} is varied in our simulations, but typically $5 \leq k_{stiff} \leq 20$.

- $\mathbf{Q}_j = \mathbf{P}_j + \mathbf{B}_j + \mathbf{W}_j + \sum_k \mathbf{H}_{jk}$

is the sum of miscellaneous conditional forces:

$$- \mathbf{P}_j = k_{pin} (\mathbf{r}_j - h\hat{\mathbf{j}})$$

$$\text{if } (j \bmod n) = 1$$

is the force on the base monomer of each polymer chain keeping it pinned to the anchoring surface. For our simulations, we set $k_{pin} = 100$ and $h = 1$.

$$- \mathbf{B}_j = k_{pin2} (\mathbf{r}_j - \mathbf{r}_{j-1} - \ell\hat{\mathbf{j}})$$

$$\text{if } (j \bmod n) = 2$$

is the force on the second monomer in each polymer chain, keeping the base of each polymer approximately orthogonal to the anchoring surface (F_{base} in Figure 3.1). For our simulations, we set $k_{base} = 100$.

$$- \mathbf{W}_j = k_{wall} \left[1 - \left(\frac{d_{wall}}{y_j} \right)^4 \right] \hat{\mathbf{j}}$$

$$\text{if } y_j < d_{wall}$$

is the repulsive force exerted by the anchoring plane on any monomer that gets close to the wall. For our simulations, we set $d_{wall} = 0.5$ and $k_{wall} = 100$.

$$- \mathbf{H}_{jk} = k_{rep} \left[1 - \left(\frac{d_{rep}}{|\mathbf{r}_j - \mathbf{r}_k|} \right)^4 \right] (\mathbf{r}_j - \mathbf{r}_k)$$

$$\text{if } |\mathbf{r}_j - \mathbf{r}_k| < d_{rep}$$

is the repulsive force between monomers that are very close to one another.

For our simulations, we set $d_{rep} = 0.5$ and $k_{rep} = 1$.

3.5 Analysis of Unipolarity

The work of Sanchez et al. [1, 5] consists of a mixture of biotin-labeled kinesin-1 motors bound together to form clusters using multimeric streptavidin and taxol stabi-

lized microtubules in a polyethylene-glycol solution with ATP. These form bundles of microtubules, some of which are adsorbed to air-water or air-glass interfaces, that point out from the interface forming a lawn of microtubule bundles. These bundles are flexible and show bending similar to what is seen in the simulations described here in both the time scales, length scales, and correlations between different bundles.

The question that is not answered in the experimental work is the directionality of the microtubules inside a bundle. The microtubules forced into bundles by the polyethylene glycol (PEG) could be of mixed polarity so that some have their minus ends at the interface while others have their plus ends there. We will refer to microtubules with different orientations as having different “polarities”, minus-ends against the interface as “minus” and those with opposite polarity as “plus”.

The problems with having a mixed polarity bundle are two fold. The first is that for a wide range of experimental parameters, we expect mixed polarity bundles to be unstable [52, 53]. The second problem is that it is not clear that mixed polarity bundles can give rise to the motion seen experimentally. We will analyze both problems below.

3.5.1 Instability of mixed polarity bundles

The first problem is that adjacent microtubules with different polarities will be linked by kinesin clusters that will apply equal and opposite forces to them. This will cause the minus microtubules to be pushed toward the interface, and the plus ones away from it. The forces from the kinesin act in parallel on a microtubule over its

length which is of order $10\mu m$. The forces that these cause can be competitive with depletion forces caused by the PEG as we will now see. A full analysis of this is not possible without more information about the details of the system such as the density of kinesin clusters and chain lengths of the PEG. However we can do a calculation to show that even with very modest assumptions concerning kinesin density, expulsion of plus microtubules will take place.

Depletion forces exert an osmotic pressure on microtubules and filaments. Each polymer excludes a roughly spherical region of order its radius of gyration R_g . Entropic forces favor the separation of microtubules into bundles because less volume is excluded by the PEG. We will estimate the force acting on a single microtubule protruding from a bundle. PEG is depleted in a region of size R_g around the microtubule. The increase in free energy per unit area caused by this depletion is of order pR_g where the osmotic pressure is $p = k_B T \rho$, and ρ is the number of polymers per unit volume. The increase in free energy dF , in raising the microtubule by a height dz , is $dF = (2\pi R_m dz) p x$. Here R_m is the microtubule radius. If we assume that the polymers are close-packed around the microtubule to get the maximum effect, then $\rho = 1/(4\pi R_g^3/3)$. So the force needed to push the microtubule out of the tip of the bundle is $f = dF/dz = (3/2)R_m k_B T / R_g^2$.

$R_m \approx 13nm$ and conservatively taking $R_g = 1nm$, which is quite small for PEG, $f = 81pN$ The stall force of kinesin is approximately $5pN$ [60]. So only 16.2 kinesins are needed to overcome the depletion forces and expel this microtubule from the bundle.

The minimum separation of kinesin on a microtubule is $8nm$ and there are 13

tracks around its circumference. Because kinesin has a strong affinity for microtubules we expect a high density of bound kinesin. Therefore 16 kinesins contributing to the force over a distance of $10\mu m$ is over three orders of magnitude less dense than the maximum density attainable. This suggests that for a wide range of parameters, the microtubule bundles will become unipolar with minus-ends against the interface.

3.5.2 Model of mixed polarity bundles

The second problem is that it is not clear that a mixed polarity bundle can give rise to the motion seen in experiment. Here we analyze this possibility by using simulation methods similar to what was used previously to understand molecular motor dynamics [2]

We assume that the microtubules are inextensible and that opposite polarity microtubules apply forces in equal and opposite directions. We discuss the different forces separately.

First there is an effective attractive interaction between microtubules independent of their polarities induced by the presence of PEG polymers. We choose a short range force so the monomers separated by a distance \mathbf{r} within a range σ_s will feel an attractive force due to depletion forces as discussed above. To simplify the expressions we use a normalized unitless distance $\Delta \equiv \mathbf{r}/\sigma_s$. The force between any two monomers for $\Delta < 1$ is taken to be

$$\mathbf{f}_{attr} = f_a \Delta^4 (1 - \Delta^{12})^3 \mathbf{r} \quad (3.7)$$

where f_a is the strength of the attractive interaction. The reason for choosing this

functional dependence on Δ was to produce a force that was close to constant for $\Delta < 0.6$, and then drop smoothly to zero, so as to work well with the Runge Kutta algorithm.

Second, we introduce an even shorter range repulsion between monomers that diverges at a hard core radius σ_h and goes to zero at σ_s :

$$\mathbf{f}_{rep} = f_r \left(\frac{1}{r^2 - \sigma_h^2} - \frac{1}{\sigma_s^2 - \sigma_h^2} \right)^4 \mathbf{r} \quad (3.8)$$

where f_r is the strength of the repulsive interaction.

Third, we introduce an equal and opposite forces between monomers on opposite polarity microtubules that are within a distance σ_s . The direction of the force is as follows. We compute the tangents to both monomers as $(\mathbf{r}_{i+1} - \mathbf{r}_{i-1})/2$. Then we choose the direction \mathbf{t} , to be the average of these two tangents. The magnitude of the kinesin force is

$$\mathbf{f}_{kin} = f_k (1 - \Delta^{12})^3 \quad (3.9)$$

where f_k is similar the symbol used previously and denotes the magnitude of the kinesin force.

These forces are added to the elastic forces, viscous drag, and tension that must be introduced to conserve link length and the equation of motion is iterated using a method for updating chains with constant link length [61, 62].

We also tried two separate kinds of boundary conditions. First, tethering the chains to fixed points on the surface which we will call “fixed” boundary conditions. Second, confining the chain ends to a two dimensional plane but letting the ends move

within that plane, which we will call “sliding” boundary conditions.

We tried a wide range of parameters, of different elastic constants, attractive interactions, number of microtubules, and boundary conditions. What we found is now summarized.

For two chain bundles of opposite polarity we did find a set of parameters which showed movement of the bundle with: $f_r = 10.0$, $\sigma_s = 2$, $\sigma_h = 1$, $f_a = 3$, $f_k = 0.2$, $C = 100$, and chain length of 20.

For larger bundle sizes, e.g. 9 chains, we did not find anything similar to experiments. With fixed boundary conditions, and started as a pillar of parallel microtubules with slightly randomized directions, the chains would settle down to a pillar shape that would not change with time for sufficiently small attractive interactions f_a , but when this became greater than a certain value that depends on elastic constant and other parameters, it would suddenly collapse into a ball because this is more highly favored energetically.

When we chose sliding boundary conditions, and for sufficiently weak attractive interactions, $f_a = 1$ there was a regime where there was twisting motion inside the pillar but then the minus microtubules would suddenly slide off of the plus ones, finally lying close to parallel with the plane of attachment, see supplemental movie S10. It therefore appears that a two microtubule bundle moves because of a strong anisotropy in forces seen in cross sections. In larger bundles, the forces through the bundle are more homogeneous which acts to stabilize them.

We conclude that by direct physical modeling of a mixed polarity bundle, it is

not clear if there are any reasonable parameters which show motion similar to what is seen in the experiments of Sanchez et al [1, 5].

Note that the elastic constant of a microtubule in a bundle will depend strongly on the rate at which it is bent. For very short times, the bonds between different microtubules caused by kinesin binding will be fixed in position giving the bundle the elastic constant of a cylinder of radius R which is $\propto R^4$. However the oscillations here take place on minute timescales. In that case the individual kinesin molecules have velocities of order $1\mu m/s$ so they unbind and move very far on this time scale. This allows neighboring microtubules to move relative to each other, to eliminate stress. Therefore on sufficiently long timescales, this reduces the elastic constant of a microtubule to that of one in isolation.

3.6 Results

Links to videos of select simulations are included in the appendix. Figure 3.5 shows some still frames of simulated arrays demonstrating metachronal wave behavior in both the planar and circular geometries.

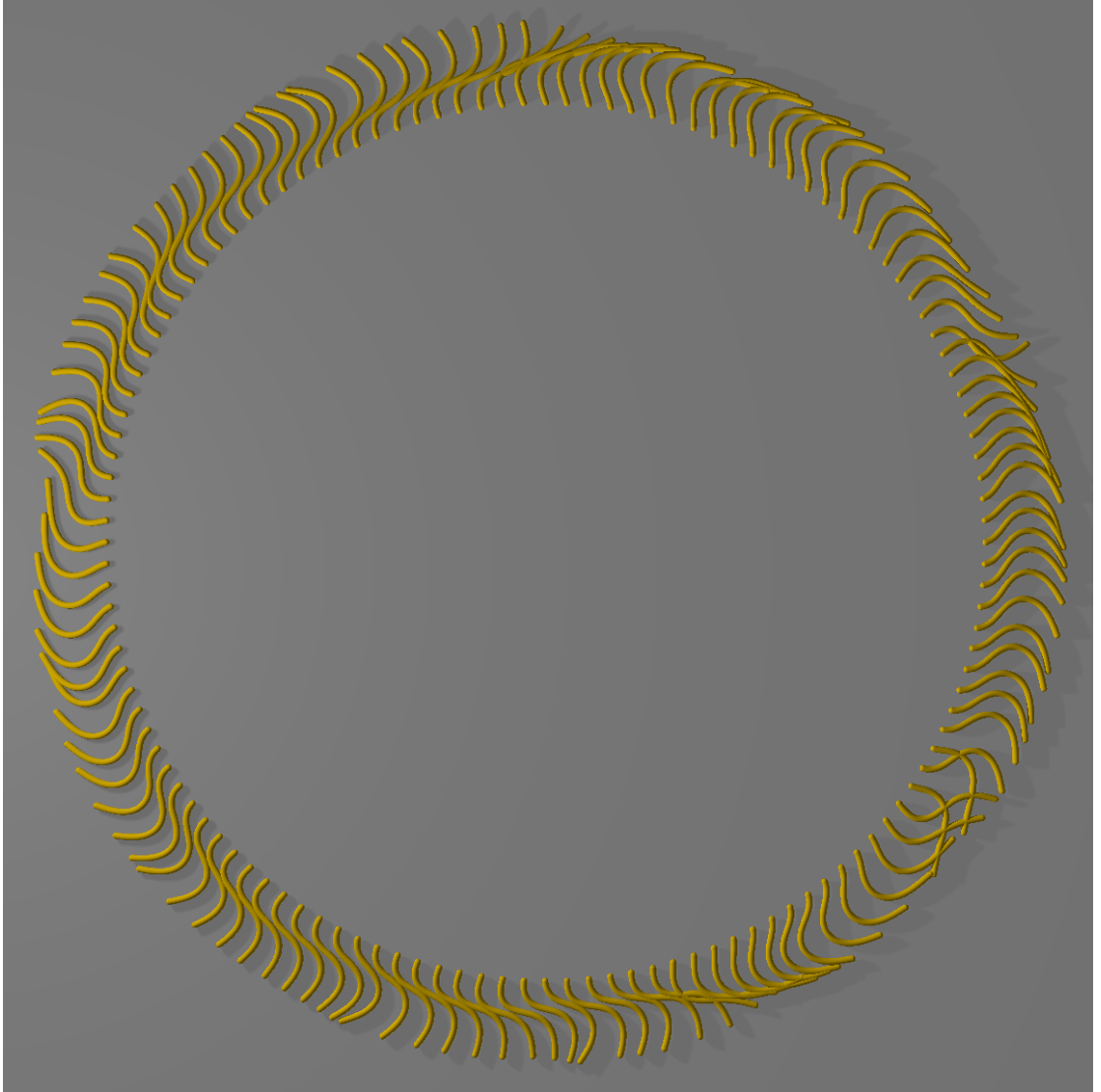
We characterize the behavior of each system using the correlation function

$$C(\Delta i, \Delta t) = \langle \Delta x(i + \Delta i, t + \Delta t) \Delta x(i, t) \rangle, \quad (3.10)$$

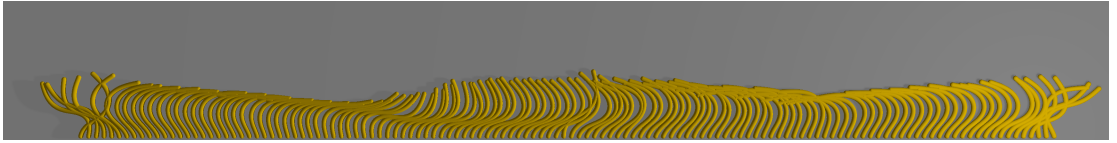
where

$$\Delta x(i, t) = x(i, t) - \langle x(i, t) \rangle.$$

Figs. 3.6, 3.7, and 3.8 show correlation functions for planar and a circular geometries



(a)



(b)

Figure 3.5: Simulated metachronal wave formation for 128-polymer arrays in (a) circular and (b) planar geometries. In both cases, $k_{o\text{seen}} = 0.1$, $k_{stiff} = 10.0$, $H = 1$.

(for the circular geometry, θ is the position variable rather than x). In the following, we will discuss these and examine how the system responds to changes in k_{Oseen} , k_{stiff} , and height H . It should be noted that changes in the viscosity or kinesin velocity and density (that affect f_k), can be absorbed into a rescaling of time, and of k_{stiff} .

The strength of the interaction tensor, k_{Oseen} , has a dramatic effect on the type of wave behavior seen, or whether it is observed at all. This strength is a function of the hydrodynamic effects of kinesin walking along microtubules, and will depend on their density and speed, as explained in detail in Ref. [14]. Figure 3.6 shows the correlation results of three 128-polymer simulations in the same circular geometry shown in Figure 3.5(a) for three different values of k_{Oseen} . There is an overall strengthening of the metachronal behavior as k_{Oseen} is increased from 0.1 to 0.2. The sign of the slope reflects the initial conditions of the system. Long lived waves travel predominantly in a single direction over long times scales resulting in a slope of the crests of the correlation function that can either be positive or negative. Similar crests are seen in the analysis of the real experimental data [1]. With this circular geometry, the correlation function must be periodic, which is why it rises again when i becomes large.

The polymer stiffness k_{stiff} also has an interesting effect on metachronal wave formation. Figure 3.7 shows the correlation functions for $k_{stiff} = 5.0, 10.0$, and 20.0 in a planar geometry. While Figs. 3.7(a-b) are qualitatively similar, we do see an apparent decrease in the metachronal wavelength. Figs. 3.7(c-d) show that if the polymer is made too stiff, no metachronal behavior is observed at all. In general, planar geometry appears to cause more coherence in the motion of the different bundles, and

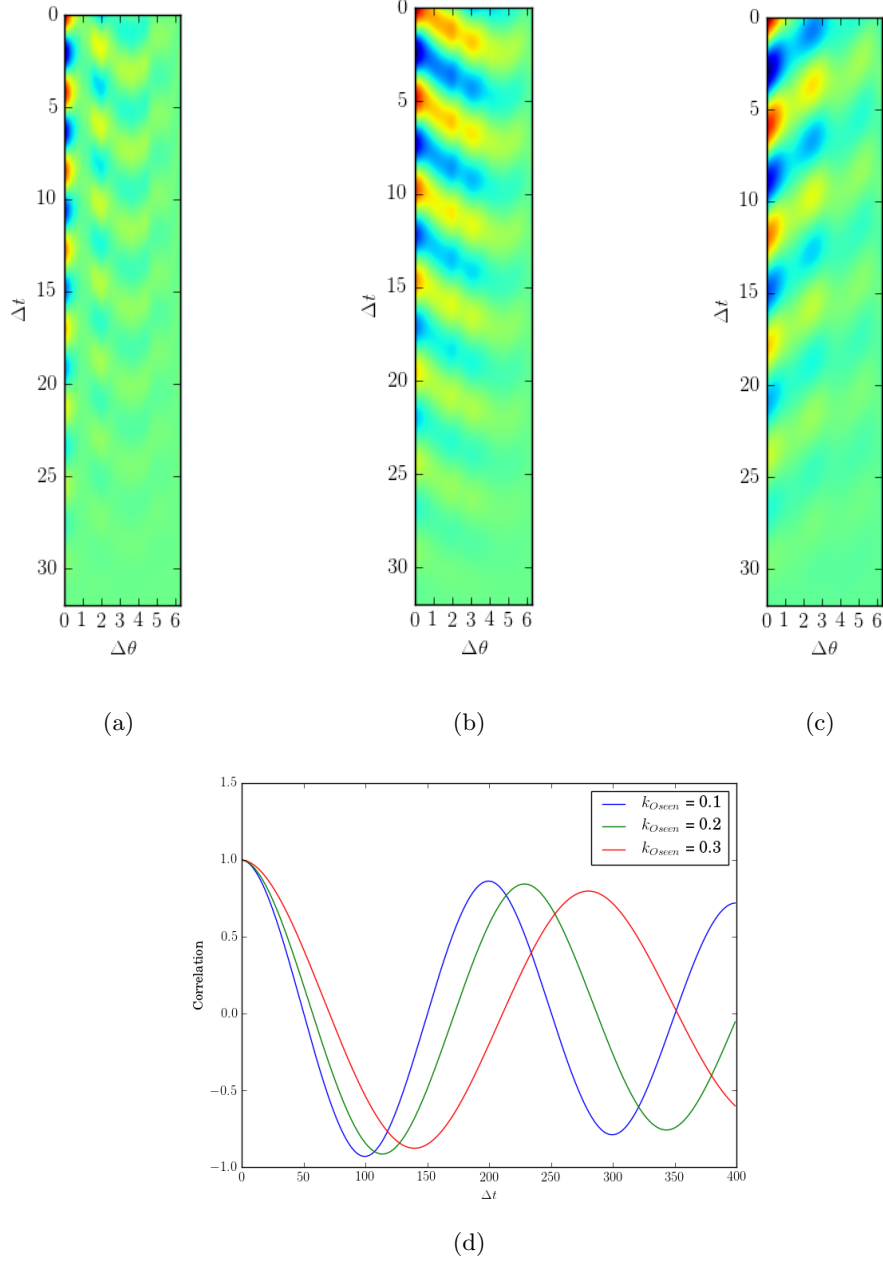


Figure 3.6: Full correlation functions for circular geometry with $H = 1$ and $k_{stiff} = 10$, with $k_{Oseen} = 0.1, 0.2$, and 0.3 (a-c, respectively). The correlation function at $\Delta i = 0$ for all of these values of k_{Oseen} are shown in (d).

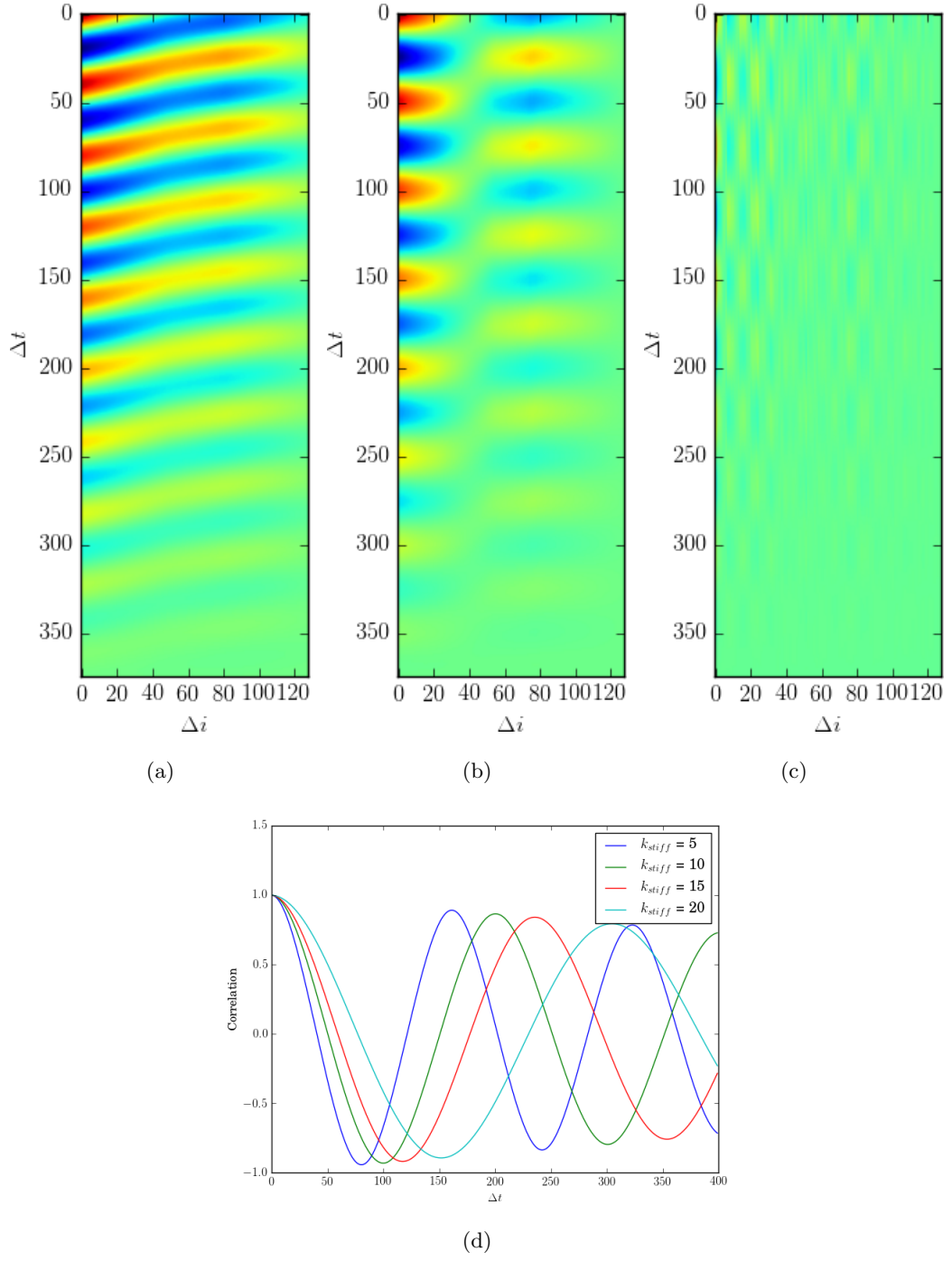


Figure 3.7: Full correlation functions for planar geometry with $H = 1$ and $k_{Oseen} = 0.1$, with $k_{stiff} = 5.0, 10.0$, and 20.0 (a-c, respectively). The correlation function at $\Delta i = 0$ for all of these values of k_{stiff} are shown in (d).

the correlation function is dominated by motion at the longest lengths and time scales.

The distance between plates, H , has a considerable effect on the dynamics as well. Longer range, more coherent motion is observed when H is larger, and short range, less coherent motion when H is small. See Figure 3.8. This is to be expected due to the strong screening effect that these boundary conditions impose. Smaller H reduces the hydrodynamic coupling, causing a decrease in coherence.

3.7 Discussion

When comparing these results to those of Sanchez et al., we find that the basic features agree. The videos linked in the appendix qualitatively mimic the experimental videos, and the experimental correlation analysis agrees quite well with the simulations. More importantly, this agreement between theory and experiment was reached from first principles. We only use a handful of forces in our simulations, and each force has a physical justification for being used.

There are potential shortcomings of this model that may result in some differences between experiment and theory. The first is that the experiments observe bundles of microtubules that taper away from their base. The hydrodynamics are not expected to be uniform along the length of a chain. In addition these bundles will, for short enough times, behave like rigid material, but for longer times, because they are connected through walking kinesin molecules, will behave more as individual microtubules with a greatly reduced elastic constant. On the time scales of the motion, we expect

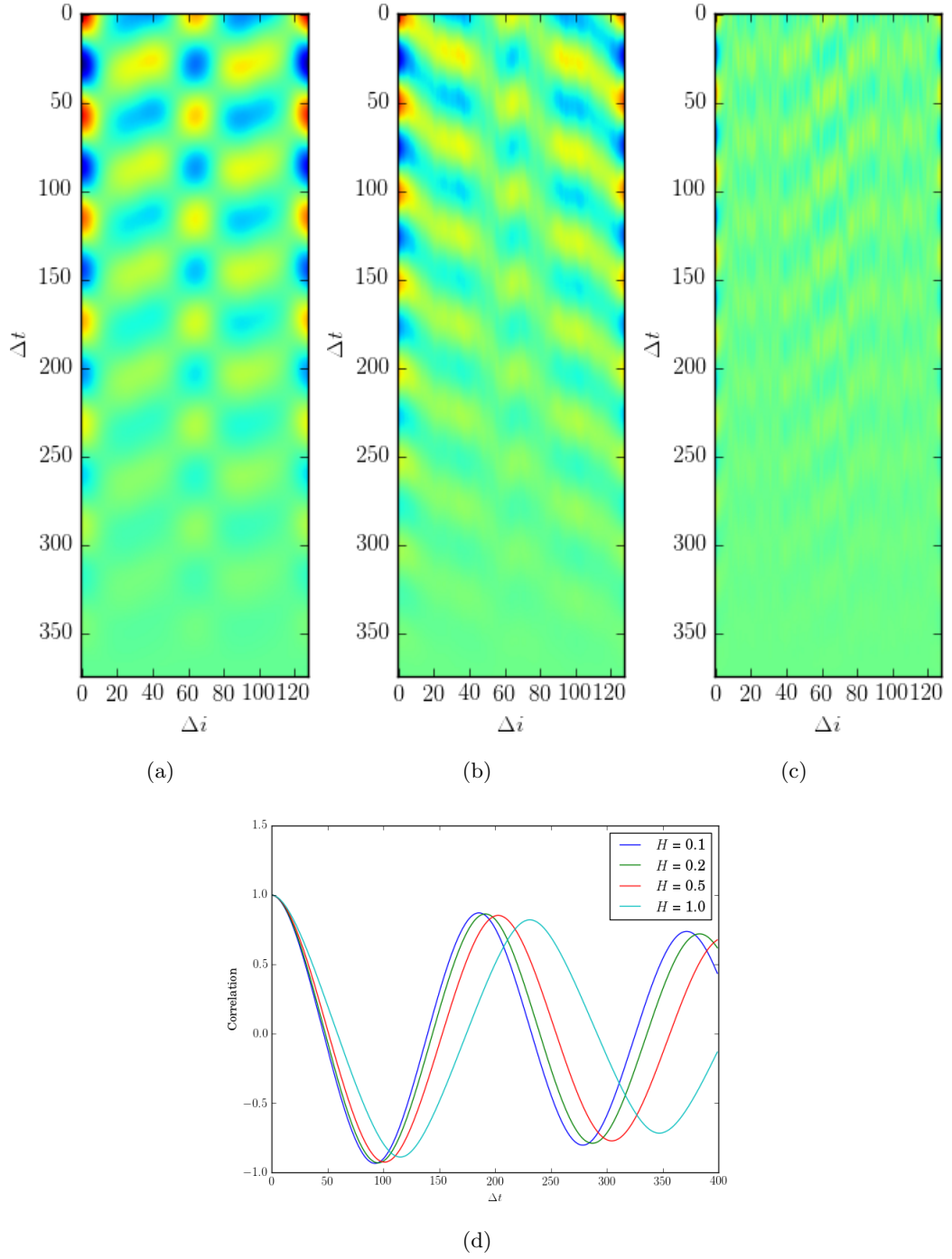


Figure 3.8: Full correlation functions for circular geometry with $k_{stiff} = 10$, $k_{Oseen} = 0.2$, and $H = 1.0, 0.5$, and 0.1 (a-c, respectively). The correlation function at $\Delta i = 0$ for all of these values of H are shown in (d).

to be in the latter regime. However the details of the hydrodynamics and elasticity in these bundles is still not understood experimentally. In fact, as we mentioned earlier, the polarity of individual MT's is not known experimentally, and arguments for their unipolarity are given in 3.5. But still, the basic mechanism of dynamic buckling due to kinesin drag, and metachronal waves being generated by hydrodynamic coupling is robust over a wide parameter range, so we believe that these complications, aside from unipolarity, will not alter the basics of our explanation.

At a more technical level, there are other things that may make a slight difference to the results here. The bundles are constrained to move only in the xy -plane, and while it is true that MT motion is nearly 2-dimensional, there is some room in the z -direction that MT bundles can occupy. Additionally, this model does not account for the fluid boundary condition at the anchoring surface. This may introduce some errors if a monomer becomes close ($\sim H$) to the anchoring plane. However, because of the screening effects of the plates, this should not alter the behavior at distances large compared to the plate separation. We have tested for this by adding image charges to the planar case, and found that their effects on correlations are small, as expected.

3.8 Conclusions

In conclusion, we have developed a model for the spontaneous formation of wavelike behavior in active polymer arrays that only requires two ingredients: semi-flexible chains tethered to a surface, and motors walking from their bases to their tips.

The hydrodynamics in their confined geometry gives rise to metachronal waves that appear remarkably similar to what is observed experimentally [1, 5]. There is no need to posit additional mechanisms that force individual bundles to oscillate. This all happens as a consequence of Newton's laws and fluid mechanics, allowing us to gain a better understanding of how metachronal waves form with considerable predictive power. As such, we have examined new parameter spaces and have demonstrated boundaries between different types of metachronal behavior and regimes in which no metachronal behavior exists. It would be of great interest to test these predictions experimentally. Given the simplicity and robust nature of this mechanism, and the ubiquity of microtubules and kinesin in cells, it gives one further impetus to look for other places in biology where this kind of behavior can be found.

Chapter 4

Spontaneous Circulation of Active Microtubules Confined by Optical Traps

4.1 Introduction

The study of active fluids – fluids which have a source of internal propulsion, as is common in biology – has been of interest for several decades. In more recent years, several experiments have demonstrated remarkable emergent phenomena using mixtures of microtubules and kinesin fueled by ATP. Kinesin is a motor protein that binds to a microtubule in such a way that, when powered by ATP, tends to “walk” along the microtubule in a particular direction governed by the microtubule polarity. As the kinesin moves, it feels a drag force by the surrounding fluid. This has the effect of pushing the fluid in the direction that the kinesin is moving, as well as (by Newton’s third law) exerting a force on the microtubule in the opposite direction. As

such, flows can be observed in the fluid with no external impetus, from vortex lattices [63] to 2-dimensional active nematics [64, 65] to macroscopic coherent flow [66].

In what follows, we use first-principles hydrodynamic simulations to show the types of behavior (e.g. spontaneous circulation) of confined microtubules. We propose an experiment in which microtubules are held in place by an optical trap. To aid in this, we show the feasibility of such an experiment by first calculating the laser power required to contain a bending microtubule, and then we derive the change in temperature one might expect for such an experiment.

We then discuss the methods of simulation. While the specifics of the simulation are somewhat complicated, it uses no phenomenology. In fact, it has (in slightly adapted forms) been used to successfully reproduce and offer important insights into the phenomena of cytoplasmic streaming in *Drosophila* oocytes [14] and metachronal wave formation in microtubule bundles [3].

The results of the simulations themselves are then presented, in which we identify qualitatively different kinds of observed motion. We examine the dependence of these outcomes on parameters, and provide some interpretation. In addition to examining the motion of the polymers themselves, we also calculate and present analysis of the fluid motion in the near- and far-field. We then perform a power spectrum analysis of the angular momenta of polymers to give some concrete metrics for determining phase.

4.2 Preliminary Estimations

Before going in-depth into predictions as to what will happen if microtubules are contained in an optical trap, we should first address whether it is feasible to do so given typical issues common in optical trapping.

4.2.1 Laser frequency

For biological applications, lasers with wavelength > 1000 nm are typical, as this reduces damage to cells [67, 68]. However, even from the beginning of its usage, optical traps with wavelengths in the visible regime have been successfully used for sub-cellular structures [69]. In what follows, we consider a range of wavelengths from 500 nm to slightly over 1000 nm.

4.2.2 Forces

Microtubules confined in an optical trap would bend, and it is useful to get a sense of whether an optical trap would exert a sufficient force to keep the microtubules contained. In what follows, we use typical values to argue that an optical trap with reasonable intensity would be enough to overcome the microtubule rigidity.

The most common and straightforward approach to optical trapping uses a tightly-focused Gaussian beam in the TEM₀₀ mode. For such a beam, the intensity of the radiation as a function of radial position can be written as

$$I(r) = \frac{2P}{\pi w^2} \exp\left(-\frac{2r^2}{w^2}\right) \quad (4.1)$$

where P is the power of the laser and w is the radius of the beam cross section. Because the diameter of a microtubule is 24 nm and the smallest the beam diameter can be is on the order of the wavelength $\lambda \sim 500$ nm, we use the electric dipole approximation

$$\mathbf{F} = \frac{1}{2}\alpha\nabla E^2 \quad (4.2)$$

where α is the induced dipole of the trapped particle. For a sphere of radius a ,

$$\alpha = 4\pi n_0^2 \epsilon_0 a^3 \frac{m^2 - 1}{m^2 + 2}, \quad (4.3)$$

where $m \equiv n_1/n_0$; n_0 and n_1 being the refractive indices of the surroundings and the sphere respectively [70]. Because, for a monochromatic wave, $I = \frac{c\epsilon_0 n_0}{2} E^2$, we rewrite 4.2 as

$$\mathbf{F} = \frac{4\pi n_0 a^3}{c} \frac{m^2 - 1}{m^2 + 2} \nabla I \quad (4.4)$$

In terms of the Gaussian beam described by equation 4.1,

$$F(r) = -\frac{32n_0 a^3 P r}{c w^4} \left(\frac{m^2 - 1}{m^2 + 2} \right) \exp\left(-\frac{2r^2}{w^2}\right) \quad (4.5)$$

For a bending microtubule, the elastic restoring force per unit length will be

$$f_{el} = C \left| \frac{d^4 \mathbf{r}}{ds^4} \right| \quad (4.6)$$

If the microtubule is circling the optical trap, then this becomes

$$f_{el}(r) = \frac{C}{r^3} \quad (4.7)$$

Where r is the radius of circulation. If we now model the microtubule as a chain of beads (each bead having radius a), then the elastic force on a single bead would be

$$F_{el}(r) = \frac{2aC}{r^3} \quad (4.8)$$

Equating Eqs. 4.8 and 4.5 and solving for P gives the power required to contain a microtubule circling at radius r ,

$$P(r) = \frac{cCw^4}{16n_0a^2r^4} \left(\frac{m^2 + 2}{m^2 - 1} \right) \exp \left(\frac{2r^2}{w^2} \right) \quad (4.9)$$

This is minimized at $r = w$, meaning the minimum power required to contain a microtubule is

$$P_{min} = \frac{cCe^2}{16n_0a^2} \left(\frac{m^2 + 2}{m^2 - 1} \right) \quad (4.10)$$

The microtubule stiffness C has been measured to be approximately $1 \times 10^{-23} \text{ Nm}^2$ [71, 72]. The refractive index of water is $n_0 = 1.33$, and the refractive index of tubulin has been measured to be $n_1 \approx 2.5$ [73, 74]. Modeling the microtubule as a string of beads of radius a means $a \approx 12 \text{ nm}$. Using these quantities, we find that $P_{min} \approx 16 \text{ W}$. This is quite large compared to standard lasers used for optical traps, but it should be emphasized that when a group of microtubules are circling an optical trap, each individual microtubule often has a radius of curvature larger than the radius of the trap if the length of the microtubule is on the order of, or less than, the trap radius (see images in Section 4.4). The minimum power input $P_{min} \propto b^{-3}$ where b is the polymer radius of curvature, so even a factor of 2 increase (i.e. let $b = 2r$) reduces P_{min} to only 2 W.

4.2.3 Heating

The relatively large laser power required to perform this proposed experiment raises some concerns about heating in the system, and it is worthwhile to address the

degree of heating one might expect so that an experiment may be properly designed. It has been shown [75] that for a Gaussian beam, the change in temperature at the center of the optical trap of uniform absorbance is approximately

$$\Delta T(r=0) \approx \frac{\alpha P}{2\pi C} \left[\ln \left(\frac{2\pi R}{\lambda} \right) - 1 \right], \quad (4.11)$$

where α is the absorption coefficient, P is the laser power, C is the thermal conductivity, λ is the laser wavelength, and R is a characteristic distance ($R \gg \lambda$) to a boundary at which temperature is held constant, often taken to be the distance to the glass slide in experiments. If the experiment is performed on water, it should be noted that α is highly dependent on λ , but this dependence has been thoroughly studied [76].

Fig. 4.1 shows $\Delta T(r=0)/P$ as a function of λ for water, letting $R = 10 \mu\text{m}$. From this, we can see that, for a 20 W laser, wavelengths longer than $\sim 700 \text{ nm}$ quickly become unfeasible, as this would lead to temperature increases of 20 K or more. However, wavelengths shorter than 700 nm would likely only heat by 5-10 K.

Adding microtubules to the optical trap would increase the temperature further, as the absorbance of proteins tends to be several orders of magnitude larger than that of water. However, an important implication of the calculation in the previous section is that the trap radius has no effect on the power required to confine the microtubules. This means that, if needed, the radius could be increased (and microtubules made longer) in order to reduce the relative area of the microtubules. For example, a $1 \mu\text{m}$ long, 24 nm diameter microtubule takes nearly 1% of the area of a trap of radius $1 \mu\text{m}$. If the length of the microtubule and the radius of the trap are both increased to

10 μm , the area fraction per microtubule reduces by a factor of 10 to under 0.1%.

Furthermore, the assumption that the optical trap is far from the plates will not necessarily be true, and therefore the calculations above should be seen as an upper bound on heating. Two plates separated by a very thin gap (on the order of or even less than the radius of the trap) may be used, as the hydrodynamics of this are accounted for in the simulations that follow. This would further increase the ability of the slides to dissipate heat, especially if the slide material is chosen to have high thermal conductivity and low absorbance at the desired wavelength. Sapphire substrates have been used for this purpose as it has ~ 20 times the thermal conductivity than borosilicate glass [77], but quartz (~ 3 times the thermal conductivity of water) would likely also be a viable choice.

4.3 Method of simulation

This simulation was adapted from previous work used to successfully model cytoplasmic streaming and metachronal wave formation [14, 3], and more detailed explanations of what follows can be found in these papers. This is a first-principles simulation, and at a high level utilizes a straightforward approach. Microtubules are expressed as polymers, each made of a chain of N monomers bound together by a spring force which separates them by a distance $\ell = 1$. A group of M polymers is initialized, and various forces act on them. The i th monomer position and velocity are updated using a

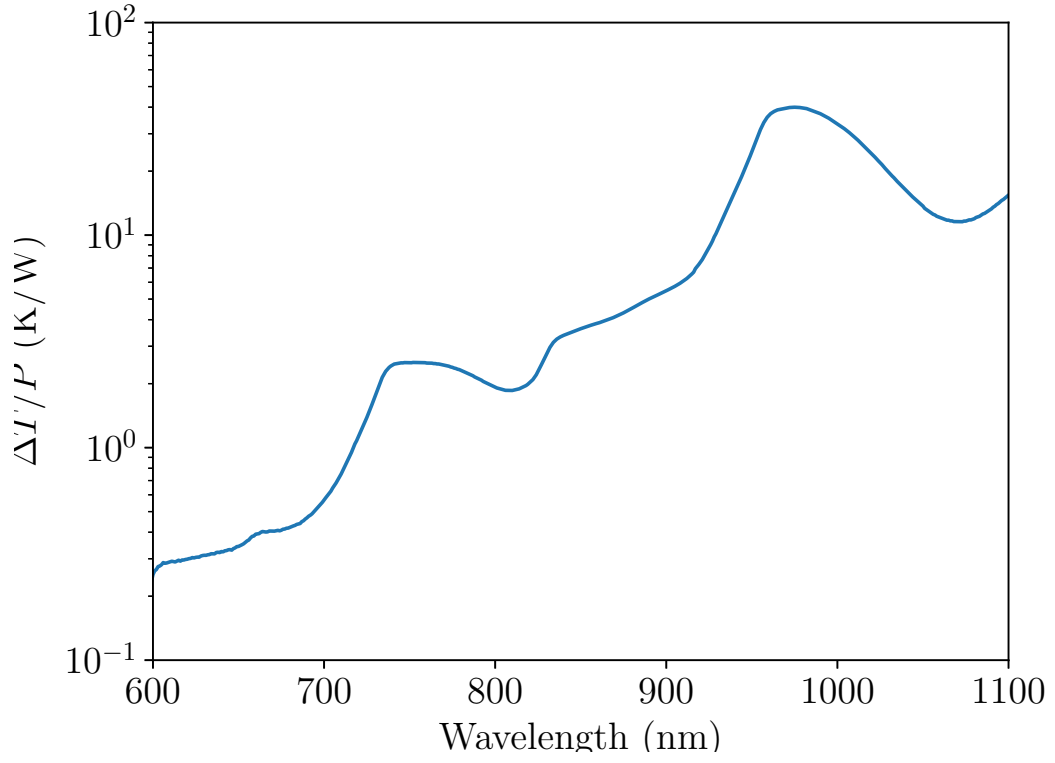


Figure 4.1: Predicted increase in temperature per watt at the center of the optical trap as a function of laser wavelength. The trap is assumed to only contain water a distance of $10\ \mu\text{m}$ from a thermally conducting plate. The lower bound of the plot terminates at 600 nm because at this point the absorption coefficient of water becomes similar to that of glass, and the constant temperature boundary condition approximation becomes questionable.

fourth-order Runge Kutta integration of the equation

$$\frac{d\mathbf{r}_i}{dt} = \mathbf{u}(\mathbf{r}_i) - k_{kin}(\mathbf{r}_{i-1} - \mathbf{r}_{i+1}) \quad (4.12)$$

where $dt = 0.003$ is the time step, $k_{kin} = 0.2$ corresponds to the strength of the kinesin drag force tangent to the polymer (see following section), and $\mathbf{u}(\mathbf{r}_i)$ is the fluid velocity due to all other forces.

The polymers are initialized in the trap in a zig-zag pattern, alternating polarity, with random noise given to each monomer's initial position. This is more computationally efficient than true Monte Carlo initialization, and we observed no noticeable difference in simulation outcome.

4.3.1 Kinesin drag force

The drag force propelling the microtubules depends on the concentration of kinesin. Kinesin bind preferentially to microtubules, meaning that a relatively low concentration of kinesin in the solution will result in a high concentration of kinesin on the microtubules. Suppose that these kinesins are modeled as a linear train of spheres (radius a) separated by distance d and moving at speed v_0 . It has been shown [14] that, far from the kinesin, the fluid velocity is the same as that due to thin cylinder moving at speed $(a/d)v_0$. In terms of equation 4.12, $k_{kin} \propto a/d$.

The above demonstrates that there are two main ways of tuning k_{kin} experimentally: one can change the kinesin concentration (effectively changing d), or one can add cargo to the kinesin (changing a). Explicitly adding cargo for kinesin to transport

is not strictly necessary – many studies have shown active matter phenomena using no added cargo (although it is possible the kinesin are transporting segments of microtubule). This being said, the size of the dragged cargo is not particularly important in itself: a well-known result of slender-body theory is that the drag force F on a cylinder moving parallel to its axis is

$$F \sim \frac{2\pi\mu\ell u}{\ln(\ell/a)}, \quad (4.13)$$

where μ is the dynamic viscosity, u is the cylinder speed (relative to the far-field fluid), and ℓ is the cylinder length. This is only logarithmically dependent on the cylinder radius a . Much more important is the ratio a/d , as $u \propto a/d$ for the kinesin train.

4.3.2 Description of other forces

The forces that go into computing $\mathbf{u}(\mathbf{r}_i)$ in equation 4.12 are:

$$\mathbf{u}(\mathbf{r}_i) = J_{ii}\mathbf{F}_i + \sum_{i \neq j} \mathbf{F}_j \cdot \mathbb{G}(\mathbf{r}_i - \mathbf{r}_j) \quad (4.14)$$

Here, $J_{ii}\mathbf{F}_i = \mathbf{F}_i/4\pi\mu$ is the drag experienced by a small sphere, \mathbb{G} is the hydrodynamic interaction tensor (described in the following section), and \mathbf{F} is the sum of all forces on a monomer not related to kinesin drag or hydrodynamic interactions:

$$\mathbf{F}_j = \mathbf{T}_j + \mathbf{C}_j + \mathbf{W}_j + \sum_k \mathbf{H}_{jk} \quad (4.15)$$

where:

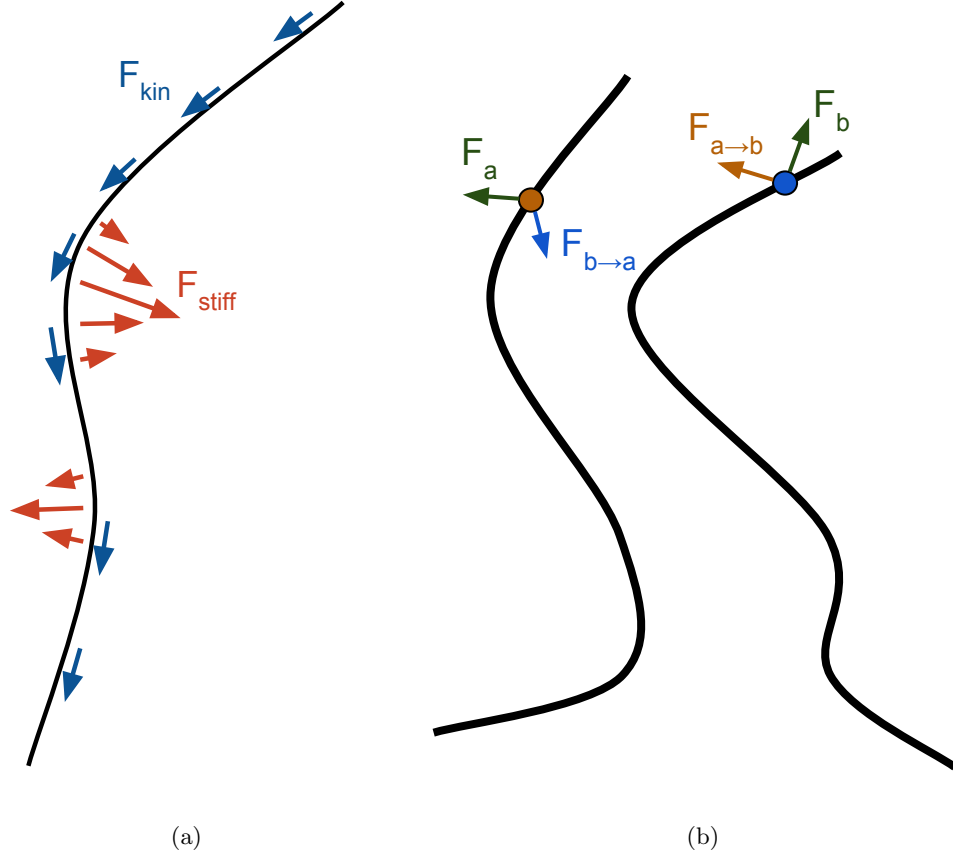


Figure 4.2: Illustrations of some of the important forces applied to simulated polymers. (a) shows stiffness and kinesin drag forces that a polymer experiences regardless of the existence of other polymers (part of the F terms in Eq. 4.14), and (b) gives an example of how polymers exert hydrodynamic forces on one another via the interaction tensor \mathbb{G} .

- $\mathbf{T}_j = k_{spr} [(|\mathbf{r}_{j-}| - \ell) \hat{\mathbf{r}}_{j-} + (|\mathbf{r}_{j+}| - \ell) \hat{\mathbf{r}}_{j+}]$

with $\mathbf{r}_{j\pm} \equiv \mathbf{r}_{j\pm 1} - \mathbf{r}_j$, is the spring force keeping monomer separation approximately constant. For our simulations, $k_{spr} = 100$ and $\ell = 1$.

- $\mathbf{C}_j = k_{stiff} (2\mathbf{r}_j - \mathbf{r}_{j+2} - \mathbf{r}_{j-2})$

is the stiffness force which resists polymer bending. This is equivalent to C in Eq.

4.6. k_{stiff} is varied in our simulations, with $0.02 \leq k_{stiff} \leq 10$.

- $\mathbf{W}_j = -k_{trap} \left| \frac{\mathbf{r}_j}{R} \right|^7 \hat{\mathbf{r}}_j$

is the trapping force which pushes all monomers radially inward. The r^7 dependence of the trap was used for computational efficiency as well as to let polymers travel freely within the trap while providing a firm boundary at the trap radius $r = R$. A spring force of the form $\mathbf{W}_j = -k_{trap}\mathbf{r}_j$ was also attempted, and similar (albeit somewhat less stable) types of behavior were observed. This was not used for analysis, however, because the trap radius is less well defined and the time required for polymers to exhibit collective behavior is significantly longer. $k_{trap} = 1.0$ for all simulations, and the trap radius R was varied between 2.5 and 10.0.

- $\sum_k \mathbf{H}_{jk} = k_{rep} \left[1 - \left(\frac{d_{rep}}{|\mathbf{r}_j - \mathbf{r}_k|} \right)^4 \right] (\mathbf{r}_j - \mathbf{r}_k)$

$$\text{if } |\mathbf{r}_j - \mathbf{r}_k| < d_{rep}$$

is a repulsive force between monomers that only acts if two monomers are very close to one another. For our simulations, we set $d_{rep} = 0.5$ and $k_{rep} = 1.0$.

4.3.3 Interaction tensor

The hydrodynamic interaction tensor \mathbb{G} is the same as that which was used previously to simulate metachronal wave formation [3], so we will only describe its significance at a high level here. As this is Stokes flow ($\text{Re} = 0$), the sum of non-hydrodynamic forces exerted on each monomer is transferred perfectly to the surrounding fluid. If the monomer is sufficiently small relative to the interaction distances, such a force can be modeled as a point force (known as a stokeslet). The exact solution for the velocity field $\mathbf{v}(\mathbf{r})$ due to a free stokeslet as derived by Oseen has been known for nearly a century:

$$\mathbf{v}(\mathbf{r}) = \frac{1}{8\pi\mu} \mathbf{F} \cdot \mathbb{J}, \quad (4.16)$$

where

$$\mathbb{J} \equiv \frac{1}{r} \left(\mathbb{I} + \frac{\mathbf{r} \otimes \mathbf{r}}{r^2} \right) \quad (4.17)$$

is known as the Oseen tensor.

The interaction tensor used in this study is a simplified version of the solution derived by Liron and Mochon for a stokeslet between two infinite flat parallel plates [15, 3]. We assume that microtubules in the proposed optical trapping experiment would be confined approximately halfway between two glass slides (separated by distance $H = 1.0$). For this reason and for computational efficiency, we confine all monomers to this plane in all simulations.

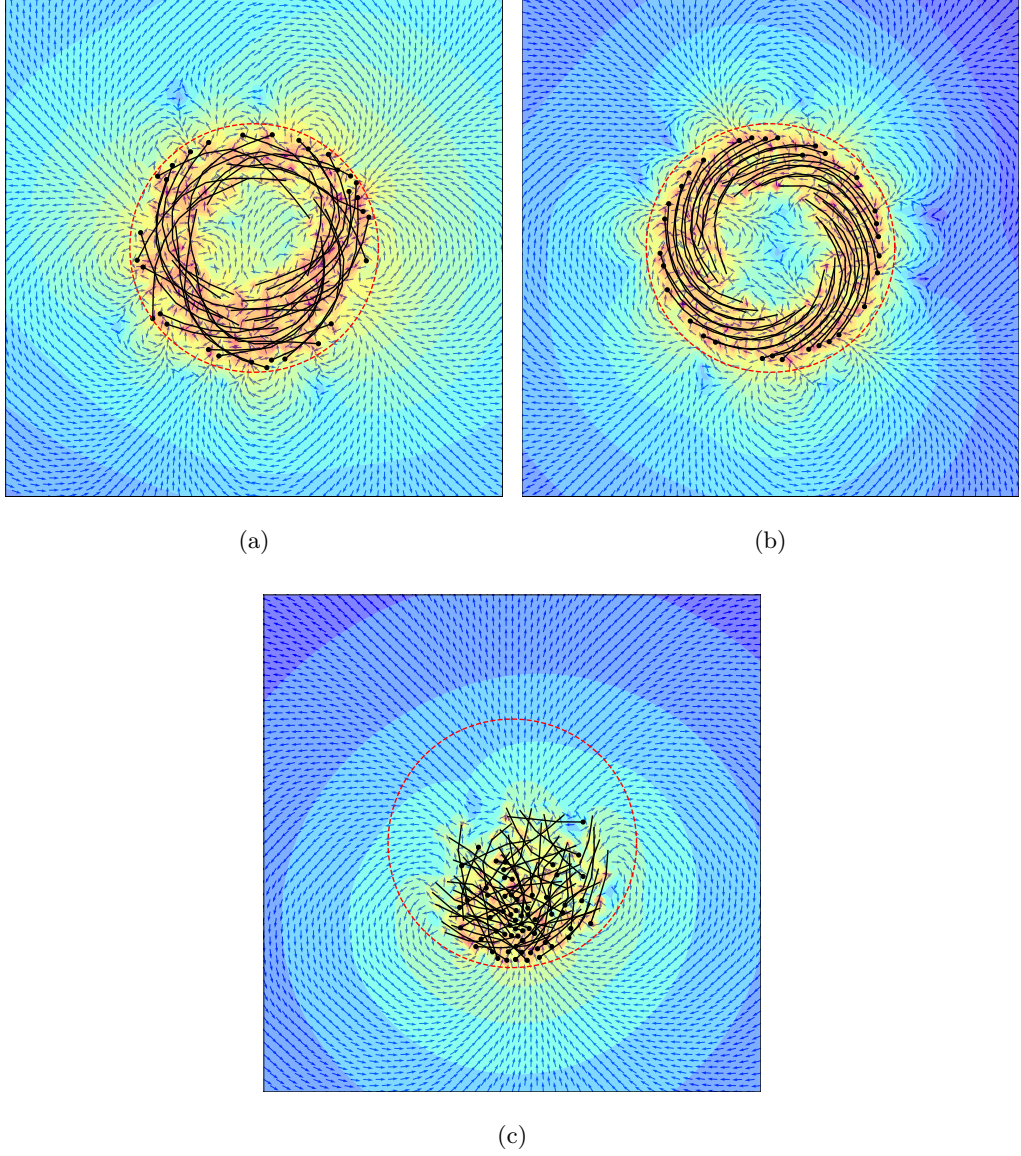


Figure 4.3: Quiver plots showing the direction of fluid flow in the vicinity of the polymers (black curves, with black circles indicating polarity) caught in the trap (dashed red circle). Color map is overlaid to show relative magnitudes of fluid velocity. (a) Uncorrelated circulation, using 32 polymers of length 8 and $k_{stiff} = 2.0$. (b) Correlated circulation, using 32 polymers of length 8 and $k_{stiff} = 0.5$. (c) Stasis, with 64 polymers of length 4 and $k_{stiff} = 0.5$. See the appendix for a link to animations of each of these.

4.4 Results

In what follows, we describe the sorts of behaviors that emerge depending on input parameters. A link to animations of simulated behavior is provided in appendix. We then analyze the velocity in the surrounding fluid to give a sense of the mixing ability of each type of behavior.

4.4.1 Types of microtubule motion

While the motion of simulated polymers was often complex, we classify behavior into three categories: uncorrelated circulation, correlated circulation, and stasis. These are broad classifications: the descriptions provided are qualitative, and many parameter choices exhibit intermediate behavior. Below is a description of these categories, and section 4.5 gives further information regarding how certain parameters affect the behavior exhibited by the system.

4.4.1.1 Uncorrelated circulation

If polymers do not interact sufficiently (i.e. if k_{Oseen} is small) or polymer density is low, then each polymer tends to act independently of other polymers. As such, there is no symmetry breaking: approximately the same number of polymers circulate clockwise as counter-clockwise. Correspondingly, the polarity of the microtubules is mixed.

4.4.1.2 Correlated circulation

If k_{Oseen} is increased and the density of polymers is sufficient, then correlated circulation is often seen: that is, polymers interact strongly enough and the stiffness is low enough such that some polymers reverse direction, breaking symmetry to exhibit organized circulation in a single direction. The polarity of the microtubules are all in the same direction, consistent with the circulation of the system.

4.4.1.3 Stasis

If polymers interact strongly but the polymer length is short compared to the trap diameter, the stiffness is too low, or the polymer density is too high, then no circulation occurs. Polymers interact but are unable to change direction, resulting in a cluster of polymers that remains largely stationary, with occasional and irregular changes in direction. Here static rotational symmetry is broken, with the microtubules clustered in one region of the trap away from the middle.

4.4.2 Fluid velocity field

Fig. 4.3 shows the direction of the velocity field for the three types of motion discussed in the previous section. We immediately notice that the velocity field for circulation behaviors is irregular, while that of stasis resembles the flow field for a stokeslet. This suggests that the far-field behavior for polymers in stasis will be stronger than those in circulation. Fig. 4.4 shows the average fluid speed far from the trap for the same simulations as Fig. 4.3. Indeed, this is what we see: in the far field, fluid

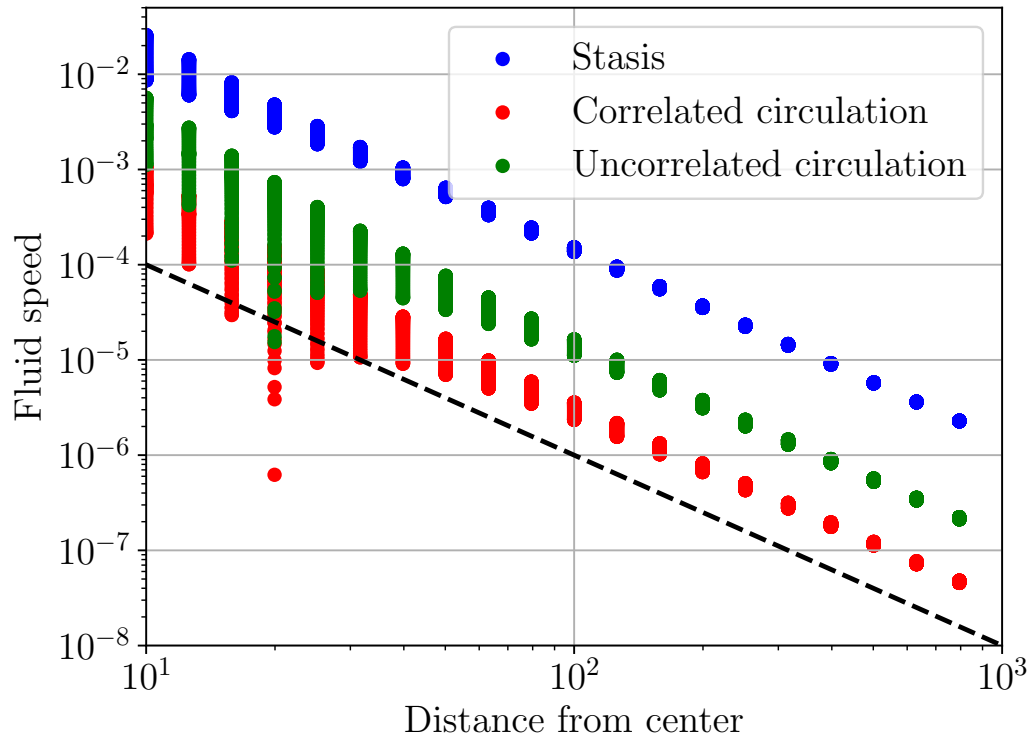


Figure 4.4: Fluid speeds plotted with respect to distance to the center of the trap, with trap radius $R = 5$, for the three simulations shown in Figure 4.3. The black dashed line is an example of $v \propto 1/r^2$ as a guide to the eye.

speeds due to polymers in stasis are an order of magnitude higher than polymers in uncorrelated circulation, and nearly two orders of magnitude higher than polymers in correlated circulation. Furthermore, we verify that fluid speeds for all cases drop off as $1/r^2$. This is not entirely unexpected, as this is the far-field behavior of the Liron-Mochon interaction tensor [15, 3].

4.4.3 Angular momentum power spectra

One method to quantify the differences between these types of behavior is to consider the power spectrum of the angular momentum. We first calculate the angular momentum of the j th monomer of the i th polymer,

$$\ell_{ij}(t) = \mathbf{r}_{ij}(t) \times \mathbf{v}_{ij}(t) \quad (4.18)$$

Note that, due to our 2D geometry, the cross product is always in the z -direction and can as such be treated as a scalar. We then sum these to find the angular momentum L_i of the i th polymer,

$$L_i(t) = \sum_{j=1}^N \ell_{ij}(t) \quad (4.19)$$

We then find the power spectrum for each polymer over time and sum these, i.e.

$$|\hat{L}|^2 = \sum_{i=0}^M |\hat{L}_i|^2 \quad (4.20)$$

where $\hat{L}_i(\omega) = \mathcal{F}[L_i(t)]$ is the Fourier transform of equation 4.19. Fig. 4.5(a)-(b) shows this power spectrum for the uncorrelated circulation and stasis phases. The correlated circulation phase is not shown as the power spectrum is very strongly peaked

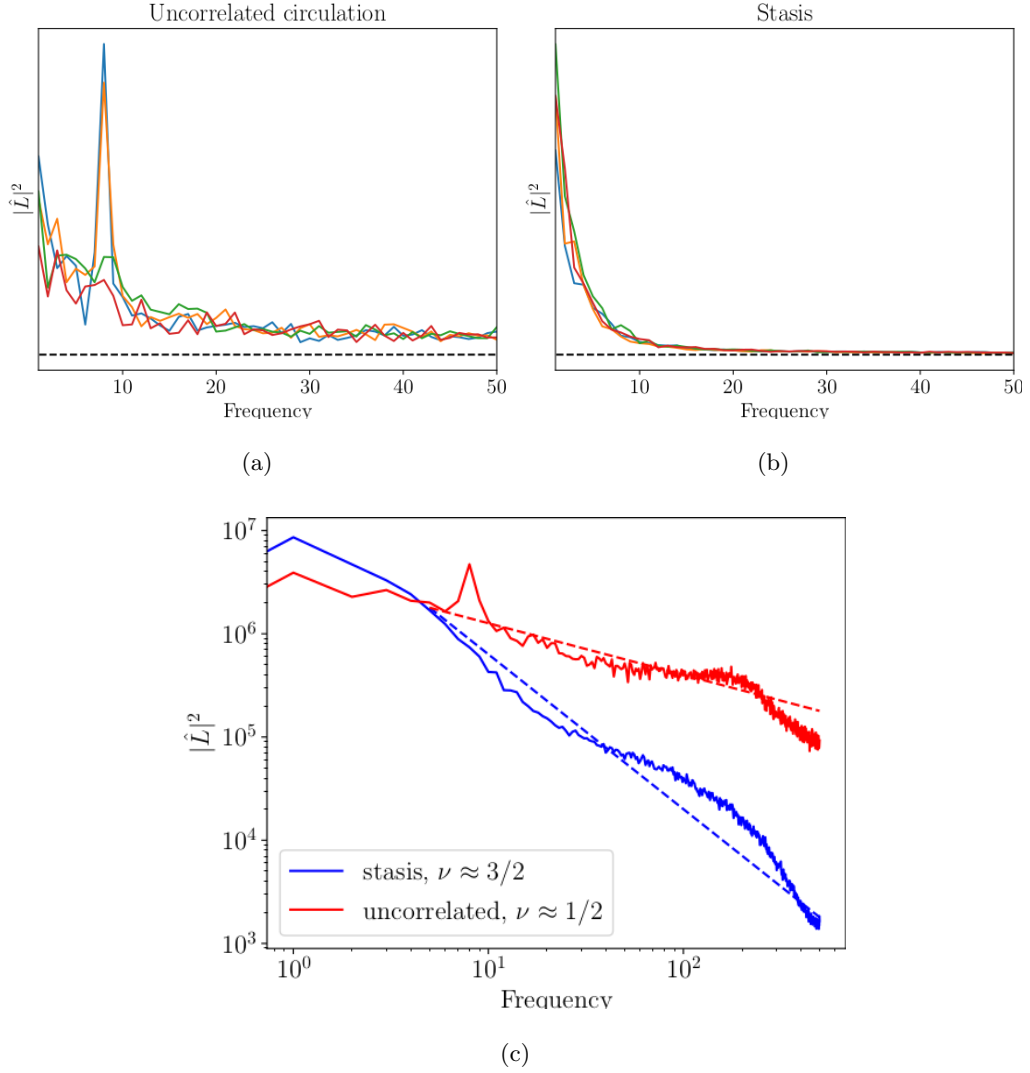


Figure 4.5: Plots showing the power spectrum of (a) uncorrelated circulation and (b) stasis, with identical system parameters as shown in Fig. 4.3(a) and (c), respectively. Each plot shows the power spectrum for four system initializations. Units on both axes are arbitrary. The power spectrum for correlated circulation is not shown, as it is so heavily peaked at zero frequency. Plot (c) averages the initializations from plot the other plot on a log-log scale. The dashed lines are a guide to the eye for $|\hat{L}|^2 \sim \omega^{-3/2}$ (blue) and $|\hat{L}|^2 \sim \omega^{-1/2}$ (red)

at frequency $\omega = 0$: that is, all polymers are more or less locked into stable circulation, and there is very little change in the angular momentum.

We immediately notice that the uncorrelated circulation state tends to have a single peak for $\omega > 0$. This makes sense, as any two given polymers circulating in opposite directions tend to collide twice per rotation, i.e. $\omega \approx \frac{2}{T}$, where T is the period of circulation. The power spectra in Fig. 4.5 were over a span of 1000 time steps (giving the x -axis units of $\Delta\omega = \frac{1}{1000}$), and the period of circulation for a single polymer was observed to be $T \approx 200$ time steps. Indeed, we see that $\omega_{peak} \approx \frac{2}{T} = \frac{1}{100} = 10\Delta\omega$.

Fig. 4.5(c) shows these same spectra on a log-log scale, but each averaged over its four initializations. The intent of this plot is to show that the power spectrum for the uncorrelated circulation phase has a much larger high-frequency tail compared to that of the stasis phase. Indeed, if we assume the power spectrum has the approximate form

$$|\hat{L}|^2 \sim \omega^{-\nu} \quad (4.21)$$

then this figure shows that $\nu \approx 3/2$ and $1/2$ for the stasis phase and the uncorrelated circulation phase, respectively.

In summary, this power spectrum is a very useful tool for determining type of motion:

- For the correlated circulation phase, $|\hat{L}|^2$ is essentially a delta function at $\omega = 0$.
- For the uncorrelated circulation phase, $|\hat{L}|^2$ has a distinctive peak at $\omega \approx \frac{2}{T}$, where T is the period of circulation. Additionally, for high frequencies, $|\hat{L}|^2 \sim \omega^{-1/2}$.

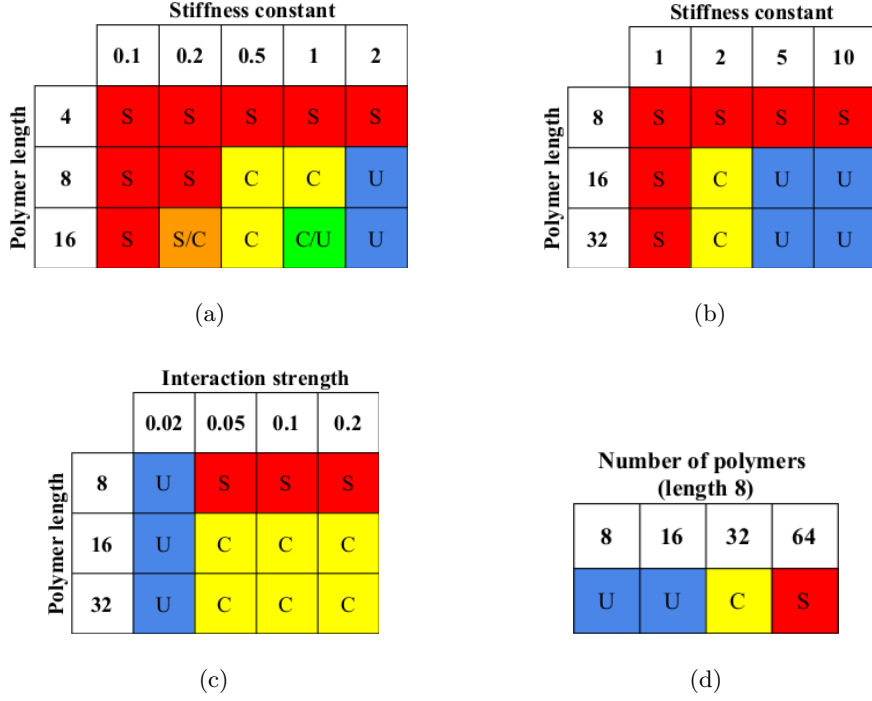


Figure 4.6: Tables showing the observed behavior (S = stasis, C = correlated circulation, U = uncorrelated circulation) as a function of input parameters. In all tables except (d), monomer density remains constant – e.g. there are double the number of polymers of length 4 as there were of length 8 in a similar run. (a) Trap radius = 5.0, 256 monomers, $k_{Oseen} = 0.1$. (b) Trap radius = 10.0, 1024 monomers, $k_{Oseen} = 0.1$. (c) Trap radius = 5.0, 256 monomers, $k_{stiff} = 0.5$. (d) Trap radius = 5.0, polymer length = 8, $k_{Oseen} = 0.1$, $k_{stiff} = 0.5$.

- For the stasis phase, $|\hat{L}|^2 \sim \omega^{-3/2}$ for high frequencies.

4.5 System behavior and simulation parameters

Several explorations into the effects of parameter tuning are summarized in Fig. 4.6. The key insights of these tables are that the correlated circulation motion is sensitive to polymer density and polymer length (relative to trap radius). It is also important to take scaling concerns into account: for example, if the trap radius is doubled, the

stiffness must be quadrupled in order to see analogous behavior. Simulations were also completed for a trap radius of 2.5, but correlated circulation was never seen for this radius (likely because the expected polymer length for circulation is now only 4, which does a poor job approximating an elastic rod).

4.6 Conclusion

We have shown that, under the right conditions, interesting and unique motions can occur for confined microtubules. While the design of such an optical trap experiment poses some challenges (a powerful visible-frequency laser would likely be required to contain microtubules while mitigating temperature increase), these are not prohibitive. In fact, we have shown that the trap radius should have no effect on the amount of power required to confine the microtubules, giving a fair amount of leniency in experimental design.

Three distinct types of polymer motion were identified and analyzed using first-principles simulations, with insights presented as to what parameter regimes might lead to preference of one type of motion over another. We also calculated velocity fields in the vicinity of the traps and in the far-field. These calculations are important for any future applications in mixing, as it shows that fluid motion is far more localized for correlated circular motion than for other phases (although $v \propto 1/r^2$ for all types of motion).

From an experimental perspective, it may seem as though many of the param-

eters varied in the simulations are not tunable. For instance, one cannot substantially vary polymer stiffness when dealing with real microtubules. However, it is possible to vary other experimental parameters to achieve the same effects. For instance, the stasis phase would more likely be encouraged with: (1) a very thin system, as this both increases the strength of hydrodynamic interactions and makes the microtubules less prone to sliding over one another when they have crossed; (2) with more kinesin (or cargo for kinesin added) to increase viscous drag; and/or (3) increased fluid viscosity. Any increase in hydrodynamic interactions would, in effect, be equivalent to lowering the microtubule stiffness. In fact, this is one of the reasons why it is believed that *Drosophila* oocytes transition from the slow to fast streaming phase. Experiments [78] show that loosening the actin network, and hence lowering the viscosity, causes premature fast streaming. The slow streaming phase shows some similarity to the stasis phase described above (characterized by slow uncorrelated motions where the microtubules appear disordered), and fast streaming resembles correlated circulation.

Although the hydrodynamics of the boundary would be different, a related system would be to place microtubules inside a hard-walled cylinder instead of an optical trap. Because of the strong hydrodynamic screening induced by the plates, the types of behavior seen in a hard-walled experiment may be similar to that of an optical trap if the height of the cylinder is much less than its radius. It might therefore be of interest to try to confine microtubules this way as well, perhaps by forming them in situ inside of a thin circular boundary (with radius on the order of the microtubule length) that is then confined between two plates. In addition to having fewer design obstacles, such

an experiment would also perhaps be more representative of intracellular systems.

The experimental confirmation of this effect would have important implications. For instance, the core forces and geometry of this work are very similar to those present in active nematics [64, 65], so understanding this behavior would be highly relevant to such systems. Such experiments could also provide a logical next step to applications in localized mixing in microfluidics.

Bibliography

- [1] T. Sanchez, D. Welch, D. Nicastro, and Z. Dogic. Filler. *Science*, 333(6041):456–459, 2011.
- [2] Joshua M Deutsch and Stephen E Martin. Photomechanical energy conversion using polymer brush dissociation. *Macromolecules*, 48(18):6703–6712, 2015.
- [3] Stephen E Martin, Matthew E Brunner, and Joshua M Deutsch. Emergence of metachronal waves in active microtubule arrays. *arXiv preprint arXiv:1806.06993*, 2018.
- [4] Stephen E Martin, Matthew E Brunner, and Joshua M Deutsch. Spontaneous circulation of active microtubules confined by optical traps. Unpublished.
- [5] Timothy Sanchez and Zvonimir Dogic. Engineering oscillating microtubule bundles. In *Methods in enzymology*, volume 524, pages 205–224. Elsevier, 2013.
- [6] Sarah Rice, Abel W Lin, Daniel Safer, Cynthia L Hart, Nariman Naber, Bridget O Carragher, Shane M Cain, Elena Pechatnikova, Elizabeth M Wilson-Kubalek,

- Michael Whittaker, et al. A structural change in the kinesin motor protein that drives motility. *Nature*, 402(6763):778, 1999.
- [7] Ronald D Vale and Ronald A Milligan. The way things move: looking under the hood of molecular motor proteins. *Science*, 288(5463):88–95, 2000.
- [8] Ronald D Vale, Thomas S Reese, and Michael P Sheetz. Identification of a novel force-generating protein, kinesin, involved in microtubule-based motility. *Cell*, 42(1):39–50, 1985.
- [9] Ronald D Vale, Takashi Funatsu, Daniel W Pierce, Laura Romberg, Yoshie Harada, and Toshio Yanagida. Direct observation of single kinesin molecules moving along microtubules. *Nature*, 380(6573):451, 1996.
- [10] Sangtae Kim and Seppo J Karrila. *Microhydrodynamics: principles and selected applications*. Courier Corporation, 2013.
- [11] Maciej Lisicki. Four approaches to hydrodynamic green’s functions—the oseen tensors. *arXiv preprint arXiv:1312.6231*, 2013.
- [12] J. R. Blake. A note on the image system for a stokeslet in a no-slip boundary. *Mathematical Proceedings of the Cambridge Philosophical Society*, 70(2):303–310, 1971.
- [13] Allen T Chwang and T Yao-Tsu Wu. Hydromechanics of low-reynolds-number flow. part 2. singularity method for stokes flows. *Journal of Fluid Mechanics*, 67(4):787–815, 1975.

- [14] C. E. Monteith, M. E. Brunner, I. Djagaeva, A. M. Bielecki, and J. M. Deutsch. Filler. *Biophys. J.*, 110(9):2053–2065, 2016.
- [15] Nadav Liron and S Mochon. Stokes flow for a stokeslet between two parallel flat plates. *Journal of Engineering Mathematics*, 10(4):287–303, 1976.
- [16] Masahiro Irie and Dawan Kunwatchakun. Photoresponsive polymers. 8. reversible photostimulated dilation of polyacrylamide gels having triphenylmethane leuco derivatives. *Macromolecules*, 19(10):2476–2480, 1986.
- [17] Masahiro Irie. Photoresponsive polymers. In *New Polymer Materials*, pages 27–67. Springer, 1990.
- [18] M Suzuki and O Hirasa. An approach to artificial muscle using polymer gels formed by micro-phase separation. In *responsive gels: volume transitions II*, pages 241–261. Springer, 1993.
- [19] Marc Behl and Andreas Lendlein. Actively moving polymers. *Soft Matter*, 3(1):58–67, 2007.
- [20] Ipsita Roy and Munishwar Nath Gupta. Smart polymeric materials: emerging biochemical applications. *Chemistry & biology*, 10(12):1161–1171, 2003.
- [21] Alberto Credi. Artificial molecular motors powered by light. *Australian journal of chemistry*, 59(3):157–169, 2006.
- [22] Matthijs KJ ter Wiel, Richard A van Delden, Auke Meetsma, and Ben L Feringa. Light-driven molecular motors: stepwise thermal helix inversion during unidirec-

- tional rotation of sterically overcrowded biphenanthrylidenes. *Journal of the American Chemical Society*, 127(41):14208–14222, 2005.
- [23] Nopporn Ruangsupapichat, Michael M Pollard, Syuzanna R Harutyunyan, and Ben L Feringa. Reversing the direction in a light-driven rotary molecular motor. *Nature Chemistry*, 3(1):53–60, 2011.
- [24] Javier Vicario, Martin Walko, Auke Meetsma, and Ben L Feringa. Fine tuning of the rotary motion by structural modification in light-driven unidirectional molecular motors. *Journal of the American Chemical Society*, 128(15):5127–5135, 2006.
- [25] Peter R Ashton, Roberto Ballardini, Vincenzo Balzani, Edwin C Constable, Alberto Credi, Oldrich Kocian, Steven J Langford, Jon A Preece, Luca Prodi, Emma R Schofield, et al. Ru(II)-polypyridine complexes covalently linked to electron acceptors as wires for light-driven pseudorotaxane-type molecular machines. *Chemistry–A European Journal*, 4(12):2413–2422, 1998.
- [26] Peter R Ashton, Roberto Ballardini, Vincenzo Balzani, Alberto Credi, Klaus Ruprecht Dress, Eléna Ishow, Cornelis J Kleverlaan, Oldrich Kocian, Jon A Preece, Neil Spencer, et al. A photochemically driven molecular-level abacus. *Chemistry–A European Journal*, 6(19):3558–3574, 2000.
- [27] Jose Berna, David A Leigh, Monika Lubomska, Sandra M Mendoza, Emilio M Pérez, Petra Rudolf, Gilberto Teobaldi, and Francesco Zerbetto. Macroscopic transport by synthetic molecular machines. *Nature materials*, 4(9):704, 2005.

- [28] Yi Liu, Amar H Flood, Paul A Bonvallet, Scott A Vignon, Brian H Northrop, Hsian-Rong Tseng, Jan O Jeppesen, Tony J Huang, Branden Brough, Marko Baller, et al. Linear artificial molecular muscles. *Journal of the American Chemical Society*, 127(27):9745–9759, 2005.
- [29] Carlos Bustamante, David Keller, and George Oster. The physics of molecular motors. *Accounts of Chemical Research*, 34(6):412–420, 2001.
- [30] Jacques Prost, Jean-François Chauwin, Luca Peliti, and Armand Ajdari. Asymmetric pumping of particles. *Physical Review Letters*, 72(16):2652, 1994.
- [31] Zhian Sun and Aixia Liu. Fast scheme for estimation of instantaneous direct solar irradiance at the earths surface. *Solar Energy*, 98:125–137, 2013.
- [32] David M Gates. Spectral distribution of solar radiation at the earth’s surface. *Science*, 151(3710):523–529, 1966.
- [33] Pierre-Gilles De Gennes and Pierre-Gilles Gennes. *Scaling concepts in polymer physics*. Cornell university press, 1979.
- [34] Efthymios Klampaftis, David Ross, Keith R McIntosh, and Bryce S Richards. Enhancing the performance of solar cells via luminescent down-shifting of the incident spectrum: A review. *Solar Energy Materials and Solar Cells*, 93(8):1182–1194, 2009.
- [35] Nils-Peter Harder and Peter Würfel. Theoretical limits of thermophotovoltaic solar energy conversion. *Semiconductor Science and Technology*, 18(5):S151, 2003.

- [36] JM Deutsch. Internal dissipation of a polymer. *Physical Review E*, 81(6):061804, 2010.
- [37] Peter Reimann and Peter Hänggi. Introduction to the physics of brownian motors. *Applied Physics A*, 75(2):169–178, 2002.
- [38] Frank Jülicher, Armand Ajdari, and Jacques Prost. Modeling molecular motors. *Reviews of Modern Physics*, 69(4):1269, 1997.
- [39] William H Press, Saul A Teukolsky, William T Vetterling, and Brian P Flannery. *Numerical recipes 3rd edition: The art of scientific computing*. Cambridge university press, 2007.
- [40] Ali Coskun, Michal Banaszak, R Dean Astumian, J Fraser Stoddart, and Bartosz A Grzybowski. Great expectations: can artificial molecular machines deliver on their promise? *Chemical Society Reviews*, 41(1):19–30, 2012.
- [41] B. A. Afzelius. Cilia-related diseases. *J. Pathol.*, 204(4):470–477, 2004.
- [42] Y. Okada, S. Takeda, Y. Tanaka, J., C. I. Belmonte, and N. Hirokawa. Filler. *Cell*, 121(4):633–644, 2005.
- [43] Charles J Brokaw. Molecular mechanism for oscillation in flagella and muscle. *Proceedings of the National Academy of Sciences*, 72(8):3102–3106, 1975.
- [44] Sébastien Camalet, Frank Jülicher, and Jacques Prost. Self-organized beating and swimming of internally driven filaments. *Physical Review Letters*, 82(7):1590, 1999.

- [45] Charles B Lindemann and Kathleen A Lesich. Flagellar and ciliary beating: the proven and the possible. *J Cell Sci*, 123(4):519–528, 2010.
- [46] M. A. Sleight. Filler. *Int. Rev. Cytol.*, 25:31–54, 1969.
- [47] M. A. Sleight, editor. *Cilia and Flagella*. Academic Press, 1974.
- [48] L. Gheber and Z. Priel. Filler. *Biophys. J.*, 55(1):183–191, 1989.
- [49] S. Gueron, K. Levit-Gurevich, N. Liron, and J. J. Blum. Filler. *Prot. Natl. Acad. Sci. USA*, 94(12):6001–6006, 1997.
- [50] Daniel J Needleman, Miguel A Ojeda-Lopez, Uri Raviv, Kai Ewert, Jayna B Jones, Herbert P Miller, Leslie Wilson, and Cyrus R Safinya. Synchrotron x-ray diffraction study of microtubules buckling and bundling under osmotic stress: a probe of interprotofilament interactions. *Physical review letters*, 93(19):198104, 2004.
- [51] Gregory J Pazour, Nathan Agrin, John Leszyk, and George B Witman. Proteomic analysis of a eukaryotic cilium. *J Cell Biol*, 170(1):103–113, 2005.
- [52] Karsten Kruse and F Jülicher. Actively contracting bundles of polar filaments. *Physical Review Letters*, 85(8):1778, 2000.
- [53] Tanniemola B Liverpool and M Cristina Marchetti. Instabilities of isotropic solutions of active polar filaments. *Physical Review Letters*, 90(13):138102, 2003.
- [54] M. Cosentino Lagomarsino, P. Jona, and B. Bassetti. Metachronal waves for deter-

- ministic switching two-state oscillators with hydrodynamic interaction. *Phys. Rev. E*, 68:021908, Aug 2003.
- [55] Boris Guirao and Jean-François Joanny. Spontaneous creation of macroscopic flow and metachronal waves in an array of cilia. *Biophysical journal*, 92(6):1900–1917, 2007.
- [56] Jens Elgeti and Gerhard Gompper. Emergence of metachronal waves in cilia arrays. *Proceedings of the National Academy of Sciences*, 110(12):4470–4475, 2013.
- [57] Thomas Niedermayer, Bruno Eckhardt, and Peter Lenz. Synchronization, phase locking, and metachronal wave formation in ciliary chains. *Chaos: An Interdisciplinary Journal of Nonlinear Science*, 18(3):037128, 2008.
- [58] L Bourdieu, T Duke, MB Elowitz, DA Winkelmann, S Leibler, and A Libchaber. Spiral defects in motility assays: a measure of motor protein force. *Physical Review Letters*, 75(1):176, 1995.
- [59] Gabriele De Canio, Eric Lauga, and Raymond E Goldstein. Spontaneous oscillations of elastic filaments induced by molecular motors. *Journal of The Royal Society Interface*, 14(136):20170491, 2017.
- [60] Edgar Meyhöfer and Jonathon Howard. The force generated by a single kinesin molecule against an elastic load. *Proceedings of the National Academy of Sciences*, 92(2):574–578, 1995.

- [61] JM Deutsch. Theoretical studies of dna during gel electrophoresis. *Science*, 240(4854):922–924, 1988.
- [62] JM Deutsch and TL Madden. Theoretical studies of dna during gel electrophoresis. *The Journal of Chemical Physics*, 90(4):2476–2485, 1989.
- [63] Yutaka Sumino, Ken H Nagai, Yuji Shitaka, Dan Tanaka, Kenichi Yoshikawa, Hugues Chaté, and Kazuhiro Oiwa. Large-scale vortex lattice emerging from collectively moving microtubules. *Nature*, 483(7390):448, 2012.
- [64] Tim Sanchez, Daniel TN Chen, Stephen J DeCamp, Michael Heymann, and Zvonimir Dogic. Spontaneous motion in hierarchically assembled active matter. *Nature*, 491(7424):431, 2012.
- [65] Stephen J DeCamp, Gabriel S Redner, Aparna Baskaran, Michael F Hagan, and Zvonimir Dogic. Orientational order of motile defects in active nematics. *Nature materials*, 14(11):1110, 2015.
- [66] Kun-Ta Wu, Jean Bernard Hishamunda, Daniel TN Chen, Stephen J DeCamp, Ya-Wen Chang, Alberto Fernández-Nieves, Seth Fraden, and Zvonimir Dogic. Transition from turbulent to coherent flows in confined three-dimensional active fluids. *Science*, 355(6331):eaal1979, 2017.
- [67] Arthur Ashkin, James M Dziedzic, and T Yamane. Optical trapping and manipulation of single cells using infrared laser beams. *Nature*, 330(6150):769, 1987.

- [68] DJ Stevenson, TK Lake, B Agate, V Garcés-Chávez, K Dholakia, and F Gunn-Moore. Optically guided neuronal growth at near infrared wavelengths. *Optics express*, 14(21):9786–9793, 2006.
- [69] Arthur Ashkin and James M Dziedzic. Optical trapping and manipulation of viruses and bacteria. *Science*, 235(4795):1517–1520, 1987.
- [70] Yasuhiro Harada and Toshimitsu Asakura. Radiation forces on a dielectric sphere in the rayleigh scattering regime. *Optics communications*, 124(5-6):529–541, 1996.
- [71] Frederick Gittes, Brian Mickey, Jilda Nettleton, and Jonathon Howard. Flexural rigidity of microtubules and actin filaments measured from thermal fluctuations in shape. *The Journal of cell biology*, 120(4):923–934, 1993.
- [72] Harald Felgner, Rainer Frank, and Manfred Schliwa. Flexural rigidity of microtubules measured with the use of optical tweezers. *Journal of cell science*, 109(2):509–516, 1996.
- [73] Pierre Bon, Sandrine Lécart, Emmanuel Fort, and Sandrine Lévêque-Fort. Fast label-free cytoskeletal network imaging in living mammalian cells. *Biophysical journal*, 106(8):1588–1595, 2014.
- [74] Andreas Mershin, Alexandre A Kolomenski, Hans A Schuessler, and Dimitri V Nanopoulos. Tubulin dipole moment, dielectric constant and quantum behavior: computer simulations, experimental results and suggestions. *Biosystems*, 77(1-3):73–85, 2004.

- [75] Erwin JG Peterman, Frederick Gittes, and Christoph F Schmidt. Laser-induced heating in optical traps. *Biophysical journal*, 84(2):1308–1316, 2003.
- [76] Stefan Kedenburg, Marius Vieweg, Timo Gissibl, and Harald Giessen. Linear refractive index and absorption measurements of nonlinear optical liquids in the visible and near-infrared spectral region. *Optical Materials Express*, 2(11):1588–1611, 2012.
- [77] Mark E Polinkovsky, Yann Gambin, Priya R Banerjee, Michael J Erickstad, Alex Groisman, and Ashok A Deniz. Ultrafast cooling reveals microsecond-scale biomolecular dynamics. *Nature communications*, 5:5737, 2014.
- [78] Laura R Serbus, Byeong-Jik Cha, William E Theurkauf, and William M Saxton. Dynein and the actin cytoskeleton control kinesin-driven cytoplasmic streaming in drosophila oocytes. *Development*, 132(16):3743–3752, 2005.
- [79] M. E. Brunner. *Polymer Dynamics*. PhD thesis, University of California, Santa Cruz, Santa Cruz, CA, 6 2011.
- [80] D. R. Brumley, M. Polin, T. J. Pedley, and R. E. Goldstein. Filler. *Phys. Rev. Lett.*, 109(26):268102, 2012.
- [81] D. R. Brumley, M. Polin, T. J. Pedley, and R. E. Goldstein. Filler. *J. R. Soc. Interface*, 12(108):20141358, 2015.
- [82] A. Morozov. Filler. *Science*, 355(6331):1262–1263, 2017.

- [83] K. Wu, J. B. Hishamunda, D. T. N. Chen, S. J. DeCamp, Y. Chang, A. Fernandez-Nieves, Seth Fraden, and Zvonimir Dogic. Filler. *Science*, 355(6331):eaal1979, 2017.
- [84] J. Slomka and J Dunkel. Filler. *Phys. Rev. Fluids*, 2:043102, 2017.
- [85] S. Kim and S. J. Karilla. *Microhydrodynamics: Principles and Selected Applications*. Dover Publications, 2005.
- [86] M. Lisicki. Four approaches to hydrodynamic Green’s functions – the Oseen tensors. *ArXiv e-prints*, December 2013.
- [87] Z. Zapryanov and S. Tabakova. *Dynamics of Bubbles, Drops, and Rigid Particles*. Springer, 1999.
- [88] J. R. Blake and M. A. Sleight. Mechanics of ciliary locomotion. *Biological Reviews*, 49(1):85–125, 1974.
- [89] Bruce Alberts, Alexander Johnson, Julian Lewis, Martin Raff, Keith Roberts, and Peter Walter. *Microtubules*. Garland Science, New York, 2002.
- [90] Dennis Bray. *Cell movements: from molecules to motility*. Garland Science, 2000.
- [91] Thomas L McMeekin, Merton L Groves, and Norbert J Hipp. Refractive indices of amino acids, proteins, and related substances. *Amino acids and serum proteins*, 44:54–66, 1964.

Appendix A

Supplementary Videos

Video showing the kinesin walking process discussed in section 1.2.2:

<https://www.youtube.com/watch?v=YAva4g3Pk6k>

Supplementary videos for the material in chapter 3 can be found here:

<https://sites.google.com/ucsc.edu/joshdeutsch/metachronal-videos?authuser=>

0

Supplementary videos for the material in chapter 4 can be found here:

<https://sites.google.com/ucsc.edu/joshdeutsch/optical-trap-videos?authuser=>

0